Università degli Studi di Padova

Dipartimento di Ingegneria dell'Informazione

Corso di Laurea Magistrale in Bioingegneria

Approaches based on nonlinear Kalman filtering to deal with physiological noise in the estimation of the hemodynamic response from functional near-infrared spectroscopy data

Laureando

Pietro Dal Bianco

Relatore

Prof. Giovanni Sparacino

Co-relatore

Ing. Sabrina Brigadoi

To Alessandra, for her constant support
and to my parents, who always believed in me.

Contents

Introduction

Functional near-infrared spectroscopy (fNIRS) is a non-invasive technique for monitoring the hemodynamic changes occurring in superficial regions of the brain cortex after a stimulus or a cognitive task. It uses non-ionizing near-infrared light to measure the concentration changes of oxy- and deoxy-hemoglobin occurring in the brain cortex and which are associated with the evoked brain activity [1][2]. fNIRS can be utilized in clinical and psychological settings to monitor brain activity or to recover the response of the brain to a particular task performed by the subject. During brain activation, indeed, an increase in oxy-hemoglobin concentration occurs in the area of the brain involved in the task. This increase in concentration can be measured by fNIRS and gives the so-called hemodynamic response function (HRF).

Unfortunately, fNIRS measured signals are strongly contaminated by systemic interference occurring in the superficial layers of the brain and in the brain itself, such as cardiac and respiratory oscillations and low frequency waves typically associated with vasomotor activity. These biological signals, which can be considered noise sources, make HRF estimation challenging. Many methods have been proposed in literature to reduce physiological noise and improve HRF estimation, but none of them has become a gold standard technique. Recently, the idea of using the so-called reference channel, which measures the physiological noise occurring in the superficial layers of the head without any influence of the HRF, has been proposed with some success [3]. Nevertheless, margins of improvement are worthwhile to be investigated.

In this thesis we will consider data collected at the Martinos Center for Biomedical Imaging, Massachusets General Hospital, Boston, and made available to the Department of Developmental Psychology, University of Padova, for a collaboration. These data are related to finger-tapping tasks performed by 7 healthy participants in order to investigate brain activation in the parietal hemisphere associated with motor activity. Soon after each task session was over, resting state data were recorded from the same participants to analyze the performance of the proposed algorithm in a semi-simulated scenario.

In particular, the thesis proposes a novel Unscented Kalman Filtering (UKF) approach for the reduction of systemic interference that affects fNIRS signals coupled with a linear Kalman filtering approach for the estimation of the hemodynamic response functions associated with brain activation. This novel approach will be compared to other literature techniques, namely Conventional Averaging (CA), Saager's method, the Linear Kalman filter approach and Extended Kalman Filtering (EKF) approaches. In particular, the comparison with CA and the linear Kalman filter approach will shed light on the importance of the reference channel for dealing with physiological noise oscillations. The comparison with Saager's method, instead, will highlight the strength of parametric approaches compared to non-parametric ones. Finally, the comparison between Unscented and Extended Kalman filtering approaches will provide information on the strength of the non-linearity of the fNIRS signal.

A brief outline of the thesis is as follows:

- Chapter 1 will review physical principles underlying fNIRS measurements and the state of the art about signal processing methodologies aiming at improving the HRF estimation from noisy data. In addition, the aims of the thesis will be presented.

- Chapter 2 will present the experimental scenario and protocol in which data employed in this thesis were acquired, along with some information about the fNIRS instrumentation adopted.

- Chapter 3 will briefly and theoretically review the Kalman filtering approach, both in the linear and non-linear estimation context. This approach will be used to estimate at each sample time the parameters of a specified physiological noise model in order to reduce systemic interference contaminating fNIRS data.

- Chapter 4 will describe the actual implementation of the novel UKF-based algorithm developed in this thesis, as well as briefly describe the literature methods used for the comparison and the new variant of the EKF approach.

- Chapter 5 will show the results of the application of the novel method in a semi-simulation scenario. Moreover, comparisons with the other literature methods will be carried out to better assess its performance.

- Chapter 6 will present results deriving from the application of the novel algorithm and of all the other methods for comparison on real cognitive data involving finger-tapping tasks.

- Chapter 7 will resume the results achieved and give future directions and insights about further developments of the present work.

Chapter 1

Functional near-infrared spectroscopy (fNIRS): physical principles, signal features, state of art on HRF estimation and aim of the thesis

1.1 A brief overview on fNIRS history and its development

Optical methods have been used to measure physiological variables for decades, but the use of diffuse optical light for physiological and non-invasive monitoring of brain activity has a relatively short history. This delayed development was mainly due to two primary issues.

The first one was sensitivity: there was the need to discover a wavelength range able to be absorbed mainly by the molecules of interest but not by the surrounding tissues and to develop sensitive detectors in order to monitor through large distances (centimeters) of tissue. Near-infrared wavelengths, which range roughly from 600 to 950 nm, are poorly absorbed by biological tissues while being at the same time highly absorbed by some chromophores of interest, that is oxy-hemoglobin (HbO) and deoxy-hemoglobin (HbR). Hence, this wavelength range turned out to be the ideal choice. In the late 1970s, Jöbsis [4] was the first to use near-infrared light to non-invasively monitor and estimate hemodynamic parameters in the brain tissues. This work can be considered the base of the new technology able to monitor brain activity non-invasively, which goes under the name of fNIRS.

The second issue was the need for a better understanding of how light propagates through highly scattering tissues. Recently, considerable work has been done on the theory of light propagation through scattering media, especially using phantoms [5] [6]. These studies allowed to overcome also the second obstacle which was hindering the further development of the fNIRS technique. Thanks to the simultaneous development of new image reconstruction algorithms, it became thus possible to reconstruct images of brain activation.

Early research, during the 1980s and 1990s, focused on the use of near infrared light for measuring brain hemoglobin oxygen saturation in neonates and adults. During the same period, functional magnetic resonance imaging (fMRI) became available for research purposes, providing whole brain images of the blood oxygen level-dependent (BOLD) signal, which is associated with blood flow and oxygen metabolism in the brain tissues. Nowadays, many research groups worldwide use fNIRS for functional brain studies as a non-invasive tool to monitor local changes in cerebral oxygenation and hemodynamics. In addition, a few groups have also worked on using diffuse light to measure neuronal activity directly rather than indirectly via hemoglobin changes. Indeed, it has been shown in vitro that neuronal activity is associated with an increase in light scattering, induced by a change in the index of refraction of the neural membranes [7]. Despite being born recently, the use of diffuse light for non-invasive imaging of brain activity is progressing very quickly. The accumulating literature [8] [9] demonstrates the unique ability of near-infrared techniques to detect hemodynamic, metabolic and neural signals associated with ongoing brain activity. Moreover, these techniques hold promise for providing absolute quantitative values of hemodynamic and metabolic parameters. Even if the progress and developments in the optic field were much slower than those in the fMRI one, fNIRS is now becoming more and more common in laboratories around the world, thanks also to recent advances both in hardware and signal processing methods.

1.2   fNIRS physical principles

1.2.1   fNIRS rationale

fNIRS instrumentation is composed by a certain number of sources, which are typically laser diodes or light emitting diodes, and a certain number of detectors, which are photomultiplier tubes or avalanche photo-diodes, that are both placed on human scalp non-invasively (Fig. 1.1). To perform an fNIRS acquisition, at least one detector and a pair of co-located sources are

needed: they create a so-called channel. The light emitted by the sources penetrates through the tissues, undergoes scattering and absorption phenomena, and eventually it reaches the detector which measures its intensity. From the difference in intensity between the light emitted by the source and the one measured at a nearby detector it is possible to recover the concentration changes of HbO and HbR occurring in the tissues underlying the measuring channel. The number and types of sources and detectors typically rely on the type of instrumentation and the experimental scenario involved in the study. Currently, several technical solutions exist for implementation of fNIRS, such as time domain (TD), frequency domain (FD) and continuous wave (CW) systems. The last technical solution is the most common and widely used.

Figure 1.1: left: typical adult probe placement during an fNIRS acquisition. Blue and red flags display sources and detectors respectively. The gray cables are the optical fibers. (Taken from [46]). Right: an example of an fNIRS instrumentation (taken from [47]).

The wavelength range employed in fNIRS studies typically ranges from 650 nm to 950 nm. Light emitted by a source travels through the scalp, skull, cerebrospinal fluid and eventually it reaches the gray matter of the brain. During this path, the main absorbent chromophores encountered for the near-infrared wavelength range are oxy- and deoxy-hemoglobin, while biological tissues are relatively transparent. These two molecules absorb light differently, as we can see from the absorbance spectrum in Fig. 1.3, and thus it is possible to compute the absorbance of both of them. These two molecules play a key role in brain studies because they reflect the neural activity during specific cognitive tasks. Indeed, when a brain region is active, it consumes

more glucose and oxygen. This causes a local increase in cerebral blood flow to that region and hence an increase in oxy-hemoglobin and a decrease in deoxy-hemoglobin concentration. These local changes in the concentration of HbO and HbR are captured by the fNIRS signal. In particular, in areas where more oxygen is needed, NIR light will be more absorbed, and so the detected light will have a lower intensity compared to the emitted one.

There are other main chromophores that are able to absorb near-infrared light in tissues underlying the scalp. These are water, lipids, melanin and cytochrome oxydase. Fortunately, water and lipids have a negligible impact on near-infrared light absorption, because their peak is placed at the end of the near-infrared wavelength window. On the other hand, melanin strongly absorbs near-infrared light, but its concentration is very low and so the contribution is rather limited. Finally, cytochrome oxydase is an interesting chromophore [10][11] , and it is an indicator of the intracellular metabolism. However, its contribution to absorption is low and at least one order of magnitude lower than the absorption due to hemoglobin, since its concentration is about 1 tenth of that of hemoglobin. Hence, HbO and HbR contributions are dominant in the NIR wavelength window, and absorption due to other chromophores is rather limited and can be considered constant in time. Thus, variations in the measured NIRS absorption signal can be considered due to hemoglobin only.

Once light passes through brain tissues, penetrating the human head to a depth of several centimeters, other than absorption also random scattering phenomena take place due to light interactions with underlying biological structures, such as scalp, fat and capillaries. Recent studies on the propagation of light in simplified models (e.g. semi-homogeneous medium) have defined the formulation of the so-called "banana-shaped " model, which defines a three-dimenstional model of the probability that a single photon, emitted from a source and measured by a detector, travels through a defined optical path. As we can see from Fig. 1.2, light is emitted from the source (black arrow), and travels through the skull and gray matter, and finally reaches two detectors placed at different distances ($r_N \leq 1$ cm and $r_F \approx 3$ cm (light blue and red arrow respectively)) from the source. Photons emitted by the source and measured at the detector position will have higher probability to follow the path described by the banana-shaped model (red and light blue for the two detectors) than to travel to other parts of the head and reach the detectors afterwards.

The penetration depth reached by photons is typically proportional to the distance between the source and the detector involved. In most fNIRS studies, source and detector pairs are placed on the scalp at 2-3 cm from each other so that light can reach a depth of about 3 cm under the skull,
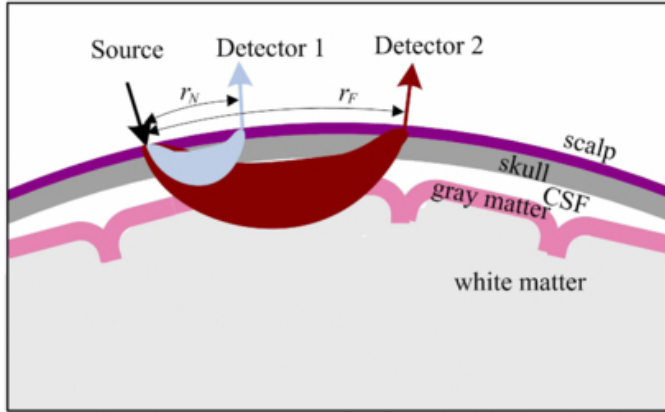
Figure 1.2: an overview of the theoretical "banana-shaped" model. It is worth noting the different depth reached by photons depending on the source-detector distance: only the channel with source-detector distance of ≈ 3 cm is probing the gray matter. Taken from [48].

and thus measure the brain activity in the gray matter. By increasing the source-detector distance, the depth reached by the photons will increase, but the Signal-to-Noise Ratio (SNR) will decrease. Decreasing the distance between source and detector (e.g. less than 1 cm), the photons will not reach the cerebral cortex, probing only the extra-cerebral layers. For this reason, standard sources and detectors are usually placed 2-3 cm far from each other in most fNIRS experiments.

1.2.2 Underlying theoretical formulation

NIRS theory is essentially based on the modified Beer-Lambert Law (MBLL) [12], which allows to compute HbO and HbR concentration changes from the intensity values of NIR light detected. This law is derived from the solution of the photon diffusion equations under the assumption of homogeneous medium. Let's start with the standard Beer-Lambert Law, which describes the ratio between the intensity of light emitted from a source (I_0) and the intensity measured at a detector (I) in a non-scattering medium. The equation is:

$$OD = -log\left(\frac{I}{I_0}\right) = \mu_a(\lambda) \cdot L \qquad (1.1)$$

where OD is the optical density or attenuation, $\mu_a(\lambda)$ is the absorption coefficient of the medium involved at a particular wavelength λ, and L is the
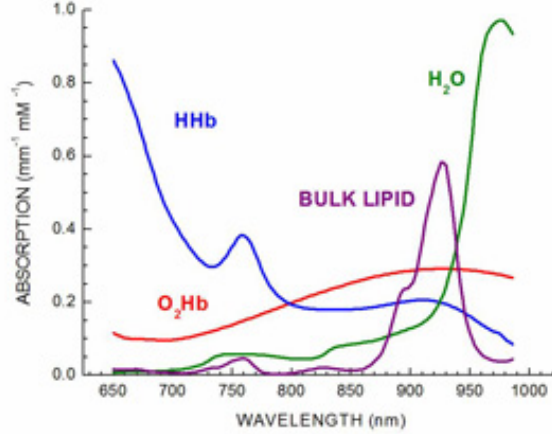
Figure 1.3: an overview of the absorption spectra of the main absorbers involved in the NIRS acquisition. Near-infrared wavelength range is from 650 nm to 950 nm.

distance travelled by photons through the medium, that is the optical pathlength. The absorption coefficient can be written as the product of the chromophore concentration c and its extinction coefficient ϵ. Hence, equation (1.1) becomes:

$$OD = c \cdot \epsilon(\lambda) \cdot L \tag{1.2}$$

In addition to absorption, scattering needs to be taken into account as well, since it is usually even more frequent than absorption. Photons that are subjected to more scattering events during their path will take longer to exit the tissues, and thus they will have a higher probability of being absorbed. Hence, we need to incorporate this scattering effect in the previous equations: the result is the MBLL mentioned before. It is derived from the solution of certain transport equations under the assumptions of homogeneous medium, high but constant scattering and homogeneous variations of the parameters of interest in the measured volume:

$$OD = c \cdot \epsilon(\lambda) \cdot d \cdot DPF(\lambda) + G(\lambda) \tag{1.3}$$

where $G(\lambda)$ has been added to account for potentially scattering losses and it depends on the measurement geometry and scattering coefficient, d is the real source-detector distance and $DPF(\lambda)$ is the differential pathlength factor,

which takes into account the increased path followed by the photons due to scattering.

Under the hypothesis of high but constant scattering effect, $G(\lambda)$ and $DPF(\lambda)$ can be considered constant. Thus, change in optical density (ΔOD) can only be caused by a change in concentration Δc, that is:

$$\Delta OD = OD_t - OD_{t_0} = \Delta c \cdot \epsilon(\lambda) \cdot d \cdot DPF(\lambda) \qquad (1.4)$$

where OD_{t_0} is the attenuation at time t_0 and OD_t the attenuation measured at time t. As mentioned previously, the main absorber in the near-infrared window is hemoglobin, while other chromophores can be considered to give a constant contribution. Hence, the variation in attenuation can be assumed, at each wavelength, as the linear combination of the contributions of HbO and HbR, considered independent, that is:

$$\Delta OD(\lambda) = (\Delta[HbO] \cdot \epsilon_{HbO}(\lambda) + \Delta[HbR] \cdot \epsilon_{HbR}(\lambda)) \cdot d \cdot DPF(\lambda) \qquad (1.5)$$

where $\epsilon_{HbO}(\lambda)$ and $\epsilon_{HbR}(\lambda)$ are the extinction coefficients of HbO and HbR at a particular wavelength λ, and $[HbO]$ and $[HbR]$ are HbO and HbR concentrations, respectively. Knowing the extinction coefficients of HbO and HbR, it is possible to compute the concentration changes of these two chromophores exploiting the MBLL and measuring the attenuation changes at two different wavelengths over approximately the same volume of tissue, that is what fNIRS is measuring:

$$\Delta[HbO] = \frac{\epsilon_{HbR}(\lambda_1)\frac{\Delta OD(\lambda_2)}{DPF(\lambda_2)} - \epsilon_{HbR}(\lambda_2)\frac{\Delta OD(\lambda_1)}{DPF(\lambda_1)}}{(\epsilon_{HbR}(\lambda_1) \cdot \epsilon_{HbO}(\lambda_2) - \epsilon_{HbR}(\lambda_2) \cdot \epsilon_{HbO}(\lambda_1)) \cdot d} \qquad (1.6)$$

$$\Delta[HbR] = \frac{\epsilon_{HbO}(\lambda_2)\frac{\Delta OD(\lambda_1)}{DPF(\lambda_1)} - \epsilon_{HbO}(\lambda_1)\frac{\Delta OD(\lambda_2)}{DPF(\lambda_2)}}{(\epsilon_{HbR}(\lambda_1) \cdot \epsilon_{HbO}(\lambda_2) - \epsilon_{HbR}(\lambda_2) \cdot \epsilon_{HbO}(\lambda_1)) \cdot d} \qquad (1.7)$$

Generalization of this formula for more than two wavelengths can be found in [13].

Unfortunately, the main simplifying hypothesis of the MBLL are not verified when we are measuring the fNIRS signal on an adult head. Indeed, biological tissues underlying the scalp are not homogeneous, since they are made up of different layers with different optical properties such as skin, skull, cerebrospinal fluid, capillaries. Hence, the concentration changes values obtained using the MBLL may be biased and cannot be used to provide

meaningful images. A more realistic model describing the propagation of photons in the brain is the diffusion equation [14]:

$$- D \cdot \nabla^2 \phi(r,t) + \nu \cdot \mu_a \cdot \phi(r,t) + \frac{\partial \phi(r,t)}{\partial t} = \nu \cdot S(r,t) \qquad (1.8)$$

where $\phi(r,t)$ is the photon fluence at time t and position r, which is proportional to intensity, $S(r,t)$ is the distribution of the sources of photons, ν is the speed of light in the medium, and $D = \nu/(3\mu'_s)$ is the photon diffusion coefficient with μ'_s and μ_a the reduced scattering coefficient and absorption coefficient respectively. The proposed model accurately describes light migration through a scattering medium, assuming that the probability of scattering is higher than that of absorption. Moreover, assuming that concentration changes are both global and small, the solution of the photon diffusion equation (1.8) for a semi-infinite medium is:

$$\Delta OD = -log\left(\frac{\phi_{final}}{\phi_{initial}}\right)$$
$$= \frac{1}{2}\left(\frac{3\mu'_s}{\mu_a^{initial}}\right)^{\frac{1}{2}} \cdot \left[1 - \left(1 + L(3\mu_s'^{initial}\mu_a^{initial})^{\frac{1}{2}}\right)^{-1}\right] \cdot$$
$$\cdot (\epsilon_{HbR}\Delta[HbR] + \epsilon_{HbO}\Delta[HbO]) \cdot d \qquad (1.9)$$

where $\phi_{initial}$ and ϕ_{final} are the initial and final photon fluence respectively, while $\mu_s'^{initial}$ and $\mu_a^{initial}$ the initial reduced scattering coefficient and absorption coefficient.

1.3 Pros and Cons of fNIRS compared to other neuroimaging techniques

An obvious first question when considering fNIRS as a method for assessing brain functions is what advantages it offers over Electroencephalography (EEG) or fMRI, two of the most diffuse techniques in neuroscience.

EEG, which measures voltage fluctuations resulting from ionic current flows within the neurons of the brain, has the advantage of being a measure of direct neural activity, while both fMRI and fNIRS are measures of cerebral hemodynamics, which can be considered correlated with neural activity [15]. EEG is a technique with relatively poor spatial resolution (of the order of centimeters). This means that it is relatively ineffective at differentiating specific regions or circuits in the brain, even when high-density arrays are

utilized. Source localization from EEG measurements is achieved by solving the so-called inverse problem to obtain and localize the most probable electrical sources in the brain. However, reliable results depend heavily on the number and position of electrodes and the algorithms employed in the analysis. Instead, EEG has a very high temporal resolution, of the order of milliseconds so that samples are typically acquired at frequencies ranging from 250 to 2000 Hz in clinical and research settings.

The fMRI technique can localize brain activity with greater spatial resolution compared to other techniques (voxel size of the order of millimeters, usually 3x3x3 mm), but it has a very low temporal resolution (about 2-3 seconds), depending on the repetition time employed (T_R). It is worth mentioning that fMRI provides whole-brain imaging, allowing to measure deep gray and white matter as well. Nevertheless, fMRI requires the subject to lie extremely still during the acquisition, in a noisy and relatively small environment, which might be uncomfortable.

fNIRS is a non-invasive versatile functional neuroimaging technology for monitoring brain activity. It has high potentials for research topics thanks to the high temporal resolution and cost effectiveness. In particular, fNIRS has a higher temporal resolution compared to fMRI (order of milliseconds or even less depending on the instrumentation used), but lower compared to EEG. Spatial resolution should be assessed considering both source-detector distance (e.g. horizontal resolution) and depth (e.g. vertical resolution). The spatial resolution is rather limited (2-4 cm) compared to fMRI, but it is higher than that of EEG. Recently, many efforts have been done to improve spatial resolution [16], as it usually relies on the instrumentation used and the source-detector numbers and position. The spatial resolution can be highly improved using high-density arrays for example (as in Diffuse Optical Tomography, DOT [17]) and reconstructing the activation changes in a three-dimensional head model. Also the depth resolution of fNIRS is limited: it is unable to measure cortical activity more than 4 cm deep in the brain.

An intrinsic advantage of fNIRS over fMRI is that the latter provides only one measure, the BOLD response, which is considered to be related to HbR concentration changes, whereas the former can use two (or more) near-infrared wavelengths to provide separate measures of both HbO and HbR.

Furthermore, fNIRS is definitely inexpensive compared to fMRI, and easy to move. This is a very important feature for those patients who are unable to move, allowing brain assessment directly at the bed-site. It is easy to use as well, and thus it does not require heavy staff training.

Unfortunately, fNIRS has some drawbacks as well. The key limitation of fNIRS is that it can only probe the surface layers of the cortex (e.g. grey

matter). Consequently, brain structures that lie deeper in the brain cannot be measured. Moreover, the SNR is highly variable from subject to subject and it is influenced by different factors such as skull thickness, which increases absorption and scattering, and hair color (black hair usually absorbs more light than blonde one). Nevertheless, fNIRS is less sensitive to head motion artifacts compared to other techniques. Therefore, it can easily be used to monitor newborns and children [18].

Finally, fNIRS does not interfere with high magnetic or electric fields. This allows easy integration with other techniques such as MRI, Magnetoencephalography (MEG) or EEG. In this way, morphological, electrical and functional brain information can be combined to better understand the phenomena under investigation. A lot of research is being conducted nowadays to integrate morphological and functional information from both fNIRS and fMRI signals, as shown in [19][20].

1.4   The fNIRS signal: features and components

fNIRS can be used to gather information about the hemodynamic correlates of neural activity both in infants and adults, using tasks that assess, for example, visual perception, memory and language abilities [21][22][23]. These are exciting findings, but they are tempered by a number of critical methodological issues that must be solved to ensure that fNIRS becomes a technique that is robust and reliable for daily use.

In functional brain imaging, the signal acquired with fNIRS is a mixture of evoked HRF, several background physiological components such as cardiac, respiratory and Mayer's wave and measurement noise. The main issue related to fNIRS is the separation of the HRF, which represents the useful and informative signal, from all other sources of noise due to brain physiology.

1.4.1   The hemodynamic response function (HRF)

The HRF represents the key signal in fNIRS studies, since it allows the estimation of brain activation during specific tasks. The presence of HRF in fNIRS signals is a consequence of physiological processes. Indeed, neurons are activated in defined areas of the cortex during specific tasks and they start firing, consuming glucose and oxygen. As a consequence, the increased oxygen consumption leads to an increased cerebral blood flow (CBF) and cerebral blood volume (CBV) in the areas where brain activation is occurring, in order to give more and more nutrients to the firing neurons. The increase in blood flow and oxygen is much greater than the real needs of the firing

neurons. Hence, HbO concentration will increase substantially due to oxygen recruitment, while HbR concentration will decrease. Brain activation can be detected and measured relying on HbO and HbR concentration changes, since they reflect neuronal activity, as mentioned before. It is worth mentioning that the HRF is highly variable, depending on the types of stimuli, their duration, and other causes such as adaptation and brain region. However, it is a slow response (10-20 seconds, compared to the milliseconds EEG evoked responses). Many models have been employed to estimate the HRF $h_{true}(t)$ from noisy fNIRS data in literature [24][25], but the most widely used is the canonical model, which is a combination of two gamma-variant functions Γ_{n_1} and Γ_{n_2} with a total of 6 parameters to adjust, that is:

$$h_{true}(t) = \alpha \cdot [\Gamma_{n_1}(t, \tau_1, \rho_1) - \beta \cdot \Gamma_{n_2}(t, \tau_2, \rho_2)] \tag{1.10}$$

where:

$$\Gamma_n(t, \tau_j, \rho_j) = \frac{1}{p!\tau_j} \left(\frac{t - \rho_j}{\tau_j} \right)^p e^{-\frac{(t-\rho_j)}{\tau_j}} \delta(t-\rho_j), \ \ \delta(t-\rho_j) = \begin{cases} 1 & \text{if } (t - \rho_j) \geq 0 \\ 0 & \text{otherwise} \end{cases}$$

where α tunes the amplitude, τ_j and ρ_j tune the response width and the onset time respectively, and β controls the ratio of the response to undershoot. An example of noise-free HRF prediction with the canonical model is shown in Fig. 1.4, where parameters have been set as: $\alpha = 1000$, $p = 2$, $\tau_1 = 1$, $\tau_2 = 0.81$, $\rho_1 = 0.7$, $\rho_2 = 0.81$, $\beta = 0.05$, producing the variation of HbO concentration over time ($\Delta HbO(t)$). As we can see, at time t=0 s the stimulus is presented and neural activation starts. Oxygen recruitment and its consumption start, but the recruitment is much greater than the consumption and thus HbO concentration increases. A peak is reached at about 300 nM and then the signal returns to baseline values, with an undershoot due to the fact that at the end of neuronal activation, the CBF decreases more rapidly than CBV.

Unfortunately, the HRF is not the only signal detected by fNIRS optodes. Indeed, fNIRS measures activity occurring in the underlying biological tissues, and thus there are other physiological components that contaminate the raw measured signal, making the HRF hard to estimate.

The major sources of interference are cardiac and respiratory activity, which are partly coupled. There are also low frequency spontaneous physiological oscillations typically named vasomotor waves or Mayer's waves (with a frequency around 0.1 Hz), as well as very low frequency oscillations (with a frequency around 0.04 Hz). All of these physiological interference sources
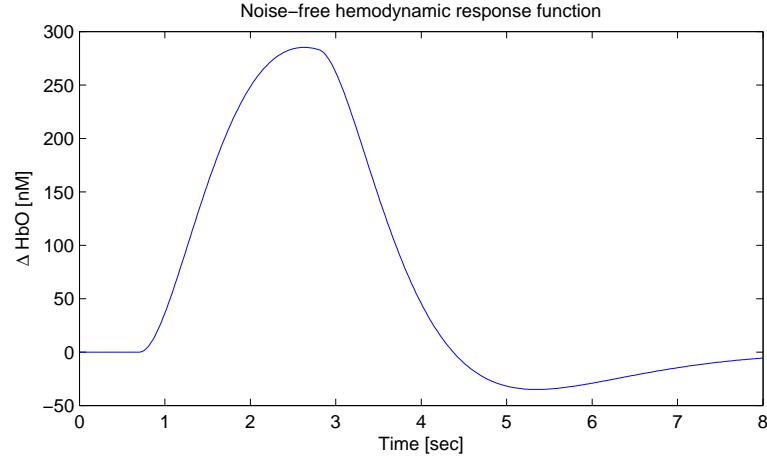
Figure 1.4: HRF prediction for HbO with the canonical model. In this example, parameters have been set as: $\alpha = 1000$, $p = 2$, $\tau_1 = 1$, $\tau_2 = 0.81$, $\rho_1 = 0.7$, $\rho_2 = 0.81$, $\beta = 0.05$.

are located both in the vasculature of the layers overlaying the brain (for instance in the skin layer) and in the brain itself, and are often referred to as global interference. These components have different underlying origins, amplitudes and frequencies. In addition, other sources of noise are inherent to the raw signal such as measurement noise and motion artifacts. An overview of these components is shown in Fig. 1.5.

1.4.2   Heart beat component

Heart beat typically has a frequency range from 60 to 80 beats per minute (about 1 Hz), and this physiological component can be modeled with a sinusoid, whose frequency is about 1 Hz and amplitude ranging from 0 to 500 nM. This component is not crucial in the HRF estimation. Indeed, it can be easily distinguished from all other sources of contamination, because its frequency range is typically higher compared to the frequency range of the HRF. For this reason, a standard low-pass filter can be employed to remove this oscillation without affecting the HRF.

1.4.3   The respiratory component

The respiratory component can be modeled with a sinusoid as well, with amplitude varying between [0-500] nM, but its frequency range lies around 0.2 Hz. This component contaminates the HRF signal, since their frequency ranges are comparable, and thus filtering is no longer optimal.
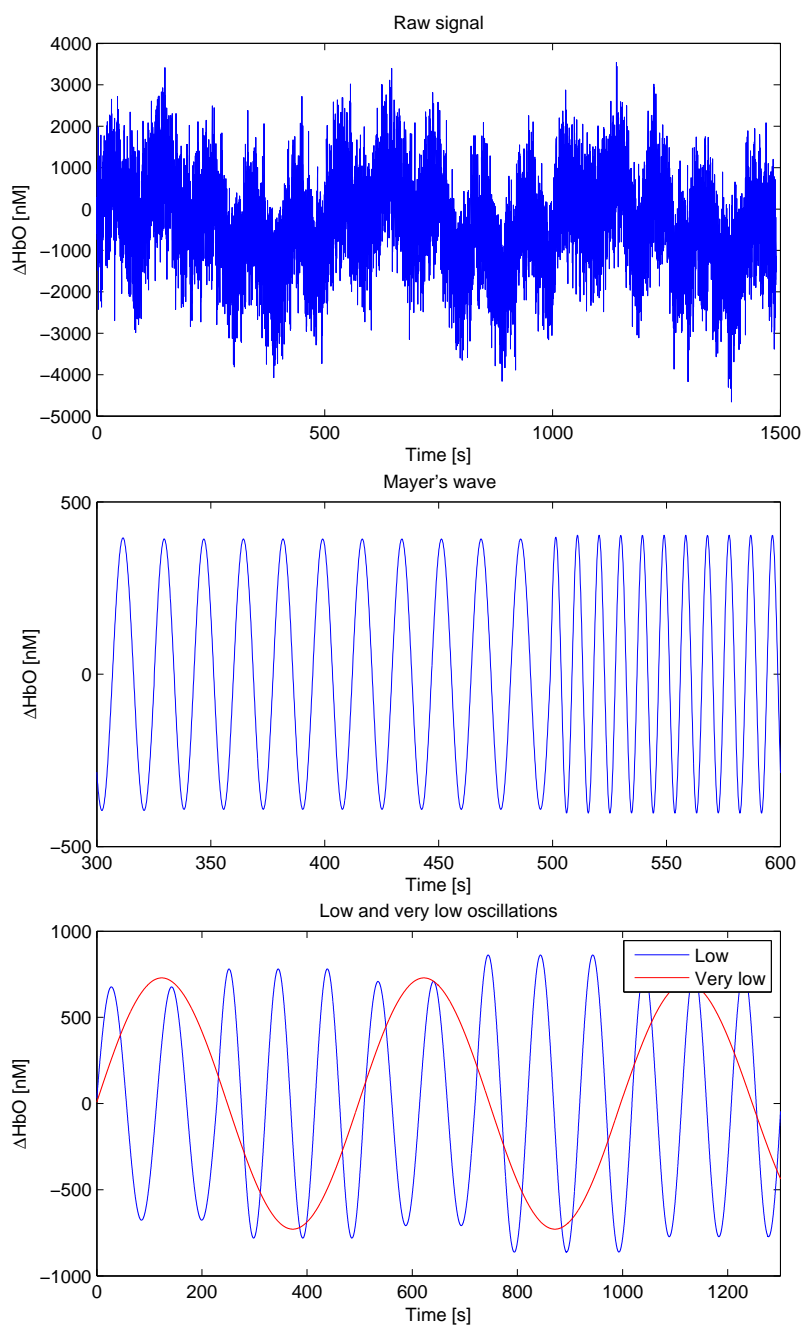
Figure 1.5: Top: raw signal measured. Middle: simulated example of Mayer's wave. Bottom: simulated examples of low (blue line) and very low (red line) oscillations. It is worth noting that amplitudes and frequencies are time-varying. Note also the different temporal scale of the figures.

1.4.4   Mayer's wave

The Mayer's wave or vasomotor wave is probably related to cyclic changes in arterial blood pressure in vessels and it shows significant coherence with sympathetic nervous activity. Its frequency spectrum ranges from 0.03 and 0.18 Hz, and overlaps with the HRF spectrum. Thus, it is impossible to remove the Mayer's wave without affecting the HRF using a standard band-pass filtering approach. Another main issue related to this form of contamination, is the fact that Mayer's wave's amplitude is typically higher than the HRF's one, making HRF estimation even harder.

1.4.5   Very low frequency oscillations

Very low frequency oscillations are contamination signals whose spectra are centered at around 0.004 Hz. These oscillations are responsible for signal trends and they are typically coupled with blood vessels pressure.

1.4.6   Motion artifacts

Motion artifacts are typically caused by small movements of the participant during a recording session, or by the uncoupling between one or more source-detector pairs and the participant's scalp. These artifacts can be usually detected by eye inspection, because they cause abrupt changes both in HbO and HbR concentration signals. However, the presence of these artifacts can sometimes lead to biased HRF estimates, and thus new algorithms are being developed to remove these sources of error, such as the spline interpolation approach [26] or the wavelet approach [27]. However, there is not a gold standard algorithm for removing these sources of error, even though some important studies have been conducted to test the impact and performances of these methods, such as in [28], where it has been shown that the wavelet filtering approach is the most powerful and promising technique to reduce and correct motion artifacts.

1.4.7   Measurement noise

Finally, the last but not least source of contamination is measurement noise. Its statistical description is not clearly known since fNIRS signal is non-stationary. This means that mean and variance are highly variable not only from subject to subject, but also during the recording session itself. An important thing to know, is that fNIRS is very sensitive to external sources of light. In order to minimize this source of noise, acquisitions typically take

place in a dimly-lit room, so that external light does not interfere with the near-infrared light employed.

1.5   State of the art methods for HRF estimation

From the discussion made so far, it turns out that the main goal in fNIRS studies is the estimation of the HRF. Unfortunately, this useful signal that correlates with neural activity is hidden in the raw signal acquired due to different physiological oscillations that can be considered noise. Some oscillations such as heart beat can be simply removed by standard filtering, but Mayer's waves and other low frequency oscillations cannot be completely removed without affecting the HRF itself. As a consequence, physiological noise removal from the fNIRS signal is an important open issue which should be solved to make fNIRS robust and reliable in research and clinical settings. In literature, several different methods have been proposed to remove or at least reduce physiological noise. Some of these rely only on standard channel signals while others on the use of the so-called reference channel, a channel with source-detector distance less than 1 cm. Due to the directly proportional relationship between source-detector distance and depth reached by photons, the reference channel will probe only the superficial layers of the head (i.e. scalp and skull) but not the cerebral cortex. Hence, the reference channel signal contains the same physiological noise of standard channel signals but it does not contain the hemodynamic response. This signal can thus be used to reduce physiological noise in standard channel without the risk of removing the HRF. The algorithms that exploit the reference channel can be further divided into two subgroups: the ones that use a parametric approach and the ones that use a non-parametric approach for the HRF estimation.

1.5.1   Bandpass filtering

The first and the simplest method to estimate the HRF and reduce physiological oscillations is band-pass filtering. This simple method only exploits standard channel signals and allows to remove oscillations with frequencies far from the ones of the useful signal, such as heart beat frequencies and very low frequency oscillations, responsible for signal drifts. This method has been widely employed in many studies [29], not only as a method itself but also as a preprocessing step in other fNIRS signal processing algorithms, such as in [30]. However, filtering does not allow to remove low frequency

physiological noise from fNIRS data, because of the overlapping in frequency between the physiological noise and the HRF.

1.5.2   Conventional averaging

Conventional averaging (CA) is widely used in signal processing algorithms, and it is a mainstay for HRF estimation. Again, this method relies only on standard channel signals. The raw signal is divided into several sweeps lasting about 15 seconds from the stimulus onset, and then all sweeps related to the same stimulus type are averaged. The main hypothesis is that noise, given by the sum of all physiological components and measurement noise in this case, is random with zero mean, variance σ^2, and stationary with no correlation with the HRF. The mean can be expressed as:

$$y_m(t) = \frac{1}{N} \sum_{i=1}^{N} (u_i(t) + v_i(t)) = u(t) + \frac{1}{N} \sum_{i=1}^{N} v_i(t) \qquad (1.11)$$

where $u_i(t)$ is the i-th HRF, $v_i(t)$ is noise in sweep number i and $u(t)$ is the HRF assumed equal for all trials. Taking the expectation of eq. (1.11) we get:

$$E[y_m(t)] = E[u(t)] + \frac{1}{N} \sum_{i=1}^{N} E[v_i(t)] = u(t) \qquad (1.12)$$

It turns out that CA gives non-polarized estimates. To quantify estimation precision, the variance of the estimation error can be derived as:

$$e(t) = y_m(t) - u(t) \qquad (1.13)$$

$$var[e(t)] = E\left[\left(\frac{1}{N} \sum_{i=1}^{N} v_i(t)\right)^2\right] = \frac{1}{N^2} E[v_i^2(t)] = \frac{\sigma^2}{N} \qquad (1.14)$$

Thus, if $N \longrightarrow \infty$ then var[e(t)] $\longrightarrow 0$, and the estimation precision is proportional to the number of trials N. However, this method requires many sweeps (about 100 sweeps) to give an accurate estimate of the mean HRF and the time required for signal acquisition would be too long. Moreover, CA hypotheses are never verified when dealing with real data and phenomena such as participant's adaptation could lead to biased HRF estimates.

1.5.3 Reference-channel subtraction method

The subtraction of a reference channel signal from standard channel signal to get rid of physiological noise and improve HRF estimation was firstly proposed by Saager et al. [31]. This method paved the way for all the future algorithms based on the reference channel subtraction idea. This method can be categorized into the reference-channel methodologies based on a non-parametric approach.

In particular, they acquired many time series using different probe geometries, based on the intuition that detectors near the source (≈ 5 mm) are more likely to record only physiological noise rather than brain activity. The authors scaled the reference channel signal to the standard channel signal using the least-squares method and then employed a weighted subtraction of the scaled reference channel signal from the standard channels signal in order to delete or at least reduce physiological contamination present in the standard channels.

1.5.4 Reference channel modeling corrected Bayesian approach (ReMCoBA)

Another method that performs physiological noise reduction exploiting the reference-channel and estimates the HRF with a non-parametric approach, as the Saager's method, is the Reference Channel Modeling Corrected Bayesian Approach (ReMCoBA) proposed by Scarpa et al. [3] and developed in [32]. Succinctly, the algorithm consists of two main steps: in the first step a physiological noise model is estimated from the reference-channel data trial by trial, in order to reduce physiological noise contamination. In the second step, the physiological noise corrected data are filtered on a single trial basis with a non-parametric Bayesian approach to further reduce residual random noise. In more details, standard-channel signals $y(t)$ were modeled as a sum of three components, that is the HRF $u(t)$, physiological noise $\phi(t)$ and random measurement noise $v(t)$:

$$y(t) = u(t) + \phi(t) + v(t) \tag{1.15}$$

whereas reference-channels $y_{ref}(t)$ were assumed to contain the same physiological noise $\phi(t)$, but scaled by a factor s constant over time to take into account different paths crossed by photons and random noise $\varepsilon(t)$, that is:

$$y_{ref}(t) = \frac{\phi(t)}{s} + \varepsilon(t) \tag{1.16}$$

Physiological noise was modeled as a sum of M sinusoidal waves on a trial by trial basis, that is:

$$\phi(t) = \sum_{i=1}^{M}[a_i sin(2\pi\omega_i t) + b_i cos(2\pi\omega_i t)] + c + w(t) \qquad (1.17)$$

where $w(t)$ is the model error, ω_i is the frequency, a_i, b_i and c represent sinusoidal amplitudes and offset, respectively. To estimate an optimum value for M and the corresponding sinusoidal frequencies ω_i for i=1,...,M, peaks were individuated from the power spectrum on a trial by trial base and then a grid search algorithm was employed to further improve $\hat{\omega}_i$ estimates. The maximum value for M was set to 3 in order to model physiological noise that lies in the HRF spectrum, i.e. respiration, Mayer's wave and very low frequency oscillations.

Finally, $\hat{a}_i$, $\hat{b}_i$ and $\hat{c}$ were estimated by the linear least squares method, whereas $\hat{s}$ was determined by minimizing the squared difference between the standard-channel signal $y(t)$ and the corresponding reference-channel signal $y_{ref}(t)$ described previously.

Once physiological noise model was determined, it was used to correct the standard-channel raw signal and obtain $y_c(t)$ that is:

$$y_c(t) = y(t) - \hat{s} \cdot \sum_{i=1}^{\hat{M}}[\hat{a}_i sin(2\pi\hat{\omega}_i t + \hat{b}_i cos(2\pi\hat{\omega}_i t)] + \hat{c} \qquad (1.18)$$

The corrected signal $y_c(t)$ was then filtered with a non-parametric Bayesian approach. Succinctly, at this step $y_c(t)$ can be modeled as:

$$y_c(t) = u(t) + v(t) \qquad (1.19)$$

where now $u(t)$ is the HRF to estimate and $v(t)$ is simply noise. Re-expressing eq. (1.19) in matrix form we get:

$$\mathbf{y}_c = \mathbf{u} + \mathbf{v} \qquad (1.20)$$

where $\mathbf{u}$ and $\mathbf{v}$ are vectors containing the n samples of the trial. In the Bayesian context, HRF estimation can be pursued using the minimum error variance linear estimation formula, that is:

$$\hat{\mathbf{u}} = (\mathbf{\Sigma}_v^{-1} + \mathbf{\Sigma}_u^{-1})\mathbf{\Sigma}_v^{-1}\mathbf{y}_c \qquad (1.21)$$

To estimate the a priori covariance matrix of $\mathbf{v}$ ($\mathbf{\Sigma}_v$), an auto-regressive model (AR) of order 4 was employed for each trial:

$$\mathbf{\Sigma}_v = \sigma^2(\mathbf{A}^T\mathbf{A})^{-1} \tag{1.22}$$

where $\mathbf{A}$ was a square nxn Toeplitz matrix whose first column was

$$[1, a_1, a_2, a_3, a_4, 0, \ldots, 0]^T$$

and a_i for i=1,..,4 are the AR model coefficients. σ^2 is the noise variance which drives the AR model and it was estimated from data in an interval ranging from 1.5 s before the stimulus onset to 2.5 s after.

In order to estimate the a priori covariance matrix of $\mathbf{u}$ ($\mathbf{\Sigma}_u$), a stochastic process given by the cascade of 2 integrators was employed, driven by zero-mean white noise process ϵ_k with variance λ^2:

$$\mathbf{\Sigma}_u = \lambda^2(\mathbf{F}^T\mathbf{F})^{-1} \tag{1.23}$$

where $F = \Delta^2$, with Δ^2 being the squared n-dimensional lower triangular Toeplitz matrix, whose first column was $[1, -2, 1, 0, \ldots, 0]^T$.

Once all unknown parameters are estimated, using (1.22) and (1.23), eq. (1.21) can be re-written as:

$$\hat{\mathbf{u}} = (\mathbf{A}^T\mathbf{A} + \gamma\mathbf{F}^T\mathbf{F})^{-1}\mathbf{A}^T\mathbf{A}\mathbf{y}_c \tag{1.24}$$

where $\gamma = \frac{\sigma^2}{\lambda^2}$ is a tuning parameter which is determined relying on the Twomey criterion for each trial.

Once all HRFs have been estimated on a single trial basis, all HRFs related to the same stimulus type are averaged and then smoothed with a 3rd order polynomial Savitzky-Golay filter with frame size of 25 time points. Finally, $\hat{\mathbf{u}}$ was baseline corrected by subtracting the mean intensity calculated in the range [0-500] ms from stimulus onset.

1.5.5 Parametric approach with coefficients estimated by linear Kalman filtering

A different approach that exploits the reference-channel signals as regressors, but estimates the HRF using a parametric model, has been proposed by Gagnon et al. [33]. They use a linear Kalman filter approach in order to

estimate single trial HRFs. The linear Kalman filter tries to dynamically estimate the weights associated to some gaussian functions employed to model the HRF over time. The HRF $h(t)$ was modeled as a set of $N_w=15$ temporal basis functions, that is:

$$h(t) = \sum_{i=1}^{N_w} w_i b_i(t) \tag{1.25}$$

where $b_i(t)$ are normalized Gaussian functions with means separated by 0.5 s and standard deviation of 0.5 s, as shown in Fig. 1.6. It is worth noting that $h(t)$ represents the Finite-Impulse-Response (FIR) of the system.
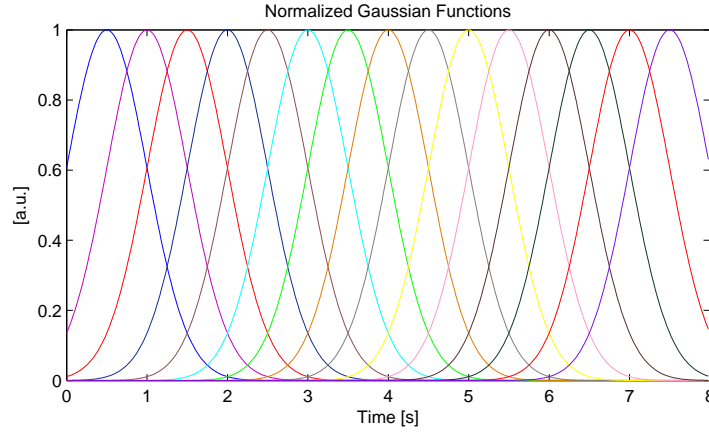
Figure 1.6: normalized gaussian functions used in the linear kalman filtering approach.

Hence, the HRF signal y_{HRF} can be modeled as the output of the FIR filter, that is:

$$y_{HRF}(t) = \sum_{k=-\infty}^{\infty} h(k)u(n-k) \tag{1.26}$$

where $u(t)$ represents the onset vector, which takes values of 1 only when the stimulus is shown to the participant and 0 otherwise.

The signal obtained from standard-channels $y_3(t)$ was modeled as a linear combination of the HRF and the reference-channel signal $y_1(t)$ as:

$$y_3(t) = \sum_{k=-\infty}^{\infty} h(k)u(n-k) + \sum_{i=1}^{N_a} a_i y_1(n+1-i) \tag{1.27}$$

where N_a is the number of points taken from the reference-channel data and used as regressors, and a_i are their weights. In this study N_a was set to 1.

Eqs. (1.25) and (1.27) can be re-expressed in state space form. Defining the state vector $\mathbf{x}$ as:

$$\mathbf{x} = \begin{bmatrix} w_1 & w_2 & ... & w_{N_w} & a_1 & ... & a_{N_a} \end{bmatrix} \tag{1.28}$$

and assuming that the a priori evolution of the states are described by a random-walk model, we get the process equation:

$$\mathbf{x}_{k+1} = \mathbf{I} \cdot \mathbf{x}_k + \mathbf{w}_k \tag{1.29}$$

where $\mathbf{w}_k$ is the process noise and $\mathbf{I}$ is a $N_w + N_a$x$N_w + N_a$ identity matrix.

To derive the measurement equation, we must define the matrix $\mathbf{U}$, whose columns are the linear convolution between the onset vector $u(t)$ and each temporal basis function $b_i(t)$, that is:

$$\mathbf{U} = \begin{bmatrix} u \otimes b_1(t) & u \otimes b_2(t) & ... & u \otimes b_{N_w}(t) \end{bmatrix} \tag{1.30}$$

Defining matrix $\mathbf{A}$ as the concatenation of the matrix $\mathbf{U}$ in (1.30) and matrix $\mathbf{Y}$

$$\mathbf{A} = \begin{bmatrix} \mathbf{U} & \mathbf{Y} \end{bmatrix} \tag{1.31}$$

where

$$\mathbf{Y} = \begin{bmatrix} y_1(1) & 0 & ... \\ y_1(2) & y_1(1) & 0 \\ \vdots & \vdots & \ddots \end{bmatrix} \tag{1.32}$$

the filter takes into account also data deriving from the reference-channel as in (1.27). Thus, measurement equation can be expressed as:

$$y_{3_k} = \mathbf{C}_k \cdot \mathbf{x}_k + \mathbf{v}_k \tag{1.33}$$

where $\mathbf{v}_k$ is measurement noise and $\mathbf{C}_k$ is a 1 by $N_w + N_a$ vector whose entries correspond to the kth row of $\mathbf{A}$ in (1.31).

The estimate $\hat{\mathbf{x}}_k$ has been computed using classical kalman filter equations which will be discussed in chapter 2 in more detail, followed by the

Rauch Tung-Striebel (RTS) smoother. The estimated HRF time course was determined as:

$$\hat{h}_k = \mathbf{C}_k \cdot \hat{\mathbf{x}}_{k|N_t} \tag{1.34}$$

where $\hat{\mathbf{x}}_{k|N_t}$ is the state $\mathbf{x}$ at time k estimated with the RTS smoother.

1.6 Discussion on methods for HRF estimation and open issues

Over the past 15 years, fNIRS has emerged as a complement to fMRI for estimating the HRF related to cerebral activity above all in situations where fMRI cannot be used. A common problem with fNIRS time series is the presence of strong physiology-based systemic interference, which affects both the HRF estimation and the corresponding brain activation. As mentioned before, this interference derives from cardiac activity, respiration and other physiological and homeostatic processes. As a consequence, NIRS signal is usually contaminated by systemic interference occurring in the superficial layers of the head, that is the scalp and skin. Recent findings have shown that short source-detector separations (reference-channels), can be used as regressors in order to filter the systemic interference affecting the longer source-detector measurements (standard channels) [34]. As such, many different methods have been proposed in literature, but considerable work remains in terms of improvements and suitability to real-time use. Indeed, it is still difficult to filter global interference without affecting the HRF estimation due to common frequency ranges.

In this chapter we have shown that several methods have been proposed in literature to reduce physiological noise and improve the HRF estimation. Some of these methods use only standard-channel signals, such as standard filtering and CA. Despite being simple, standard filtering does not allow to remove physiological noise located in the same frequency range of the HRF, while CA requires many sweeps to be collected for good results. Moreover, CA underlying hypotheses are never verified in real contexts, leading to biased HRF estimates.

In order to overcome these limitations, reference-channel approaches have been investigated and proposed. These algorithms can be divided into two different groups: non-parametric and parametric methods. Two examples of non-parametric approaches presented before are the reference-channel subtraction and ReMCoBA methods.

The reference-channel subtraction method has demonstrated significant

improvements in reducing physiological noise. Indeed, it was shown that this procedure removed, on average, 60% of the total measured NIRS signal, which can be considered background physiological noise. Therefore, most of the signal acquired was not specific and did not carry useful information. However, least squares method might cause an overfitting of the reference channel signal to the standard channel signal, especially when the HRF is synchronous with the physiological noise present in the reference channel. As a consequence, the HRF could be potentially removed or its estimated amplitude reduced. Despite this down side, this study has paved the way for an increasing number of algorithms that are based on the reference-channel approach.

ReMCoBA method has shown improvements not only in mean HRF estimation, but also in other cognitive parameters related to the HRF, i.e. peak amplitude and peak latency estimation. One of its strength is the lack of assumptions made on shape, amplitude or latency of the HRF. However, in some contexts, where for example the HRF to be estimated is very small but with a known expected shape and the number of available trials is limited, the lack of priors can be a drawback. In these situations, HRF estimation could be further improved by considering stronger priors, which are able to better describe the signal. This is pursued by the other subgroup of algorithms mentioned before that exploits the reference channel: the ones that use a parametric approach.

The linear Kalman filtering approach discussed in section 1.5.5 is an example of these approaches. Simulations and statistical analysis have shown that this approach leads to interesting and significant improvements in the mean HRF estimation, especially when few trials are available. In addition, an important aspect of the study is that Gaussian basis functions allow to model HRF with different shapes, duration and components, such as initial dips or undershoots, making this approach less restrictive even in the presence of a stronger prior. Thus, it turns out that better HRF estimates can be pursued following the direction of the reference-channel parametric approaches.

1.7   Aims of the thesis

The main aim of this thesis is to implement and test the performance of a new parametric approach, based on the Kalman filter theory, that exploits reference channel data to improve the estimation of the HRF. In particular, this thesis will focus on the implementation of the so-called Unscented Kalman Filter (UKF), which is an alternative version of Kalman filtering in a

non-linear context, to model physiological noise oscillations measured in reference channel signals. A more common and known version of the non-linear Kalman filter is the Extended Kalman filter (EKF). A method exploiting EKF and reference channel data to improve HRF estimation has been proposed in [35] and its performance will be compared with the one of the UKF here introduced. Furthermore, in this thesis, an improvement to this EKF method will also be proposed.

UKF and EKF will be theoretically reviewed in chapter 3. Both UKF and EKF will be used to estimate systemic interference from reference-channel data. The estimated noise model will be then used to reduce physiological noise in standard channels. After that, a Linear Kalman Filter will be employed for the HRF estimation in standard channels. Thus, this thesis will try to give its contributions to the parametric approaches that rely on reference channel data. Indeed, these methods are being developed in literature since it has been shown that they give more accurate estimates, and so future directions will be pursued in this field.

Another aim of this thesis is to test whether the use of the reference channel in a parametric context actually gives better performances in terms of HRF estimation compared to the use of the standard channel alone and compared to the use of non-parametric approaches, which have shown to have weaker priors compared to parametric approaches. In this regard, the performances of UKF- and EKF-based methods will be compared with those of CA, of the linear Kalman filter without the previous subtraction of the reference channel signal and of the Saager's reference-channel subtraction method.

Moreover, the comparison between the proposed UKF approach and both the EKF approaches will give information on whether the fNIRS signal necessitates a highly non-linear approach (UKF) or a lower order non-linear approach (EKF) is enough for its description. The results of this comparison will highlight whether the direction taken so far (i.e. trying to estimate the noise model with higher non-linear approaches) is promising or needs to be redirected.

Comparisons between all the algorithms will be performed with both real SNR and high SNR semi-simulated dataset. We expect good performances for all methods in the high SNR dataset, while we expect a great improvement in HRF estimation for those methods using the reference-channel in the real SNR scenario. Error indexes computed between the synthetic and the estimated HRFs will be used as a metric of comparison between the different techniques.

Finally, the proposed novel UKF algorithm will be applied to real cognitive data using the dataset shown in section 2.1.

Chapter 2

Database

2.1 Experimental protocol

In this thesis, two different datasets acquired on the same participants have been employed to test a new method proposed in the next chapters. These data were obtained from seven healthy participants, who were recruited by the Optics Division at the Martinos Center for Biomedical Imaging, Massachusetts General Hospital, Boston, MA, USA. Both acquisitions were approved by the ethical committee of the Massachusetts General Hospital. In the first acquisition, each participant sat in a confortable chair and underwent two or three (depending on participant's tiredness) resting state recording sessions, each one lasting approximately 10 mins. Participants were asked to close their eyes and remain still for the entire session. These data will be used in a semi-simulation scenario to assess the performance of a new algorithm for physiological noise removal and HRF estimation proposed in the next chapters. Indeed, simulated HRFs (see paragraph 2.1.1) were added to these resting state data creating a semi-simulated dataset. Knowing the real HRF, it is possible to test the performance of the new algorithm and compute quantitative parameters to compare it in an objective way with other more known methods.

In the second acquisition, the same participants sat in a confortable chair and underwent a finger-tapping experiment, consisting of two or three sessions. In more detail, participants were asked to touch the right-hand thumb with the remaining fingers as quickly as possible. Three types of tasks were employed during the recording session , only differing in the duration of the required tapping: 2 s, 6 s and 18 s of finger-tapping, in order to estimate different shapes of the HRF. The previously described resting state measurements were recorded soon after each finger-tapping session. Between resting

state and finger tapping sessions, participants were allowed to rest and relax for a couple of minutes. In the finger tapping sessions, we are expecting brain activation to occur in the motor cortex located in the left hemisphere of the parietal lobe since activation is contralateral. Indeed, it is well known that brain activation induced by finger tapping tasks is higher in the hemisphere contralateral to the hand used for the tapping. Anyway, we also expect activation in the ipsilateral motor cortex, but it is typically much lower compared to contralateral activations. This second dataset will be used to test the method proposed in the next chapters on real cognitive data.

The first acquired subject of the dataset was excluded from the analyses due to the high presence of noise deriving from motion artifacts and bad coupling between optodes and skin in many channels. Hence, the total number of subjects actually processed in the following chapters of the thesis was 6.

Data were obtained using a continuous wave NIRS system (CW6, TechEn, Medford, MA, USA) with a sampling frequency of 50 Hz. Probes were placed bilaterally on the motor cortex located in the parietal lobe, which is usually activated during finger-tapping experiments, and bilaterally on the frontal lobe, as shown in Fig. 2.3. Red numbers represent sources, while blue ones represent detectors. In particular, red and blue numbers from 1 to 6 represent sources and detectors respectively placed on the left parietal hemisphere creating channels with 3 cm separation, red and blue numbers from 7 to 12 represent sources and detectors respectively in the right parietal hemisphere making up channels with 3 cm separation, and red numbers ranging from 13 to 15 and blue numbers from 13 to 16 represent sources and detectors in the frontal lobe of the participant's head. In addition, blue numbers ranging from 17 to 32 represent the detectors related to the reference channels, which are detectors placed 0.8 cm far from the nearby sources.

2.1.1   Generation of the semi-simulated data

In order to create the semi-simulated dataset, 36 simulated HRFs lasting approximately 8 seconds were added, for every participant, to each standard channel signal measured during the resting state session. The inter-stimulus interval (ISI) was varied between 9 and 12 seconds, so that no overlapping between two consecutive HRFs occurred. All HRFs that were added to the resting state data were determined using a linear combination of two time-dependent gamma-variant functions Γ_n:

$$HRF_{true}(t) = \alpha \cdot [\Gamma_{n_1}(t, \tau_1, \rho_1) - \beta \cdot \Gamma_{n_2}(t, \tau_2, \rho_2)] \qquad (2.1)$$

where each function was:

$$\Gamma_n(t, \tau_j, \rho_j) = \frac{1}{p! \tau_j} \left(\frac{t - \rho_j}{\tau_j} \right)^p e^{-\frac{(t-\rho_j)}{\tau_j}} \delta(t - \rho_j), \ \delta(t - \rho_j) = \begin{cases} 1 & \text{if } (t - \rho_j) \geq 0 \\ 0 & \text{otherwise} \end{cases}$$

where α controls the amplitude of the HRFs, τ_j and ρ_j control the response width and the onset time respectively, while β determines the ratio of the response to the undershoot typically found in real HRFs.

As far as the coefficients are concerned, coefficient p was set to 2 according to literature values [36], whereas the remaining parameters were varied across all stimulus onsets and time series in order to simulate HRFs with slightly different shapes and latencies, as in a real scenario case. These parameters were properly tuned in order to simulate a physiological HRF commonly found in finger-tapping tasks, and are summarized in Table 2.1.

In addition, a second semi-simulated dataset was created by adding trains of HRF characterized by much higher amplitudes than those of the first dataset. Even though we are actually adding non-physiological HRF trains, this second dataset will allow us to create a situation of higher SNR compared to the first semi-simulated dataset. SNR is commonly defined for each channel as the ratio between the amplitude of the simulated HRF and the standard deviation of the time course of the resting state signal. In particular, the mean SNR adding physiological HRFs is ≈ 0.5, while adding non-physiological HRFs led to a mean SNR which is ≈ 2.1. To create this high SNR dataset, parameters were tuned as shown in Table 2.2.

HRF tuning in the real SNR case						
Parameters	α	τ_1	ρ_1	β	τ_2	ρ_2
Values	1200 ± 10	1 ± 0.03	0.7 ± 0.003	0.5 ± 0.0001	0.81 ± 0.0001	2.1 ± 0.0001

Table 2.1: overview of the parameters (mean and standard deviation) used to create the synthetic HRFs in the real SNR case.

In particular, this tuning led to a mean HRF with peak amplitude of 325 ± 9.34 nM and a peak latency equal to 3 ± 0.05 s in the first dataset, while in the second one the tuning led to a mean HRF with peak amplitude of 1637.8 ± 47.21 nM and a peak latency equal to 2.68 ± 0.05 s.

HRF tuning in the high SNR case						
Parameters	α	τ_1	ρ_1	β	τ_2	ρ_2
Values	6000 ± 10	1 ± 0.03	0.7 ± 0.003	0.5 ± 0.0001	0.81 ± 0.0001	2.1 ± 0.0001

Table 2.2: overview of the parameters (mean and standard deviation) used to create the synthetic HRFs in the higher SNR case.
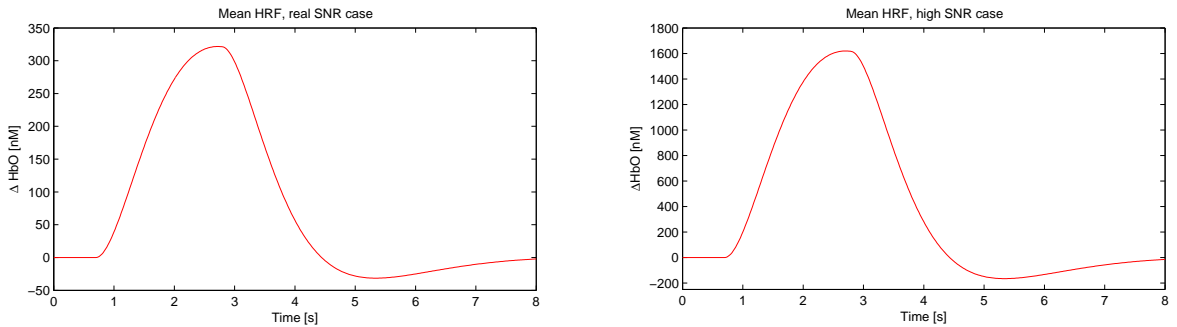
Figure 2.1: left: mean HRF computed from a HRFs train in the real SNR case. Right: mean HRF computed from a HRFs train in the high SNR case. Note the difference in amplitudes.

Two instances of mean simulated HRF computed from a sample HRFs train both in the real and high SNR case are presented in Fig. 2.1.

It is worth noting that adding synthetic HRFs to real resting state data allows to get a dataset which is much closer to a real scenario than a full simulated dataset. Indeed, in this semi-simulation scenario, we are dealing with real physiological noise, which contains many time-varying components that can be hardly simulated. At the same time, knowing the true HRF, we are also able to compute quantitative indexes which allow more accurate comparisons between different algorithms aiming at estimating the HRF. An example of a synthetic HRF train that was added to real resting state data is shown in Fig. 2.2. Looking at Fig. 2.2, we can observe the small amplitude of the HRFs compared to the entire raw signal. The signal in the top figure and the signal in the bottom figure look almost identical and no differences can be seen to the naked eye. This further highlights the difficulty of estimating such a small component, the HRF, completely hidden in the measured signal.
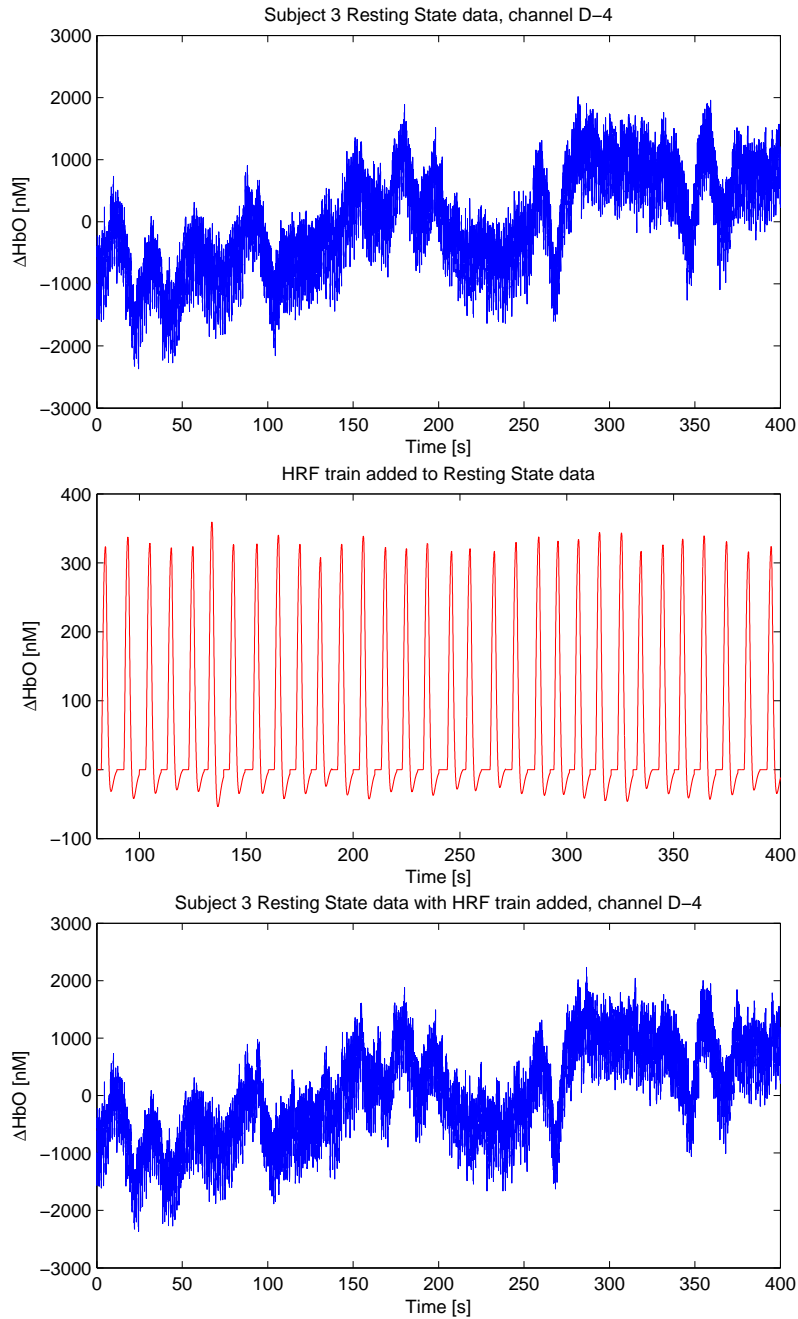
Figure 2.2: Top: real resting state data acquired from a participant. Middle: overview of the synthetic HRFs that were added to the resting state data. Bottom: the semi-simulated signal, obtained by summing the signal shown in the top figure with the HRF train shown in the middle figure.
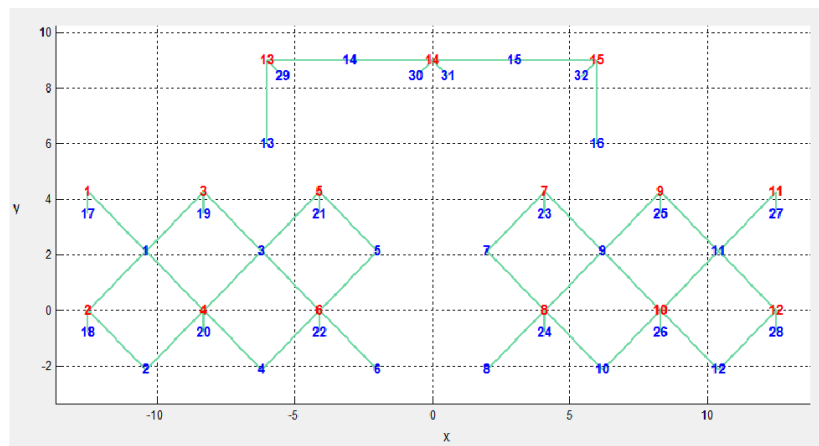
Figure 2.3: Source-detector geometry employed in the datasets: red and blue numbers represent sources and detectors respectively, whereas green lines connecting number pairs represent the corresponding measurement channel. Note the different relative distance between sources and detectors in standard channels (e.g. source 1, detector 1, 3 cm) and reference channels (e.g. source 1, detector 17, 0.8 cm).

Chapter 3

Algorithms for linear and nonlinear Kalman filtering

Theoretically, the Kalman Filter (KF) estimates the instantaneous state of a dynamic system by exploiting noisy measurements related to the state itself. It has been widely used for the control of complex dynamic systems such as manufacturing processes, aircrafts, ships and spacecraft. The solution of the estimator is recursive, i.e. the updated estimate of the state is computed from the previous state estimate and the new input data step by step. Below, we will recall the foundamentals of KF in the linear case, and review the Rauch-Tung-Striebel Smoother algorithm, which allows to improve the state estimation by exploiting and combining all the data acquired. In section 3.3 we will present a review how the method is extended to the nonlinear case.

3.1   Kalman Filter (KF) in the linear case

In this section, the derivation of the Kalman filter equations according to the original paper published by Kalman [37] is presented. Consider the block-diagram representation of a linear, discrete-time dynamical system shown in Fig. 3.1. The state vector, denoted by $\mathbf{x}_k$, is defined as the minimal set of data that is sufficient to describe the dynamical behavior of the system involved at time t_k where k denotes the discrete time step.

3.1.1   Model of the data

The state $\mathbf{x}_k$ is usually unknown and, in order to estimate it, the set of observed data denoted by the vector $\mathbf{y}_k$ is used. From a mathematical per-spective, the signal flow-graph in Fig. 3.1 embodies the following pair of

equations:
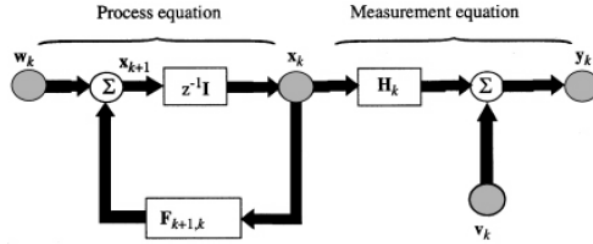
Figure 3.1: signal block-diagram representation of a linear discrete-time dynamical system.

- *Process equation*:

$$\mathbf{x}_{k+1} = \mathbf{F}_{k+1,k}\mathbf{x}_k + \mathbf{w}_k \tag{3.1}$$

where $\mathbf{F}_{k+1,k}$ is the transition matrix taking the state $\mathbf{x}_k$ from time t_k to time t_{k+1}. The process noise $\mathbf{w}_k$ is assumed to be gaussian with zero-mean and covariance matrix defined as:

$$E[\mathbf{w}_n\mathbf{w}_k^T] = \begin{cases} \mathbf{Q}_k & \text{for } n = k \\ \mathbf{0} & \text{for } n \neq 0 \end{cases} \tag{3.2}$$

where T denotes the matrix transposition. In addition, the dimension of the state space, i.e. the length of the vector $\mathbf{x}_k$, is denoted by M.

- *Measurement equation*:

$$\mathbf{y}_k = \mathbf{H}_k\mathbf{x_k} + \mathbf{v}_k \tag{3.3}$$

where $\mathbf{y}_k$ represents the measured data at time t_k, $\mathbf{H}_k$ is the measurement matrix at time t_k and $\mathbf{v}_k$ is the measurement noise at time t_k, which is assumed to be additive, white and gaussian with zero-mean and covariance matrix defined by:

$$E[\mathbf{v}_n\mathbf{v}_k^T] = \begin{cases} \mathbf{R}_k & \text{for } n = k \\ \mathbf{0} & \text{for } n \neq 0 \end{cases} \tag{3.4}$$

The measurement noise $\mathbf{v}_k$ is assumed to be uncorrelated with the process noise $\mathbf{w}_k$, and the dimension of the measurement space is denoted by N.

The problem of solving both process and measurement equations for the unknown state in an optimum manner can be summarized into exploiting the entire observed data given by vectors $\mathbf{y}_1, \mathbf{y}_2, \ldots, \mathbf{y}_k$ in order to derive for each $k \geq 1$ the minimum mean-square error estimate of the state $\mathbf{x}_i$. In particular, the problem is defined filtering if $i = k$, prediction if $i > k$ and smoothing if $1 \leq i < k$.

3.1.2   A posteriori estimation of the state vector

The Kalman filter is essentially based on a recursive prediction-correction algorithm, where, at each time step, a prediction procedure is employed and then the estimate is corrected relying on the new data acquired. Suppose that a new measurement on a linear dynamical system, described by eqs. (3.1) and (3.3), is available at time t_k. We want to use the information carried by the measurement $\mathbf{y}_k$ in order to update the estimate of the unknown state vector $\mathbf{x}_k$. Let $\hat{\mathbf{x}}_k^-$ be the a priori estimate of the state vector, derived from the prediction procedure and known at time t_k. Thus, in a prediction-correction scenario, the a posteriori estimate $\hat{\mathbf{x}}_k$ can be expressed as a linear combination of the a priori estimate $\hat{\mathbf{x}}_k^-$ and the new measurement $\mathbf{y}_k$ as:

$$\hat{\mathbf{x}}_k = \mathbf{G}_k^{(1)}\hat{\mathbf{x}}_k^- + \mathbf{G}_k\mathbf{y}_k \tag{3.5}$$

where $\mathbf{G}_k^{(1)}$ and $\mathbf{G}_k$ are unknown matrix factors which have to be determined. In order to calculate these matrices, we will use the principle of orthogonality. The state-error vector is defined as:

$$\tilde{\mathbf{x}}_k = \mathbf{x}_k - \hat{\mathbf{x}}_k \tag{3.6}$$

and exploiting the principle of orthogonality we have:

$$E[\tilde{\mathbf{x}}_k\mathbf{y}_i^T] = \mathbf{0} \text{ for } i = 1, 2, \ldots, k-1 \tag{3.7}$$

Using eqs. (3.3), (3.5), (3.6) and (3.7) we have:

$$E[(\mathbf{x}_k - \mathbf{G}_k^{(1)}\hat{\mathbf{x}}_k^- - \mathbf{G}_k\mathbf{H}_k\mathbf{x}_k - \mathbf{G}_k\mathbf{v}_k)\mathbf{y}_i^T] = \mathbf{0} \text{ for } i = 1, 2, \ldots, k-1 \tag{3.8}$$

Since process and measurement noise are uncorrelated by hypothesis, it follows that $E[\mathbf{v}_k\mathbf{y}_i^T] = \mathbf{0}$, and using this relation in eq. (3.8) and rearranging terms we get:

$$E[(\mathbf{x}_k\mathbf{y}_i^T - \mathbf{G}_k^{(1)}\hat{\mathbf{x}}_k^-\mathbf{y}_i^T - \mathbf{G}_k\mathbf{H}_k\mathbf{x}_k\mathbf{y}_i^T + (\mathbf{G}_k^{(1)}\mathbf{x}_k\mathbf{y}_i^T - \mathbf{G}_k^{(1)}\mathbf{x}_k\mathbf{y}_i^T)] = \mathbf{0} \quad (3.9)$$

$$E[(\mathbf{I} - \mathbf{G}_k\mathbf{H}_k - \mathbf{G}_k^{(1)})\mathbf{x}_k\mathbf{y}_i^T + \mathbf{G}_k^{(1)}(\mathbf{x}_k - \hat{\mathbf{x}}_k^-)\mathbf{y}_i^T] = \mathbf{0} \quad\quad (3.10)$$

where $\mathbf{I}$ is the identity matrix. From the principle of orthogonality we note that $E[(\mathbf{x}_k - \hat{\mathbf{x}}_k^-)\mathbf{y}_i^T] = \mathbf{0}$. As a consequence, eq. (3.10) can be simplified into:

$$(\mathbf{I} - \mathbf{G}_k\mathbf{H}_k - \mathbf{G}_k^{(1)})E[\mathbf{x}_k\mathbf{y}_i^T] = \mathbf{0} \text{ for } i = 1, 2, \ldots, k-1 \quad\quad (3.11)$$

For arbitrary values of the state vector $\mathbf{x}_k$ and the measurement vector $\mathbf{y}_i$, eq. (3.11) can be verified when the first factor is zero, that is in terms of $\mathbf{G}_k^{(1)}$ and $\mathbf{G}_k$:

$$(\mathbf{I} - \mathbf{G}_k\mathbf{H}_k - \mathbf{G}_k^{(1)}) = \mathbf{0} \Rightarrow \mathbf{G}_k^{(1)} = \mathbf{I} - \mathbf{G}_k\mathbf{H}_k \quad\quad (3.12)$$

Substituting eq. (3.12) into eq. (3.5) we can express the a posteriori estimate of the state vector at time t_k as:

$$\hat{\mathbf{x}}_k = \hat{\mathbf{x}}_k^- + \mathbf{G}_k(\mathbf{y}_k - \mathbf{H}_k\hat{\mathbf{x}}_k^-) \quad\quad (3.13)$$

The matrix $\mathbf{G}_k$ is named the *Kalman Gain*.

3.1.3   Derivation of the Kalman Gain

So far, we have derived the expression of the a posteriori estimate of the state. We now proceed to derive an expression for the Kalman Gain $\mathbf{G}_k$. From the principle of orthogonality we have that

$$E[(\mathbf{x}_k - \hat{\mathbf{x}}_k)\mathbf{y}_k^T] = \mathbf{0} \quad\quad (3.14)$$

Hence, it follows that:

$$E[(\mathbf{x}_k - \hat{\mathbf{x}}_k)\hat{\mathbf{y}}_k^T] = \mathbf{0} \tag{3.15}$$

where $\hat{\mathbf{y}}_k$ is a prediction estimate of $\mathbf{y}_k$ given the previous measurements $\mathbf{y}_1, \mathbf{y}_2, \ldots, \mathbf{y}_{k-1}$. We define the innovation process, which is a measure of the new information contained in $\mathbf{y}_k$ as:

$$
\begin{aligned}
\tilde{\mathbf{y}}_k = \mathbf{y}_k - \hat{\mathbf{y}}_k &= \mathbf{y}_k - \mathbf{H}_k \hat{\mathbf{x}}_k^- \\
&= \mathbf{H}_k \mathbf{x}_k + \mathbf{v}_k - \mathbf{H}_k \hat{\mathbf{x}}_k^- \\
&= \mathbf{H}_k \tilde{\mathbf{x}}_k^- + \mathbf{v}_k
\end{aligned} \tag{3.16}
$$

Then, subtracting eq. (3.15) from eq. (3.14) and using the definition of the innovation process, we get:

$$E[(\mathbf{x}_k - \hat{\mathbf{x}}_k)\tilde{\mathbf{y}}_k^T] = \mathbf{0} \tag{3.17}$$

Using eqs. (3.3) and (3.13) we can re-express the state-error vector $\mathbf{x}_k - \hat{\mathbf{x}}_k$ as:

$$
\begin{aligned}
\mathbf{x}_k - \hat{\mathbf{x}}_k &= \tilde{\mathbf{x}}_k^- - \mathbf{G}_k(\mathbf{H}_k \tilde{\mathbf{x}}_k^- + \mathbf{v}_k) \\
&= (\mathbf{I} - \mathbf{G}_k \mathbf{H}_k)\tilde{\mathbf{x}}_k^- - \mathbf{G}_k \mathbf{v}_k
\end{aligned} \tag{3.18}
$$

and substituting eqs. (3.16) and (3.18) into (3.17) we have:

$$E[\{(\mathbf{I} - \mathbf{G}_k \mathbf{H}_k)\tilde{\mathbf{x}}_k^- - \mathbf{G}_k \mathbf{v}_k\}(\mathbf{H}_k \tilde{\mathbf{x}}_k^- + \mathbf{v}_k)^T] = \mathbf{0} \tag{3.19}$$

Noting that the measurement noise $\mathbf{v}_k$ is independent of the state $\mathbf{x}_k$ and so the error $\tilde{\mathbf{x}}_k^-$, eq. (3.19) can be reduced to:

$$(\mathbf{I} - \mathbf{G}_k \mathbf{H}_k)E[\tilde{\mathbf{x}}_k \tilde{\mathbf{x}}_k^{-T}]\mathbf{H}_k^T - \mathbf{G}_k E[\mathbf{v}_k \mathbf{v}_k^T] = \mathbf{0} \tag{3.20}$$

Defining the a priori covariance matrix:

$$\mathbf{P}_k^- = E[(\mathbf{x}_k - \hat{\mathbf{x}}_k^-)(\mathbf{x}_k - \hat{\mathbf{x}}_k^-)^T] = E[\tilde{\mathbf{x}}_k^- \tilde{\mathbf{x}}_k^{-T}] \tag{3.21}$$

and recalling the definitions of eqs. (3.4) and (3.21), eq. (3.20) can be rewritten as:

$$(\mathbf{I} - \mathbf{G}_k\mathbf{H}_k)\mathbf{P}_k^-\mathbf{H}_k^T - \mathbf{G}_k\mathbf{R}_k = \mathbf{0} \qquad (3.22)$$

Solving for $\mathbf{G}_k$ we finally have:

$$\mathbf{G}_k = \mathbf{P}_k^-\mathbf{H}_k^T[\mathbf{H}_k\mathbf{P}_k^-\mathbf{H}_k^T + \mathbf{R}_k]^{-1} \qquad (3.23)$$

3.1.4   The error covariance propagation

To complete the recursive estimation procedure, we will now focus on the error covariance propagation, which describes the evolution over time of the covariance matrices of the estimation error. The propagation procedure involves two recursive stages of computation:

- 1) The a priori covariance matrix $\mathbf{P}_k^-$ at time t_k is defined by eq. (3.21). Once $\mathbf{P}_k^-$ is known, the a posteriori covariance matrix $\mathbf{P}_k$ at time t_k is determined by:

$$\mathbf{P}_k = E[\tilde{\mathbf{x}}_k\tilde{\mathbf{x}}_k^T] = E[(\mathbf{x}_k - \hat{\mathbf{x}}_k)(\mathbf{x}_k - \hat{\mathbf{x}}_k)^T] \qquad (3.24)$$

- 2) At the following time point, compute the updated a priori covariance matrix $\mathbf{P}_k^-$ given the old a posteriori covariance matrix $\mathbf{P}_{k-1}$.

In order to obtain an expression of $\mathbf{P}_k$ for the stage 1, we substitute eq. (3.18) into (3.24) and note that the noise process $\mathbf{v}_k$ is independent of the a priori estimation error $\tilde{\mathbf{x}}_k^-$ obtaining:

$$\begin{aligned} \mathbf{P}_k &= (\mathbf{I} - \mathbf{G}_k\mathbf{H}_k)E[\tilde{\mathbf{x}}_k^-\tilde{\mathbf{x}}_k^{-T}](\mathbf{I} - \mathbf{G}_k\mathbf{H}_k)^T + \mathbf{G}_kE[\mathbf{v}_k\mathbf{v}_k^T]\mathbf{G}_k^T \\ &= (\mathbf{I} - \mathbf{G}_k\mathbf{H}_k)\mathbf{P}_k^-(\mathbf{I} - \mathbf{G}_k\mathbf{H}_k)^T + \mathbf{G}_k\mathbf{R}_k\mathbf{G}_k^T \end{aligned} \qquad (3.25)$$

Expanding terms in eq. (3.25) and then using eq. (3.23), we can express the dependence of the a posteriori covariance matrix $\mathbf{P}_k$ on the a priori covariance matrix $\mathbf{P}_k^-$ in the alternative form:

$$\begin{aligned} \mathbf{P}_k &= (\mathbf{I} - \mathbf{G}_k\mathbf{H}_k)\mathbf{P}_k^- - (\mathbf{I} - \mathbf{G}_k\mathbf{H}_k)\mathbf{P}_k^-\mathbf{H}_k^T\mathbf{G}_k^T + \mathbf{G}_k\mathbf{R}_k\mathbf{G}_k^T \\ &= (\mathbf{I} - \mathbf{G}_k\mathbf{H}_k)\mathbf{P}_k^- - \mathbf{G}_k\mathbf{R}_k\mathbf{G}_k^T + \mathbf{G}_k\mathbf{R}_k\mathbf{G}_k^T \\ &= (\mathbf{I} - \mathbf{G}_k\mathbf{H}_k)\mathbf{P}_k^- \end{aligned} \qquad (3.26)$$

As far as the second stage is concerned, we first note that the a priori estimate of the state is defined in terms of the old a posteriori estimate as:

$$\hat{\mathbf{x}}_k^- = \mathbf{F}_{k,k-1}\hat{\mathbf{x}}_{k-1} \tag{3.27}$$

Therefore, using eqs. (3.1) and (3.27) we can express the a priori estimation error in an alternative form:

$$
\begin{aligned}
\tilde{\mathbf{x}}_k^- &= \mathbf{x}_k - \hat{\mathbf{x}}_k^- \\
&= (\mathbf{F}_{k,k-1}\mathbf{x}_{k-1} + \mathbf{w}_{k-1}) - (\mathbf{F}_{k,k-1}\hat{\mathbf{x}}_{k-1}) \\
&= \mathbf{F}_{k,k-1}(\mathbf{x}_{k-1} - \hat{\mathbf{x}}_{k-1}) + \mathbf{w}_{k-1} \\
&= \mathbf{F}_{k,k-1}\tilde{\mathbf{x}}_{k-1} + \mathbf{w}_{k-1}
\end{aligned} \tag{3.28}
$$

Finally, using eq. (3.28) in eq. (3.21) and noting that the process noise $\mathbf{w}_k$ is independent of $\tilde{\mathbf{x}}_{k-1}$, we obtain:

$$
\begin{aligned}
\mathbf{P}_k^- &= \mathbf{F}_{k,k-1}E[\tilde{\mathbf{x}}_{k-1}\tilde{\mathbf{x}}_{k-1}^T]\mathbf{F}_{k,k-1}^T + E[\mathbf{w}_{k-1}\mathbf{w}_{k-1}^T] \\
&= \mathbf{F}_{k,k-1}\mathbf{P}_{k-1}\mathbf{F}_{k,k-1}^T + \mathbf{Q}_{k-1}
\end{aligned} \tag{3.29}
$$

which defines the dependence of the a priori covariance matrix $\mathbf{P}_k^-$ on the old a posteriori covariance matrix $\mathbf{P}_{k-1}$.

3.1.5 Summary

Once eqs. (3.27), (3.29), (3.23), (3.13) and (3.26) have been determined, we are now able to sum up the recursive estimation of the state vector as shown in Table 3.1. It is worth noting that an initialization of the state vector $\mathbf{x}_0$ and covariance matrix $\mathbf{P}_0$ is required for the algorithm to be employed. Setting $\mathbf{x}_0 = \mathbf{0}$ and $\mathbf{P}_0$ with high values is typically a reasonable choice, but it should be adjusted to the problem to face.

So far, the state estimation has been reviewed only considering past data, that is the state vector estimation is done step by step by moving forward. The KF algorithm can also be applied in the backward direction, i.e. estimating the state vector starting from the last data and moving to the first collected data. The Rauch-Tung-Striebel Smoother is an algorithm that combines the forward and backward estimates to improve the state vector estimation, and it will be reviewed in the next section.

Table 3.1: summary of the linear Kalman filter equations

State space model:

$$\mathbf{x}_{k+1} = \mathbf{F}_{k+1,k}\mathbf{x}_k + \mathbf{w}_k$$

$$\mathbf{y}_k = \mathbf{H}_k\mathbf{x}_k + \mathbf{v}_k$$

Initialization: For $k = 0$ set

$$\hat{\mathbf{x}}_0 = E[\mathbf{x}_0]$$

$$\mathbf{P}_0 = E[(\mathbf{x}_0 - E[\mathbf{x}_0])((\mathbf{x}_0 - E[\mathbf{x}_0])^T]$$

Computation: For $k = 1, 2, ..., N$ compute:
State estimate propagation

$$\hat{\mathbf{x}}_k^- = \mathbf{F}_{k,k-1}\hat{\mathbf{x}}_{k-1}^-$$

Error covariance propagation

$$\mathbf{P}_k^- = \mathbf{F}_{k,k-1}\mathbf{P}_{k-1}\mathbf{F}_{k,k-1}^T + \mathbf{Q}_{k-1}$$

Kalman Gain Matrix

$$\mathbf{G}_k = \mathbf{P}_k^-\mathbf{H}_k^T[\mathbf{H}_k\mathbf{P}_k^-\mathbf{H}_k^T + \mathbf{R}_k]^{-1}$$

State estimate update

$$\hat{\mathbf{x}}_k = \hat{\mathbf{x}}_k^- + \mathbf{G}_k(\mathbf{y}_k - \mathbf{H}_k\hat{\mathbf{x}}_k^-)$$

Error covariance update

$$\mathbf{P}_k = (\mathbf{I} - \mathbf{G}_k\mathbf{H}_k)\mathbf{P}_k^-$$

3.2   The Rauch-Tung-Striebel Smoother

In this section we consider the smoothing problem. In particular, suppose that we are given a set of data composed of N measurements. Smoothing is a non-real time algorithm which tries to estimate the state $\hat{\mathbf{x}}_k$ exploiting all available data, that is past, present and future samples, in order to get a better estimate of the state vector $\mathbf{x}_k$. Estimation involving only past

data and the current measurement is referred to as forward filtering and its implementation has been reviewed in the previous section 3.1 and subsections 3.1.1-3.1.4. On the other hand, estimation involving only future data is referred to as backward filtering, in which estimation involves, step by step, the current measurement and all subsequent samples that are available in an off-line situation. The smoothing algorithm combines forward $\hat{\mathbf{x}}_k^f$ and backward $\hat{\mathbf{x}}_k^b$ estimates in order to get a smoothed estimate $\hat{\mathbf{x}}_k$. It is worth noting that in this section the term $\hat{\mathbf{x}}_k$ refers to the smoothed estimate at time t_k, which should not be confused with the a posteriori estimate notation used in section 3.1.

Succinctly, the measurement update equation of the Rauch-Tung-Striebel smoother is defined by:

$$\mathbf{P}_k = \mathbf{P}_k^f - \mathbf{A}_k(\mathbf{P}_{k+1}^{f-} - \mathbf{P}_{k+1})\mathbf{A}_k^T \qquad (3.30)$$

where $\mathbf{A}_k$ is the new gain matrix:

$$\mathbf{A}_k = \mathbf{P}_k^f \mathbf{F}_{k+1,k}^T [\mathbf{P}_{k+1}^{f-}]^{-1} \qquad (3.31)$$

The corresponding time update equation is defined by

$$\hat{\mathbf{x}}_k = \hat{\mathbf{x}}_k^f + \mathbf{A}_k(\hat{\mathbf{x}}_{k+1} - \hat{\mathbf{x}}_{k+1}^{f-}) \qquad (3.32)$$

Hence, the smoothing proceeds as follows:

- The Kalman filter is applied to the data in a forward manner for $k = 0, 1, 2, ..., N$ according to the theory discussed previously (see section 3.1).

- The recursive smoother is applied to the data in a backward manner for $k = N - 1, N - 2, ..., 1$ according to eqs. (3.30),(3.31) and (3.32). The Rauch-Tung-Striebel smoother is able to simultaneously perform the backward filtering and combine its estimates with the estimates of the forward filtering. Initial conditions are defined by $\mathbf{P}_N = \mathbf{P}_N^f$ and $\hat{\mathbf{x}}_k = \hat{\mathbf{x}}_k^f$.

3.3   Nonlinear case: Extended Kalman Filter (EKF)

The linear Kalman Filter can be only employed for the estimation of the state vector when we are dealing with linear systems. However, when dealing with non-linear systems, the Kalman filtering procedure can be still employed relying on a linearization procedure. The types of filters that employ this procedure are named Extended Kalman filter (EKF) and Unscented Kalman filter (UKF), which are different in the way they linearize the system under study. In particular, the EKF is based on a standard Taylor approximation of the state space model, whereas the UKF is based on a deterministic sampling approach of the state vector $\mathbf{x}_k$.

3.3.1   EKF formulation

To develop the equations of the EKF, we consider a non-linear dynamical system described by the following state-space equations:

$$\mathbf{x}_{k+1} = \mathbf{f}(k, \mathbf{x}_k) + \mathbf{w}_k \tag{3.33}$$

$$\mathbf{y}_k = \mathbf{h}(k, \mathbf{x}_k) + \mathbf{v}_k \tag{3.34}$$

where, as usual, $\mathbf{w}_k$ and $\mathbf{v}_k$ are independent zero-mean white Gaussian noise processes with covariance matrices $\mathbf{R}_k$ and $\mathbf{Q}_k$ respectively. The function $\mathbf{f}(k, \mathbf{x}_k)$ represents a non-linear transition matrix that can be time-variant, while $\mathbf{h}(k, \mathbf{x}_k)$ denotes a non-linear measurement matrix that can be time-variant as well.

The main idea of the EKF is to linearize eqs. (3.33) and (3.34) at each time point around the most recent state estimate. Once the model has been linearized, standard Kalman filter equations can be applied. In particular, linearization is pursued in two stages:

- 1) The following matrices are calculated:

$$\mathbf{F}_{k+1,k} = \left. \frac{\partial \mathbf{f}(k, \mathbf{x}_k)}{\partial \mathbf{x}} \right|_{\mathbf{x} = \hat{\mathbf{x}}_k} \tag{3.35}$$

$$\mathbf{H}_k = \left. \frac{\partial \mathbf{h}(k, \mathbf{x}_k)}{\partial \mathbf{x}} \right|_{\mathbf{x} = \hat{\mathbf{x}}_k^-} \tag{3.36}$$

This means that the ijth entry of $\mathbf{F}_{k+1,k}$ is equal to the partial derivative of the ith component of $\mathbf{f}(k, \mathbf{x}_k)$ with respect to the jth component

of $\mathbf{x}$. Likewise, the ijth entry of $\mathbf{H}_k$ is equal to the partial derivative of the ith component of $\mathbf{h}(k, \mathbf{x}_k)$ with respect to the jth component of $\mathbf{x}$. Matrices $\mathbf{F}_{k+1,k}$ and $\mathbf{H}_k$ are all known and computable by having $\hat{\mathbf{x}}_k$ and $\hat{\mathbf{x}}_k^-$ at hand at time t_k.

- 2) A first-order Taylor approximation of the non-linear functions $\mathbf{f}(k, \mathbf{x}_k)$ and $\mathbf{h}(k, \mathbf{x}_k)$ around $\hat{\mathbf{x}}_k$ and $\hat{\mathbf{x}}_k^-$ respectively, can be calculated. Matrices $\mathbf{F}_{k+1,k}$ and $\mathbf{H}_k$ are known since they have been computed in the first stage. The non-linear functions are approximated as:

$$\mathbf{f}(k, \mathbf{x}_k) \approx \mathbf{f}(k, \hat{\mathbf{x}}_k) + \mathbf{F}_{k+1,k}(k, \hat{\mathbf{x}}_k) \tag{3.37}$$

$$\mathbf{h}(k, \hat{\mathbf{x}}_k) \approx \mathbf{h}(k, \hat{\mathbf{x}}_k^-) + \mathbf{H}_{k+1,k}(k, \hat{\mathbf{x}}_k^-) \tag{3.38}$$

Then, using eqs. (3.37) and (3.38), we are able to approximate eqs. (3.33) and (3.34) , obtaining:

$$\mathbf{x}_{k+1} \approx \mathbf{F}_{k+1,k}\mathbf{x}_k + \mathbf{w}_k + \mathbf{d}_k \tag{3.39}$$

$$\bar{\mathbf{y}}_k \approx \mathbf{H}_k\mathbf{x}_k + \mathbf{v}_k \tag{3.40}$$

where

$$\bar{\mathbf{y}}_k = \mathbf{y}_k - [\mathbf{h}(k, \hat{\mathbf{x}}_k^-) - \mathbf{H}_k\hat{\mathbf{x}}_k^-] \tag{3.41}$$

$$\mathbf{d}_k = \mathbf{f}(k, \hat{\mathbf{x}}_k) - \mathbf{F}_{k+1,k}\hat{\mathbf{x}}_k \tag{3.42}$$

are all known at time t_k. Given the linearized state-space model of eqs. (3.39) and (3.40), we can then proceed and apply the linear Kalman filter theory presented in Section 3.1 to derive the equations of the EKF, which are briefly shown in Table 3.2.

Table 3.2: summary of the Extended Kalman filter equations

State space model:

$$\mathbf{x}_{k+1} = \mathbf{f}(k, \mathbf{x}_k) + \mathbf{w}_k$$
$$\mathbf{y}_k = \mathbf{h}(k, \mathbf{x}_k) + \mathbf{v}_k$$

where $\mathbf{w}_k$ and $\mathbf{v}_k$ are independent, zero mean, Gaussian noise processes of covariance matrices $\mathbf{Q}_k$ and $\mathbf{R}_k$ respectively.

Definitions:

$$\mathbf{F}_{k+1,k} = \left. \frac{\partial \mathbf{f}(k, \mathbf{x}_k)}{\partial \mathbf{x}} \right|_{\mathbf{x}=\hat{\mathbf{x}}_k}$$

$$\mathbf{H}_k = \left. \frac{\partial \mathbf{h}(k, \mathbf{x}_k)}{\partial \mathbf{x}} \right|_{\mathbf{x}=\hat{\mathbf{x}}_k^-}$$

Initialization: For $k = 0$ set

$$\hat{\mathbf{x}}_0 = E[\mathbf{x}_0]$$
$$\mathbf{P}_0 = E[(\mathbf{x}_0 - E[\mathbf{x}_0])((\mathbf{x}_0 - E[\mathbf{x}_0])^T]$$

Computation: For $k = 1, 2, ..., N$ compute:
State estimate propagation

$$\hat{\mathbf{x}}_k^- = \mathbf{f}(k, \hat{\mathbf{x}}_{k-1})$$

Error covariance propagation

$$\mathbf{P}_k^- = \mathbf{F}_{k,k-1}\mathbf{P}_{k-1}\mathbf{F}_{k,k-1}^T + \mathbf{Q}_{k-1}$$

Kalman Gain Matrix

$$\mathbf{G}_k = \mathbf{P}_k^- \mathbf{H}_k^T [\mathbf{H}_k \mathbf{P}_k^- \mathbf{H}_k^T + \mathbf{R}_k]^{-1}$$

State estimate update

$$\hat{\mathbf{x}}_k = \hat{\mathbf{x}}_k^- + \mathbf{G}_k \mathbf{y}_k - \mathbf{h}(k, \hat{\mathbf{x}}_k^-)$$

Error covariance update

$$\mathbf{P}_k = (\mathbf{I} - \mathbf{G}_k \mathbf{H}_k)\mathbf{P}_k^-$$

3.3.2 Use for HRF estimation

The Kalman filtering procedure previously discussed will be used in the proposed method to estimate physiological noise that contaminates fNIRS signals. In more detail, parameters of a noise model will be estimated step by step adopting the nonlinear Kalman filtering approach. The EKF approach was proposed in fNIRS studies [35], but its performance were sub-optimal, probably due to linearization issues. Hence, an alternative approach is needed for further studies and insights.

3.4 Nonlinear case: Unscented Kalman Filtering (UKF)

3.4.1 The idea of UKF

Over the last 20-30 years, the EKF has been used as a standard technique when dealing with non-linear dynamic systems. The EKF applies the standard linear Kalman filter methodology to a linearization of the non-linear system. However, this approach is sometimes sub-optimal, and might also lead to divergence. Indeed, the EKF state distribution is approximated to a Gaussian random variable (GRV) which is then propagated through the first-order linearization step. This may cause suboptimal performances of the filter due to errors in the true posterior mean and covariance of the transformed GRV. In addition, the linearization is substantially accurate only under the assumption of small variations between the optimum estimate $\hat{\mathbf{x}}_{k-1}$ at time t_{k-1} and the one at time t_k.

The Unscented Kalman Filter (UKF) is another implementation of the Kalman filtering approach in a non-linear scenario and was first proposed by Julier et al. [38] [39] and then further developed by Wan and van der Merwe [40] [41]. Basically, it tries to overcome the EKF approximation issues by using a deterministic sampling approach to calculate mean and covariance terms.

The state distribution is again represented by a GRV, but it is now specified using a minimal set of chosen sample points. These sample points capture the true mean and covariance of the GRV, and when the state is propagated through the non-linear system, they capture the posterior mean and covariance to the second order approximation (Taylor series expansion). Before continuing the discussion, it is important to explain the Unscented Transformation.

3.4.2   The Unscented Transformation

The Unscented Transformation (UT) is a method for computing the statistical description of a random variable which undergoes a non-linear transformation. Let $\mathbf{x}$ be a random variable of dimension L, mean $\bar{\mathbf{x}}$ and covariance $\mathbf{P}_x$ in a non-linear function, $\mathbf{y} = \mathbf{f}(\mathbf{x})$. In order to determine the statistics of $\mathbf{y}$, we compute a matrix $\bar{\chi}$ composed of $2L + 1$ sigma vectors χ_i as follows:

$$
\begin{aligned}
\chi_0 &= \bar{\mathbf{x}} \\
\chi_i &= \bar{\mathbf{x}} + (\sqrt{(L+\lambda)\mathbf{P}_x})_i \text{ for } i = 1, ..., L \\
\chi_i &= \bar{\mathbf{x}} - (\sqrt{(L+\lambda)\mathbf{P}_x})_{i-L} \text{ for } i = L+1, ..., 2L
\end{aligned}
\tag{3.43}
$$

where $\lambda = \alpha^2(L + \kappa) - L$ is a scaling parameter. The constant α controls the spread of the sigma points around the mean $\bar{\mathbf{x}}$, and it is usually set to small positive values (typically $10^{-4} \leq \alpha \leq 1$), κ is a secondary scaling parameter which is usually set to $3 - L$ and β is used to incorporate prior knowledge of the distribution of $\mathbf{x}$ (for Gaussian distributions it has been demonstrated that $\beta = 2$ is optimal). $(\sqrt{(L+\lambda)\mathbf{P}_x})_i$ is the ith column of the matrix square root (i.e. lower-triangular Cholesky factorization).
These sigma vectors are then propagated through the non-linear function:

$$
\Upsilon_i = \mathbf{f}(\chi_i) \text{ for } i = 0, ..., 2L
\tag{3.44}
$$

and the mean and covariance of $\mathbf{y}$ are approximated using a weighted sample mean and covariance of the posterior sigma points, that is:

$$
\bar{\mathbf{y}} \approx \sum_{i=0}^{2L} W_i^m \Upsilon_i
\tag{3.45}
$$

$$
\mathbf{P}_y \approx \sum_{i=0}^{2L} W_i^c (\Upsilon_i - \bar{\mathbf{y}})(\Upsilon_i - \bar{\mathbf{y}})^T
\tag{3.46}
$$

where weights W_i are given by

$$
\begin{aligned}
W_0^{(m)} &= \frac{\lambda}{L + \lambda} \\
W_0^{(c)} &= \frac{\lambda}{L + \lambda} + 1 - \alpha^2 + \beta \\
W_i^{(m)} &= W_i^{(c)} = \frac{1}{2(L + \lambda)} \text{ for } i = 1, ..., 2L
\end{aligned}
\tag{3.47}
$$

The first set of weights $W_i^{(m)}$ is used to compute the first order moment (the mean) and the second set of weights $W_i^{(c)}$ is used to compute the second order moment (the covariance). The algorithm is summarized in Fig. 3.2, where the mean vector $\bar{\mathbf{x}}$ and covariance matrix $\mathbf{P}_x$ are given. Then, the set of sigma points χ_i are computed and propagated through the nonlinear function $\mathbf{f}()$, obtaining the transformed points $\mathbf{y_i}$. Finally, the statistics of the transformed random variable $\mathbf{y}$ is calculated relying on a weighted sample mean and covariance procedure. For a better understanding, an example of UT is shown in Fig. 3.3, where mean and covariance of a two-dimensional system are propagated through the non linear function $\mathbf{f}(\cdot)$. Fig. 3.3 (a) shows the true mean and covariance transformation relying on Monte Carlo sampling, while Fig. 3.3 (b) shows the same result but using a linearization procedure as in the EKF and finally Fig. 3.3 (c) depicts the actual UT employed in the UKF equations. As we can see from the figure, the linearization procedure used in the EKF is less accurate compared to the UT adopted in the UKF procedure, which propagates the specified set of sigma points through the nonlinear function $\mathbf{f}(\cdot)$ and then applies a weighted sample mean and covariance.
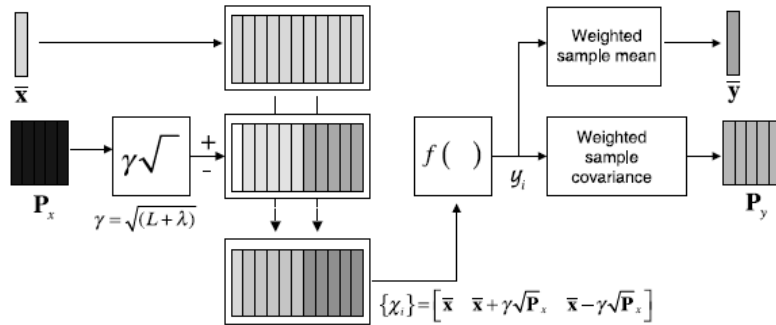
Figure 3.2: block-diagram representation of the UT algorithm used to determine the statistics of the random variable $\mathbf{y}$ starting from $\mathbf{x}$, when a non linear transformation f($\cdot$) is employed. Taken from [42].

3.4.3   Method equations

The UKF is a straightforward extension of the UT, and it is shown in Table 3.3. It is worth noting that this particular implementation does not require any Jacobian calculations and the complexity of the algorithm is the same
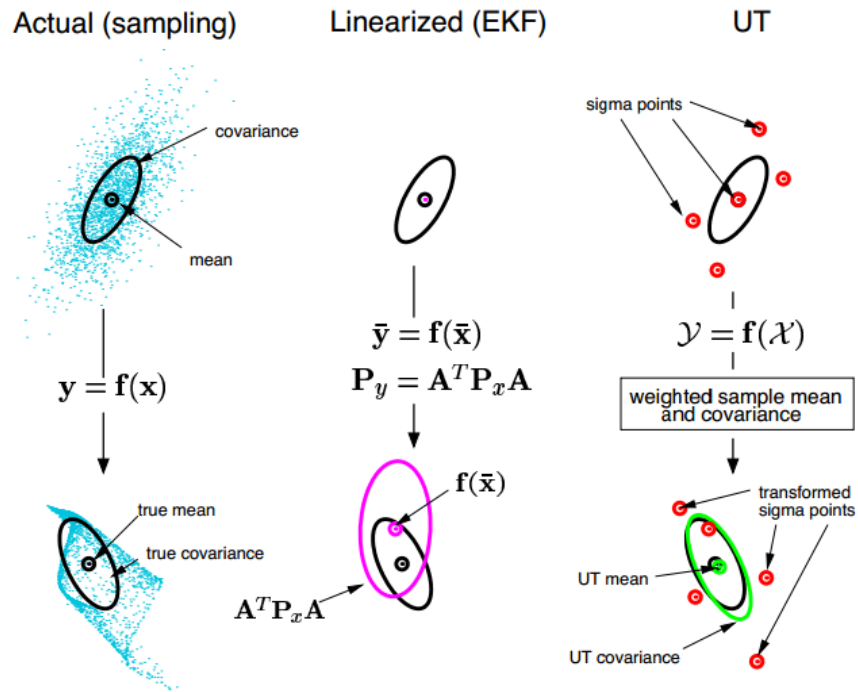
Figure 3.3: An example of the UT for the propagation of the mean and covariance through the non linear function $\mathbf{f}(\cdot)$.(a) actual Monte Carlo sampling, (b) linearized transformation and (c) UT. Taken from [42].

as the EKF.

Table 3.3: Overview of the Unscented Kalman filter algorithm

Initialize with:

$$\hat{\mathbf{x}}_0 = E[\mathbf{x}_0]$$
$$\mathbf{P}_0 = E[(\mathbf{x}_0 - E[\mathbf{x}_0])((\mathbf{x}_0 - E[\mathbf{x}_0])^T]$$

For $k = 1, 2, ..., N$

compute the sigma points:

$$\chi_{k-1} = \begin{bmatrix} \hat{\mathbf{x}}_{k-1} & \hat{\mathbf{x}}_{k-1} + \gamma\sqrt{\mathbf{P}_{k-1}} & \hat{\mathbf{x}}_{k-1} - \gamma\sqrt{\mathbf{P}_{k-1}} \end{bmatrix}$$

Time-update equations:

$$\chi_{k|k-1}^* = \mathbf{F}(\chi_{k-1})$$
$$\hat{\mathbf{x}}_k^- = \sum_{i=0}^{2L} W_i^{(m)} \chi_{i,k|k-1}^*$$
$$\mathbf{P}_k^- = \sum_{i=0}^{2L} W_i^{(c)} (\chi_{i,k|k-1}^* - \hat{\mathbf{x}}_k^-)(\chi_{i,k|k-1}^* - \hat{\mathbf{x}}_k^-)^T + \mathbf{R}^v$$

augment sigma points:

$$\chi_{k|k-1} = \begin{bmatrix} \chi_{k|k-1}^* & \chi_{0,k|k-1}^* + \gamma\sqrt{\mathbf{R}^v} & \chi_{0,k|k-1}^* - \gamma\sqrt{\mathbf{R}^v} \end{bmatrix}$$
$$\mathbf{\Upsilon}_{k|k-1} = \mathbf{H}(\chi_{k|k-1})$$
$$\hat{\mathbf{y}}_k^- = \sum_{i=0}^{2L} W_i^{(m)} \mathbf{\Upsilon}_{i,k|k-1}$$

and the measurement update equations are:

$$\mathbf{P}_{\tilde{y}_k\tilde{y}_k} = \sum_{i=0}^{2L} W_i^{(c)} (\mathbf{\Upsilon}_{i,k|k-1} - \hat{\mathbf{y}}_k^-)(\mathbf{\Upsilon}_{i,k|k-1} - \hat{\mathbf{y}}_k^-)^T + \mathbf{R}^n$$
$$\mathbf{P}_{\mathbf{x_k y_k}} = \sum_{i=0}^{2L} W_i^{(c)} (\chi_{i,k|k-1} - \hat{\mathbf{x}}_\mathbf{k}^-)(\chi_{i,k|k-1} - \hat{\mathbf{x}}_k^-)^T$$
$$\mathbf{G}_k = \mathbf{P}_{x_k y_k} \mathbf{P}_{\tilde{y}_k\tilde{y}_k}^{-1}$$
$$\hat{\mathbf{x}}_k = \mathbf{x}_k^- + \mathbf{G}_k(\mathbf{y}_k - \hat{\mathbf{y}}_k^-)$$
$$\mathbf{P}_k = \mathbf{P}_k^- - \mathbf{G}_k \mathbf{P}_{\tilde{y}_k\tilde{y}_k} \mathbf{G}_k^T$$

where $\gamma = \sqrt{L + \lambda}$, λ is the composite scaling parameter, L is the state dimension, $\mathbf{R}^v$ is the process-noise covariance, $\mathbf{R}^n$ is the measurement noise covariance and W_i are the weights calculated using eq. (3.46).

3.5   Conclusive remarks

To summarize, the EKF has been a widely accepted and standard method in non-linear control and estimation contexts. In this chapter, we have presented, along with the classic linear Kalman filter theory, an alternative approach to the EKF for non-linear systems, i.e. the UKF. The UKF tries to overcome the approximation issues of the EKF by using a deterministic sampling approach, where a minimal set of chosen sample points are propagated through the non-linear system, capturing the posterior mean and covariance, and achieving an equal or better level of performance (depending on the non-linearity of the system) at a comparable level of complexity in its implementation.

In the next chapter, the implementation of the novel method proposed in this thesis will be presented. In particular, this is a parametric method, where a specific model is employed and its parameters are estimated at each sample time using a Kalman Filter.

Chapter 4

Novel UKF-based algorithm for HRF estimation from fNIRS signals

4.1 The main steps of the algorithm

According to the discussion made in previous chapters, the fNIRS signal contains many physiological components that act like background noise, especially the Mayer's wave, which, due to the overlapping of its frequency spectrum with that of the evoked brain activity, makes HRF estimation really hard. In this chapter the key steps of the novel algorithm will be presented along with its actual implementation based on the Kalman filtering theory presented in the previous chapter. The method is composed of three main steps. The first step is a preprocessing step, while the other two steps perform the actual Kalman filter-based algorithm. In the second step, the UKF is applied to the reference-channel signal in order to estimate physiological noise, which is assumed to pollute the standard channels nearby; the estimated noise is then subtracted from the standard channel signals. In the third step, a linear Kalman filter is applied to the corrected standard channel signal in order to estimate the HRFs.

To summarize, the steps performed by the algorithm for each acquired standard channel, are the following and they will be later described thoroughly:

- **S**tep 1: pre-processing of the raw standard channel and correlated reference channel signals using a band pass filter and scaling of the reference channel.

- **S**tep 2: Unscented Kalman filter applied to the reference channel signal in order to estimate physiological noise and subtraction of the estimated noise model from the corresponding standard channel signal, obtaining a corrected standard channel signal.

- **S**tep 3: linear Kalman filter and smoother applied to the previous corrected standard channel signal for the estimation of the HRFs and final block-average for the estimation of the mean HRF.

An overview of the entire algorithm is displayed in the block-diagram scheme in Fig. 4.1.

4.2   Step 1: pre-processing stage

Raw intensity data were converted into concentration changes using some of the Homer2 fNIRS analysis package functions [43].

Both the standard and the reference channel signals were high-pass filtered at 0.01 Hz to remove any slow drifts and low-pass filtered at 1.25 Hz in order to remove instrument noise. The filter used was a 3rd order Butterworth-type digital filter, and cut-off frequencies were chosen not to affect the HRF components, which typically lie in the 0.1-0.5 Hz spectrum band.

For every standard channel, the Pearson's correlation coefficient between the standard channel and every reference channel located in the same hemisphere was computed. Each standard channel was associated with the reference channel showing the highest correlation coefficient.

Afterwards, the reference channel signal was scaled in a least squares sense. Indeed, the amplitude of the reference channel is sometimes higher than that of the corresponding standard channel one because of the different path-length followed by the light in the two types of channels. Scaling is necessary to compensate this difference in the path-length factors. In particular, a linear regression between the reference and standard channel signals was employed taking into account the first 30 seconds of acquisition. In the first 30 seconds of acquisition we did not add any simulated HRF, avoiding thus the possible overfitting problem that occurred in the Saager's reference channel subtraction method [31]. In a real scenario, acquiring 30 seconds of resting state data before starting the cognitive paradigm is surely feasible. Defining the first 30 s of the standard channel signal as $\mathbf{LS}_0$ and the first 30 s of the reference channel signal as $\mathbf{SS}_0$ in vector form, we have:

$$\mathbf{SS}_0 = \alpha \cdot \mathbf{LS}_0 \Rightarrow \hat{\alpha} = (\mathbf{LS}_0^T \cdot \mathbf{LS}_0)^{-1} \cdot \mathbf{LS}_0^T \cdot \mathbf{SS}_0 \qquad (4.0)$$
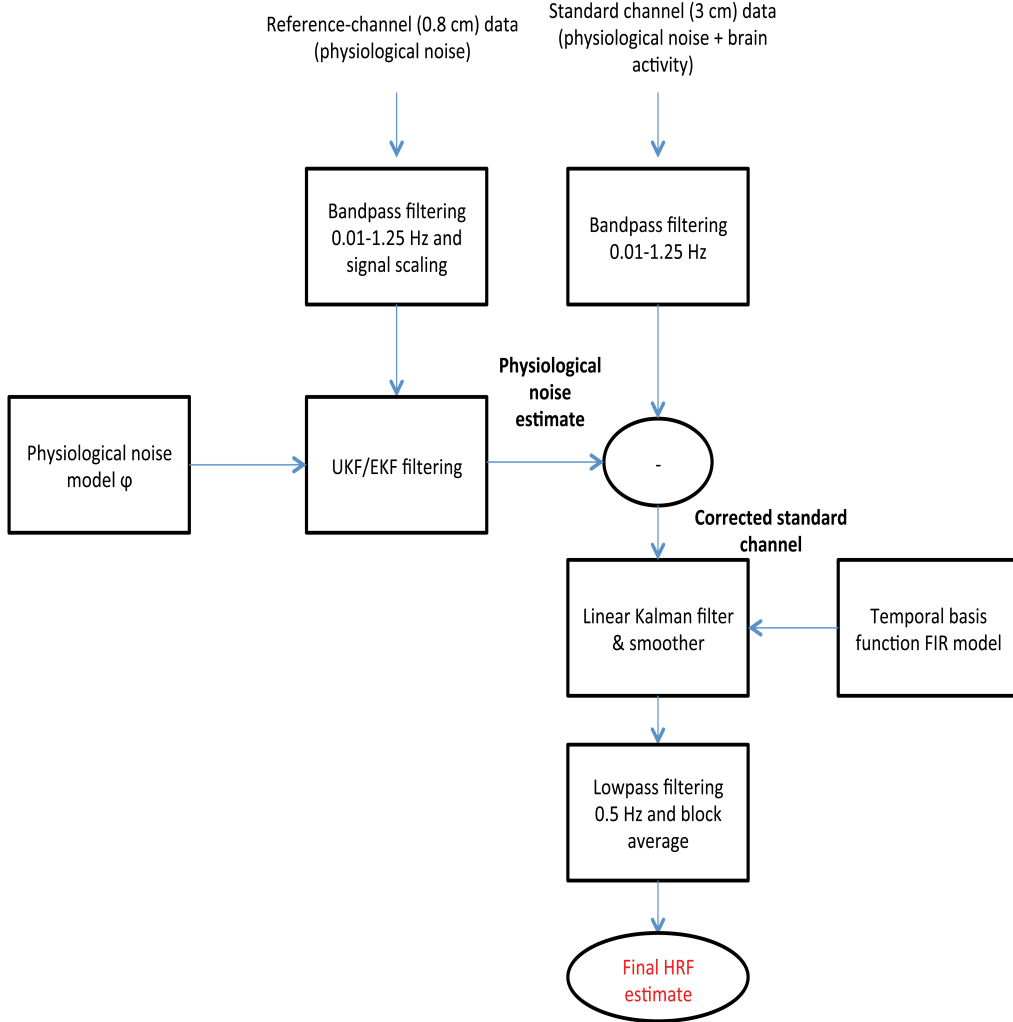
Figure 4.1: block-diagram scheme representing the main steps of the novel UKF-based algorithm proposed in this thesis.

$\hat{\alpha}$ was used to scale the entire reference channel signal as:

$$\mathbf{SS}_{scaled} = \frac{\mathbf{SS}}{\hat{\alpha}} \qquad (4.0)$$

An example of reference channel signal before and after the scaling is displayed in Fig. 4.2.
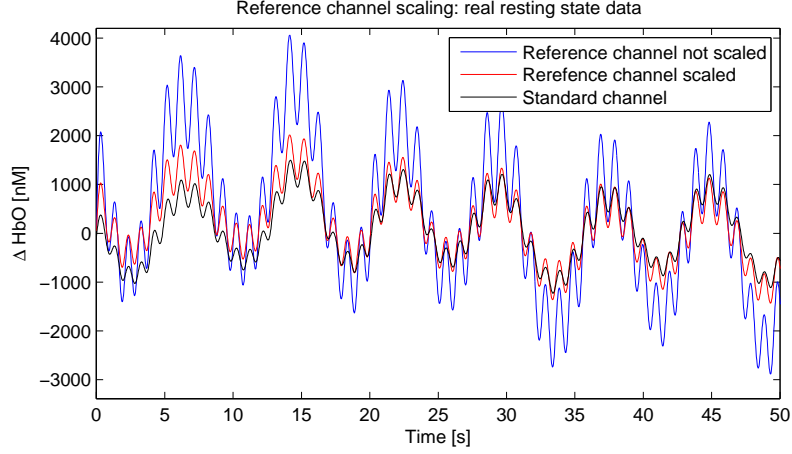
Figure 4.2: an overview of the scaling procedure on real resting state data. Note the higher amplitude of the reference channel signal compared to the standard channel signal before the scaling took place.

4.3   Step 2: UKF for the estimation of physiological noise from reference-channel data

This step was performed only if the correlation coefficient between the reference and the standard-channel signals was greater than 0.6, otherwise this step was skipped and the algorithm went directly to step 3. This was due in order not to potentially increase the noise in the time series as demonstrated in [34].

At this stage, the UKF is applied to the reference channel signal in order to estimate physiological noise.

4.3.1   Physiological noise modeling

The physiological components, that have been presented in section 1.4 and act like noise in fNIRS data, can be modeled as a sum of M sinusoidal waves:

$$\phi(t) = \sum_{i=1}^{M} a_i sin(2\pi f_i t + \theta_i) + c \tag{4.0}$$

where a_i are the amplitudes of the sinusoids, f_i the frequencies, θ_i the phases and c is the offset, which are all assumed to be time-varying. In this thesis, different physiological noise models were tested, and thus M was set to 1,2 or 3 to model only the Mayer's wave, or both Mayer's wave and respiratory

waves or both Mayer's wave, respiratory waves and cardiac oscillations, respectively. It is to note that M could be any integer, but its maximum was set up to 3 because we are actually interested in modeling only low frequency components that overlap with the HRF spectrum. Hence, physiological noise was modeled as:

$$\phi_1(t) = a_1 sin(2\pi f_1 t + \theta_1) + c \tag{4.0}$$

$$\phi_2(t) = a_1 sin(2\pi f_1 t + \theta_1) + a_2 sin(2\pi f_2 t + \theta_2) + c \tag{4.0}$$

$$\phi_3(t) = a_1 sin(2\pi f_1 t + \theta_1) + a_2 sin(2\pi f_2 t + \theta_2) + a_3 sin(2\pi f_3 t + \theta_3) + c \tag{4.0}$$

We want to estimate the parameters a_i, f_i, θ_i and c using the physiological noise models above and the Unscented Kalman filter applied on the reference channel fNIRS data. Hence, the state vector at time t_k is composed of the unknown time varying parameters, that is:

$$\mathbf{x}_{k_1} = \begin{bmatrix} a_1 & f_1 & \theta_1 & c \end{bmatrix}^T$$

$$\mathbf{x}_{k_2} = \begin{bmatrix} a_1 & f_1 & \theta_1 & a_2 & f_2 & \theta_2 & c \end{bmatrix}^T$$

$$\mathbf{x}_{k_3} = \begin{bmatrix} a_1 & f_1 & \theta_1 & a_2 & f_2 & \theta_2 & a_3 & f_3 & \theta_3 & c \end{bmatrix}^T$$

where the subindexes 1,2 and 3 refer to the number of sinusoids employed. At every step, the transition matrix $\mathbf{F}_{k+1,k}$ is assumed to be an identity matrix. This means that we are using a random walk model, due to the fact that no a priori information is substantially available about the variation of the parameters over time. Finally, the non linear function $\mathbf{h}(k, \mathbf{x}_k)$ is represented by the physiological model ϕ_i of eqs. (4.3.1), (4.3.1) and (4.3.1).

Thus, the state space equations involved are:

$$\begin{cases} \mathbf{x}_{k+1} = \mathbf{F}_{k+1,k}\mathbf{x}_k + \mathbf{w}_k \\ \mathbf{y}_k = \mathbf{h}(\mathbf{x}_k) + \mathbf{v}_k \end{cases}$$

where $\mathbf{h}(\mathbf{x}_k) = \sum_{i=1}^{M} a_i sin(2\pi f_i + \theta_i) + c$, M=1,2,3 according to the model employed, $\mathbf{w}_k \in N(\mathbf{0}, \lambda_w^2)$ and $\mathbf{v}_k \in N(0, \sigma_v^2)$

4.3.2   UKF tuning

The estimate $\hat{\mathbf{x}}_k$ at each time step t_k is computed using the UKF followed by the Rauch-Tung-Striebel smoother. However, the Kalman filter recursions require the initialization of the state vector estimate $\hat{\mathbf{x}}_0$ and estimated state covariance $\mathbf{P}_0$. In this study, the initial estimate $\hat{\mathbf{x}}_0$ was obtained by fitting

physiological noise models ϕ_i of eqs. (4.3.1), (4.3.1) and (4.3.1) on the first 30 seconds of data acquisition with the non linear least squares. In particular, the MatLab function LSQNONLIN was used. Initial values of the parameters (a_i, f_i, θ_i, c) were set according to Table 4.1. It is worth noting that fixed initial values for parameters a_i and c are not possible due to the fact that the initial signal is highly variable across all participants.

	Parameter inizialization for the non linear least squares: models ϕ_1, ϕ_2 and ϕ_3									
Parameters	a_1 (nM)	f_1 (Hz)	θ_1	a_2 (nM)	f_2 (Hz)	θ_2	a_3 (nM)	f_3 (Hz)	θ_3	c (nM)
Values for model ϕ_1	max(data)	0.1	10	-	-	-	-	-	-	mean(data)
Values for model ϕ_2	max(data)	0.1	10	max(data)	0.2	10	-	-	-	mean(data)
Values for model ϕ_3	max(data)	0.1	10	max(data)	0.2	10	max(data)	1	10	mean(data)

Table 4.1: overview of the initialization of the parameters for the non linear least squares method for the three physiological models.

Once all parameters have been determined, the covariance matrix of the error estimates was calculated as $\Sigma_{\tilde{p}} = (\mathbf{J}^T\mathbf{J})^{-1}$, where $\mathbf{J}$ is the jacobian returned by the LSQNONLIN function, and then $\mathbf{P}_0$ was set to a diagonal matrix containing the variances of the estimates. The UKF algorithm was run twice on the data and the initial covariance estimate for the second run was set to the final covariance estimate of the first run. Running the filter twice makes the method less sensitive to the initial guess of $\mathbf{P}_0$. In addition, statistical covariance priors need to be calculated as well, both for the state process noise cov$(\mathbf{w}_k)$=$\mathbf{Q}$ and measurement noise cov$(\mathbf{v}_k)$=$\mathbf{R}$. Practically, the process noise determines how much the states are allowed to vary over time, and in this work, $\mathbf{Q}$ was set as a diagonal matrix containing the following values, according to literature [33][44]:

- $[10^{-10}\ 10^{-10}\ 10^{-15}\ 20]$

- $[10^{-10}\ 10^{-10}\ 10^{-15}\ 10^{-10}\ 10^{-10}\ 10^{-15}\ 20]$

- $[10^{-10}\ 10^{-10}\ 10^{-15}\ 10^{-10}\ 10^{-10}\ 10^{-15}\ 10^{-10}\ 10^{-10}\ 10^{-15}\ 20]$

when dealing with ϕ_1, ϕ_2 and ϕ_3 respectively.

As far as $\mathbf{R}$ is concerned, it determines how well we trust measurements during the filtering algorithm. It was chosen to be time-varying in order to make it self-tunable. Indeed, it is known that fNIRS signal is stationary in small intervals of about 1 second. Thus, the covariance $\mathbf{R}$ was estimated computing the variance of the data contained in a sliding window of length 1

second while the filter proceeds forward with 70% overlap between adjacent windows to reduce noise. Hence, while the filtering time t_k is contained in the window, $\mathbf{R}$ is set to the variance of the data contained in the window itself, otherwise the window is shifted forward and a new value for $\mathbf{R}$ is determined, iteratively.

The UKF algorithm described above gives in output the estimated physiological noise model $\mathbf{y}_{filt}$. This noise model can be subtracted from the corresponding standard channel signal $\mathbf{y}_r$, obtaining the corrected standard channel signal $\mathbf{y}_c$ as:

$$\mathbf{y}_c = \mathbf{y}_r - \mathbf{y}_{filt}$$

An example of physiological noise signal and corrected standard channel signal can be found in Fig. 4.3, where we can appreciate the reduction of low drifts of the signal after the correction.

4.4   Step 3: estimation of the HRF by parametric approach

In order to get the final estimates of the HRFs, a linear Kalman filter was applied to the corrected data (or to the non-corrected data if no reference channel was sufficiently correlated with the standard channel signal).

4.4.1   Hemodynamic response function modeling

Hemodynamic response functions at sample time t_k were modeled as a set of temporal basis functions, that is:

$$h(t_k) = \sum_{i=1}^{N} w_i \cdot b_i(t_k) \tag{4.-1}$$

where $b_i(t)$ are 15 normalized gaussian functions with a standard deviation of 0.5 s and means separated by 0.5 s (see chapter 1, Fig. 1.6). These values were chosen to model a temporal window of 8 seconds, which correponds to the duration of the HRFs that were added to the semi-simulated dataset.

4.4.2   Standard channel modeling

In the linear Kalman filter the corrected standard channel signal $y_c(t)$ was modeled as a linear convolution between the hemodynamic response $h(t)$ of
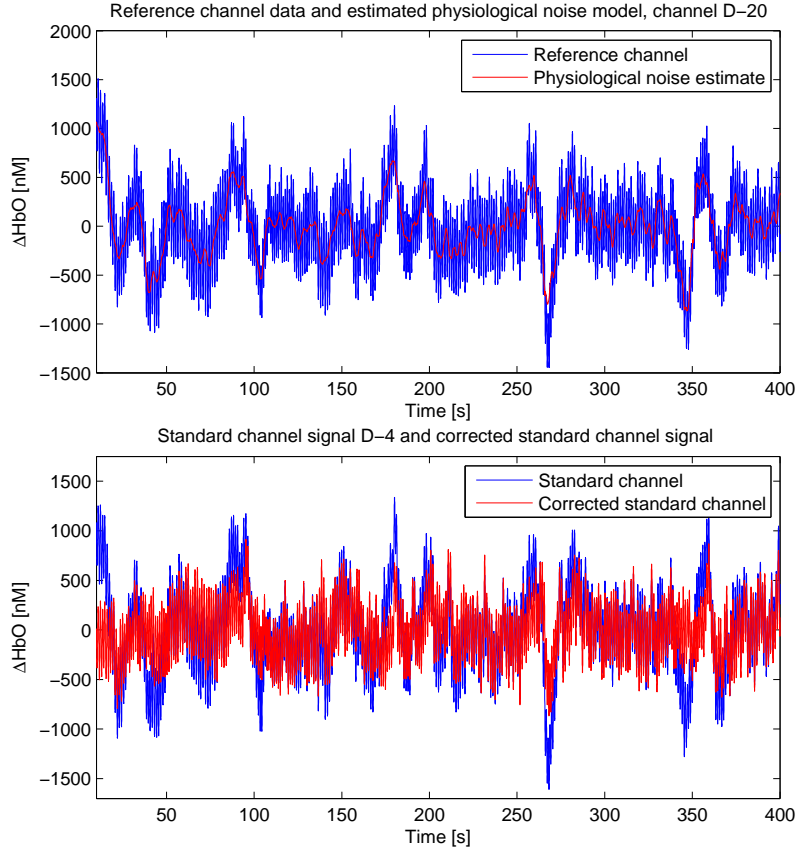
Figure 4.3: left: physiological noise estimate (red line) obtained by using the UKF followed by the RTS smoother on the reference-channel data (blue line) of a sample subject. Right: corresponding standard channel signal (blue line) and corrected standard channel signal (red line) obtained by subtracting the physiological noise estimate computed from the reference-channel data. Channel notation and probe geometry can be found in chapter 2, Fig. 2.3.

eq. (4.4.1) and an onset vector $u(t)$ as:

$$y_c(t) = \sum_{k=-\infty}^{+\infty} h(k) \cdot u(t-k) \tag{4.-1}$$

$u(t)$ is a binary vector which takes the value of 1 only at the time when the stimulus is presented, otherwise it is zero. Therefore, in this case, we are actually modeling $y_c(t)$ as the output of a linear system, in which the impulse response is represented by the HRF of eq. (4.4.1) and the input by $u(t)$.

The main idea is to define a state space equation that allows the estimation at each time step of the weights w_i for $i = 1, 2, ..., 15$, which represent the amplitudes of the gaussian functions. Thus, eqs. (4.4.1) and (4.4.2) need to be re-expressed in a state space form to define the linear Kalman filter formulation.

4.4.3   Parametric estimation problem: state-space formulation

The state-space equations of the linear Kalman filter can be summarized as follows:

$$\begin{cases} \mathbf{x}_{k+1} = \mathbf{F}_{k+1,k}\mathbf{x}_k + \mathbf{w}_k \\ \mathbf{y}_k = \mathbf{H}_k\mathbf{x}_k + \mathbf{v}_k \end{cases}$$

where the state space vector $\mathbf{x}_k$ is now composed by the 15 weights w_i defined previously, which have to be determined. $\mathbf{F}_{k+1,k}$ is, again, an identity matrix since we do not have a priori information about the variation of the weights, while $\mathbf{H}_k$ is a time-varying transition matrix, which corresponds to the kth row of the matrix A, whose columns are the linear convolution between the onset vector $u(t)$ and each temporal basis function $b_i(t)$, as:

$$A = \begin{bmatrix} u(t_1) \otimes b_1(t_1) & u(t_1) \otimes b_2(t_1) & \ldots & u(t_1) \otimes b_{15}(t_1) \\ u(t_2) \otimes b_1(t_2) & u(t_2) \otimes b_2(t_2) & \ldots & u(t_2) \otimes b_{15}(t_2) \\ \vdots & \vdots & \vdots & \vdots \\ u(t_N) \otimes b_1(t_N) & u(t_N) \otimes b_2(t_N) & \ldots & u(t_N) \otimes b_{15}(t_N) \end{bmatrix}$$

Again, the tuning of the filter is required for its running. In particular, the initial state vector $\mathbf{x}_0$ was obtained by fitting the 15 temporal basis functions to the mean HRF determined by applying a block-average procedure, where all trials containing the HRF were averaged. For a more reliable fit, a linear least squares method was employed with the constraint that all weights to be estimated must be positive. This is really important in the application of the filter on real cognitive data, since the real averaged trial could be partially negative due to the presence of noise, and this could lead to an erroneous estimation of one or more weights as negative. Once weights $\hat{w}_i$ are determined, then $\mathbf{x}_0 = [\hat{w}_1 \ \hat{w}_2 \ \ldots \ \hat{w}_{15}]$. State covariance matrix $\mathbf{P}_0$, instead, was set to be a diagonal matrix whose entries were equal to 10^{-1} as suggested in [33].

Process noise covariance matrix $\mathbf{Q}$ was assumed to be diagonal with entries equal to 10^{-15} for the first 5 and last 5 weights, while entries corresponding to the remaining weights were set to 10^{-4} similarly to [33]. The rationale behind this choice was the fact that it is reasonable to assume very low variations of the state weights corresponding to the initial and final part of the HRF, whereas the weights that model the middle peak should be more variable across trials. Indeed, variations in the HRF are commonly found in its peak amplitude and peak latency.

The measurement noise covariance matrix $\mathbf{R}$, was set to 100. This value was empirically determined noting that assigning higher values to $\mathbf{R}$ ($\approx$ 10000) led to the estimation of a perfect HRF since the filter did not take into account data, but it relied only on the HRF model. Conversely, lower values of $\mathbf{R}$ (≈ 10) led to a non physiological estimation of the HRF due to the fact that the filter, in this case, relied more on the noisy data rather than the model. In the former case, the filter was able to estimate a perfectly shaped HRF even when the HRF was not actually added to the data, while in the latter case HRF estimation was always non-physiological. Hence, a trade-off value was set according to the fact that the filter should be able to estimate the HRF when this is present in the standard channel signal and at the same time it should be able to estimate the absence of the HRF when a particular channel is sampling a brain region not activated. Different values for $\mathbf{R}$ were analyzed in different channels and subjects, yielding the final value of 100. As for the UKF, the filter was run twice in order to make it less sensitive to initial guesses of $\mathbf{P}_0$. In addition, to improve the accuracy of HRF estimation, the Rauch-Tung-Striebel smoother was applied in the backward direction, obtaining the smoothed estimate $\hat{\mathbf{x}}_k$. Every HRF trial was estimated at every time t_k using the temporal basis set contained in $\mathbf{H}_k$ and the smoothed estimate $\hat{\mathbf{x}}_k$ as:

$$\hat{h}(t_k) = \mathbf{H}_k \cdot \hat{\mathbf{x}}_k$$

Each trial was then baseline-corrected by subtracting the mean calculated in the first 0.5 s from the onset and band-pass filtered (0-0.5 Hz) to lower residual noise that could be still present. An overview of the HRF estimation from the semi-simulated dataset can be found in Fig. 4.4.

The algorithms developed in this thesis were implemented and run using MatLab$^{\text{©}}$ (version R2012a, The Mathworks, Natick, Massachussetts, USA).
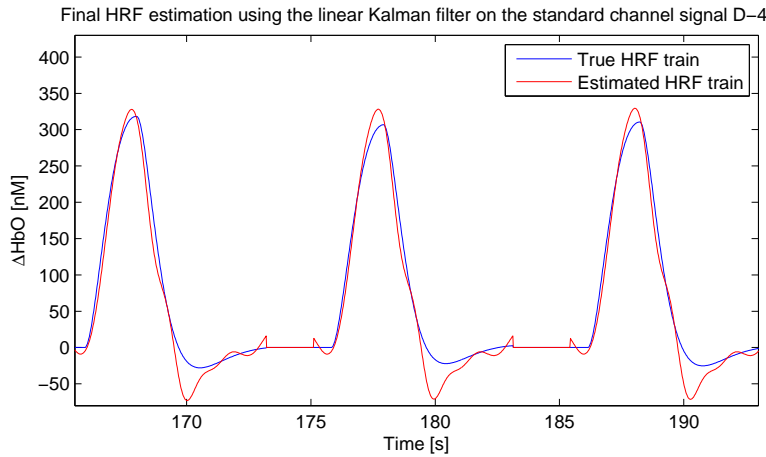
Figure 4.4: example of estimation of a HRF train added to a particular standard channel signal. Zoom in the [165 - 193] s time window.

4.5 Methods used for comparison

In order to assess and test the performance of the UKF-based approach proposed in this thesis, a comparison with the following literature methods implemented and applied to the same dataset was performed.

4.5.1 EKF-based approaches

This method was initially implemented and tested in [35] on fully simulated data. Succinctly, this method adopts the EKF in order to estimate physiological noise from reference-channel data using the same physiological model of eq. (4.3.1). The single sinusoid model aimed at estimating very low frequency oscillations and the Mayer's wave. Then, subtraction of the estimated noise model from the corresponding standard channel signal was employed and HRFs were finally estimated using the standard linear Kalman filter. This algorithm is very similar to the UKF-based algorithm implemented in this thesis, with the main difference of using the EKF instead of the UKF for physiological noise estimation.

In addition, a new version of the EKF-based approach was formulated in this thesis. The EKF algorithm was reviewed and modified in order to estimate a physiological noise model composed of 2 or 3 sinusoids, instead of just 1 sinusoid, as in the original formulation. The increased number of sinusoids aims at the estimating the respiratory and cardiac waves, respectively, under the hypothesis that a more complex model should better describe the non linear and complex fNIRS signal.

4.5.2   Linear Kalman Filter (LKF)

In order to isolate the improvement achieved by the subtraction of the physiological noise model estimated by the UKF, a linear Kalman filter approach, identical to step 3 of the proposed algorithm, but not preceded by the subtraction of the noise model (step 2 of the proposed algorithm), was employed as further parametric comparison method. This method is similar also to the one implemented in [33], but without taking into account the reference channel.

4.5.3   Saager's method

For a thorough description of this method, see section 1.5.3. In particular, Saager's method is a non-parametric approach, which exploits the reference channel signal. The comparison between UKF and Saager's method can provide information on the improvements achieved by parametric approaches vs. non-parametric approaches when the reference channel is used to reduce physiological noise.

4.5.4   CA

The comparison with CA (see section 1.5.2) can provide insights into the importance of the reduction of physiological noise for better HRF estimation and into the improvements achieved by parametric approaches. To perform CA, data were pre-filtered with a band-pass filter (0.01-0.5 Hz) to remove any slow drifts, cardiac and respiratory oscillations and instrumentation noise, and then all trials belonging to the same task were averaged and the mean HRF was further low-pass filtered at 0.5 Hz to remove any residual noise potentially present.

Chapter 5

Implementation in the semi-simulated scenario

The proposed method and the other literature methods previously described in chapter 4, were tested on the semi-simulated dataset presented in section 2.1. The dataset was created intentionally adding synthetic HRFs to real resting state data. THis approach allows to quantify the accuracy of each method in the estimation of the entire HRF and other clinical parameters derived from it, such as peak amplitude and peak latency. It is worth noting that HRF trains were added to all standard channel signals for each subject, independently from their actual location on the participant's head. Indeed, we were not interested in detecting brain activation at this point, but rather in quantifying the performances of each method, thus maximizing the number of channels to work on.

Initially, all methods were run and tested in an ideal condition of high signal-to-noise ratio, in which HRFs added had an amplitude of ≈ 1637 nM. Once the accuracy in recovering the HRF was demonstrated by all methods in this ideal scenario, all methods were then tested in a condition of signal-to-noise ratio similar to the real scenario one, by reducing the amplitude of the added HRFs to ≈ 325 nM.

5.1 Semi-simulated dataset with high SNR

This dataset was acquired recruiting 7 participants (one excluded due to excessive noise in the data) who underwent one or more resting state acquisitions, for a total of 12 processed acquisitions. Higher than normal (likely non-physiological) HRF trains were added in this high SNR semi-simulation scenario in order to test all methods and quantify the performances of the

algorithms in an ideal condition. An overview of the ability of the novel proposed UKF-based algorithm in the estimation of single trial HRFs can be appreciated in Fig. 5.1 for subject 4.
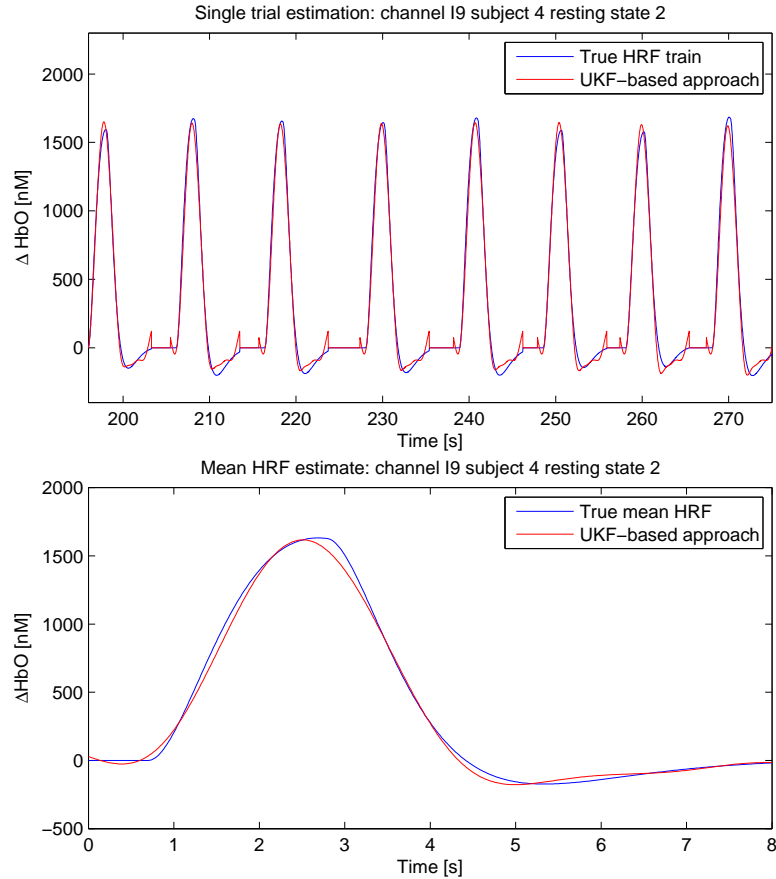
Figure 5.1: Top: true single trial HRFs (blue line) and single trial HRFs estimated with the proposed UKF-based algorithm (red line) in one channel of subject 4 (zoom in the [196-278] s time window, standard channel (source 9 - detector 9), SS channel used in the UKF-based physiological noise removal algorithm (source 9 - detector 25)). Bottom: true mean HRF (blue line) and mean HRF estimate (red line) computed by averaging all single trial estimates obtained with the proposed UKF-based algorithm.

As we can appreciate from Fig. 5.1, the proposed UKF-based method is able to accurately recover the signel trial HRFs added to the resting state data. The mean estimated HRF is very accurate and similar to the true one.

In Fig. 5.2 an example of single trials HRFs estimated with all the other literature methods is shown, together with the mean HRF computed by each

method averaging the single trial responses. A detail of a particular subject and channel is shown.
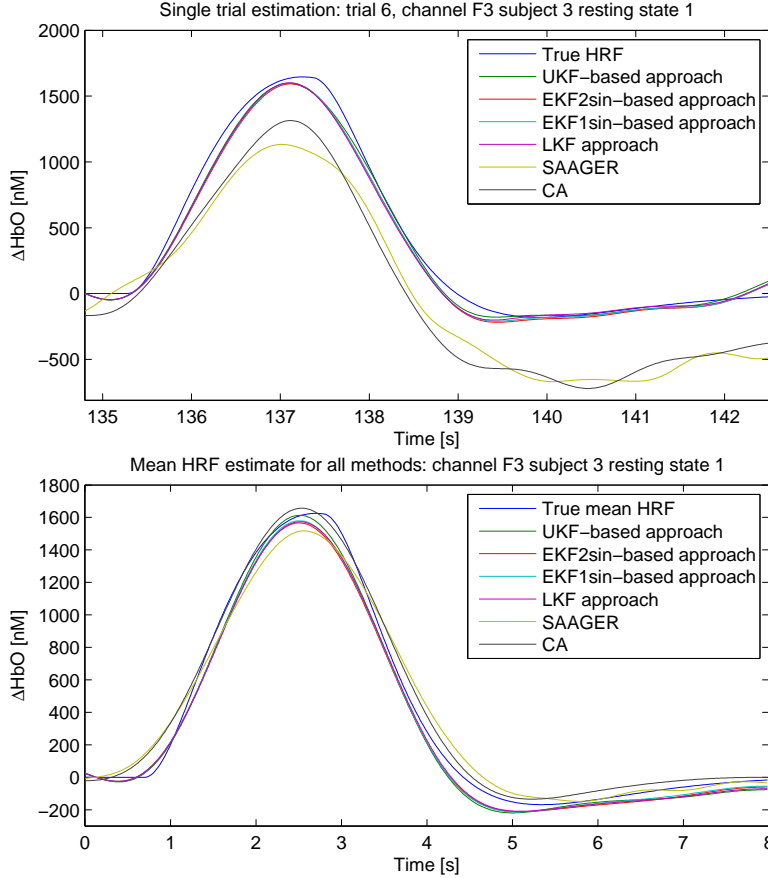
Figure 5.2: Top: true single trial HRFs (blue line) along with single trial HRFs estimated with all the methods in one channel of a particular subject (zoom in the [134.9-142.6] s time window, standard channel source 6 - detector 3, SS channel used in the UKF-based physiological noise removal algorithm (source 4 - detector20)). Bottom: true mean HRF (blue line) and mean HRF estimates computed by averaging all single trial estimates obtained with all methods in the same subject and channel.

From Fig. 5.2 it is clear that all methods achieve a good performance in the estimation of the mean HRF. However, particular differences in performance are not yet visible at this point, because we are still dealing with an ideal case of good SNR.

In order to objectively assess the performance of the proposed UKF-based method and compare that with the other techniques, the percentage

estimation error was computed for all subjects and all channels as:

$$E = 100 \cdot \frac{\parallel u_{true} - \bar{u} \parallel^2}{\parallel u_{true} \parallel^2}$$

where $\bar{u}$ is the mean HRF obtained by averaging all single trial estimates and u_{true} is the real and known mean HRF actually added to the data. The percentage estimation error gives a quantitative assessment of how good is the technique in recovering the HRF profile shape. The more the profile shape of the recovered HRF is similar to the true one, the lower the percentage estimation error is. Furthermore, other two parameters derived from the mean HRF and useful in clinical applications, the peak amplitude and peak latency, were computed for all subjects and channels. To compare the performances of the techniques in recovering these parameters, the error committed in their estimation was computed. These errors are the peak percentage error and the peak latency percentage error, defined respectively as:

$$E_{peak} = 100 \cdot \frac{\mid peak(u_{true}) - peak(\bar{u}) \mid}{\mid peak(u_{true}) \mid} \quad E_{latency} = 100 \cdot \frac{\mid lat(u_{true}) - lat(\bar{u}) \mid}{\mid lat(u_{true}) \mid}$$

Table 5.1 reports the percentage estimation errors, the percentage peak errors and the percentage peak latency error obtained with the proposed UKF-based method and all the other techniques used for the comparison in the case of high SNR. Fig. 5.4 reports a bar graph with the mean error values and their standard deviations for the three error metrics and all techniques computed across subjects, where, as mentioned in section 2.1, the first subject was deleted due to excessive noise present in the data deriving from a bad coupling between optodes and skin. Statistical significance at the $p < 0.05$ and $p < 0.01$ levels (two-tailed paired t-test) is illustrated by purple and red lines over the bars, respectively.

As we can see from the results shown, in the ideal case of high SNR all methods implemented run correctly and give very low indexes of error, revealing the great accuracy in the recovery of the HRF. In particular, the UKF-based, the two EKF-based approaches as well as the LKF approach give similar results ($\approx 2.5\%$ for the estimation error, $\approx 4\%$ for the peak estimation error and $\approx 7\%$ for the peak latency estimation error). Saager's subtraction method performs slightly worse in the estimation of the HRF profile and its peak amplitude, while performing better in the estimation

Percentage errors for the high SNR condition								
Subject	UKF			EKF2sin			EKF1sin		
	$E(\%)$	$E_{peak}(\%)$	$E_{lat}(\%)$	$E(\%)$	$E_{peak}(\%)$	$E_{lat}(\%)$	$E(\%)$	$E_{peak}(\%)$	$E_{lat}(\%)$
Subject 2 RS1	4	6.5	6.9	3.5	6	6.8	3.6	5.9	6.9
Subject 2 RS2	2.5	5.1	7	2.5	5	7	2.4	4.8	
Subject 3 RS1	1	3.1	7.1	1	2.9	7.2	1.1	3	7.2
Subject 3 RS2	1	2.6	7.2	0.9	3.1	7.3	0.9	2.9	7.1
Subject 4 RS1	1	3.8	6.5	0.9	2.7	6.6	0.7	2.4	6.6
Subject 4 RS2	0.6	1.9	6.9	0.6	2.5	6.8	0.7	2.3	6.9
Subject 4 RS3	1.1	2.6	6.9	1	2.9	6.8	0.8	2.7	6.7
Subject 5 RS1	2.9	4.8	6.6	2.81	4.9	6.7	2.78	4.7	6.9
Subject 6 RS1	1.6	3.8	7	1.7	3.1	7.1	2	3.5	7.2
Subject 6 RS2	1.3	3.8	6.8	1.2	3.8	6.7	1.2	3.6	6.8
Subject 7 RS1	3.3	4.9	6.8	2.5	4.3	6.9	2.7	4.5	6.9
Subject 7 RS2	9.9	6.8	6.9	8.2	5.7	7.1	8.7	5.5	7
Mean	2.5	4.1	6.9	2.2	3.9	6.9	2.3	3.8	6.9
Sd	2.5	1.5	0.2	2	1.1	0.2	2.2	1.2	0.1
Subject	KLF			SAAGER			CA		
	$E(\%)$	$E_{peak}(\%)$	$E_{lat}(\%)$	$E(\%)$	$E_{peak}(\%)$	$E_{lat}(\%)$	$E(\%)$	$E_{peak}(\%)$	$E_{lat}(\%)$
Subject 2 RS1	3.5	5.9	7.1	4.4	8.1	6	4.8	8.7	6.3
Subject 2 RS2	2.6	5.2	7	4.8	7.8	6.2	5.7	6.8	6.2
Subject 3 RS1	1.2	3.1	7.2	1.4	4.7	5.9	1.4	3.3	6.6
Subject 3 RS2	0.9	2.9	7.2	1.5	4.8	5.8	1.4	3.9	6.6
Subject 4 RS1	7	5.8	8.2	2.1	5.7	5.1	7.3	6.3	7.1
Subject 4 RS2	1.1	2.9	6.2	2.2	5.5	4.7	10.2	10.7	4.1
Subject 4 RS3	1.2	3.6	6.6	1.8	6.5	5	3.2	7	6.3
Subject 5 RS1	2.6	4.9	6.9	4.9	6.5	6	4.6	5.5	6.5
Subject 6 RS1	1.2	3.5	7.1	3	6.4	5.2	3	5.7	6.3
Subject 6 RS2	2.1	5.6	6.9	2.6	7.7	5.2	2.5	6	6.5
Subject 7 RS1	1.3	3.9	6.8	2.4	5.5	5.4	2.3	3.8	6.1
Subject 7 RS2	1.4	3.4	7	1.7	6.6	5.5	2.4	6.4	6.5
Mean	2.2	4.2	7	2.7	6.3	5.5	4.1	6.2	6.3
Sd	1.7	1.1	0.4	1.2	1.1	0.4	2.6	2	0.7

Table 5.1: Percentage errors for total HRF, peak amplitude and peak latency with mean and standard deviation calculated across all subjects available for all methods in the high SNR condition.

of the peak latency. Finally, CA performs worse than all other methods in recovering the HRF profile ($\approx 4\%$ estimation error).

For each of the three error metrics, a series of paired t-tests was employed to understand whether the results obtained with the different techniques are statistically significant. As expected, in this high SNR condition, no

statistical significant differences were detected for the error index E, but for the comparison between the linear Kalman filter and CA ($p < 0.02$). For the peak error E_{peak} index, both the UKF, the EKF with 2 sinusoids, the EKF with 1 sinusoid and the linear Kalman filter perform significantly better than Saager's method ($p < 0.001$ for all methods) and CA ($p < 0.03$ for all methods). Finally, as far as the latency error $E_{latency}$ index is concerned, all the linear and nonlinear Kalman approaches perform significantly better than Saager's method and CA ($p < 0.02$ for all methods). No statistical significant differences were detected among the Kalman approaches.

5.2   Semi-simulated dataset with SNR similar to the real one

Once all methods were successfully employed in the high SNR case, another simulation was run in a more real SNR situation by adding physiological HRF trains with a lower amplitude compared to the high SNR case study. An overview of the results obtained with the novel proposed UKF-based algorithm and the comparison techniques in the estimation of single trial HRFs as well as in the estimation of the mean HRF can be seen in Fig. 5.5 and Fig. 5.6.

Figure 5.3: top: bar graph of the mean values obtained across all subjects for the index of error E in the high SNR situation. Middle: bar gr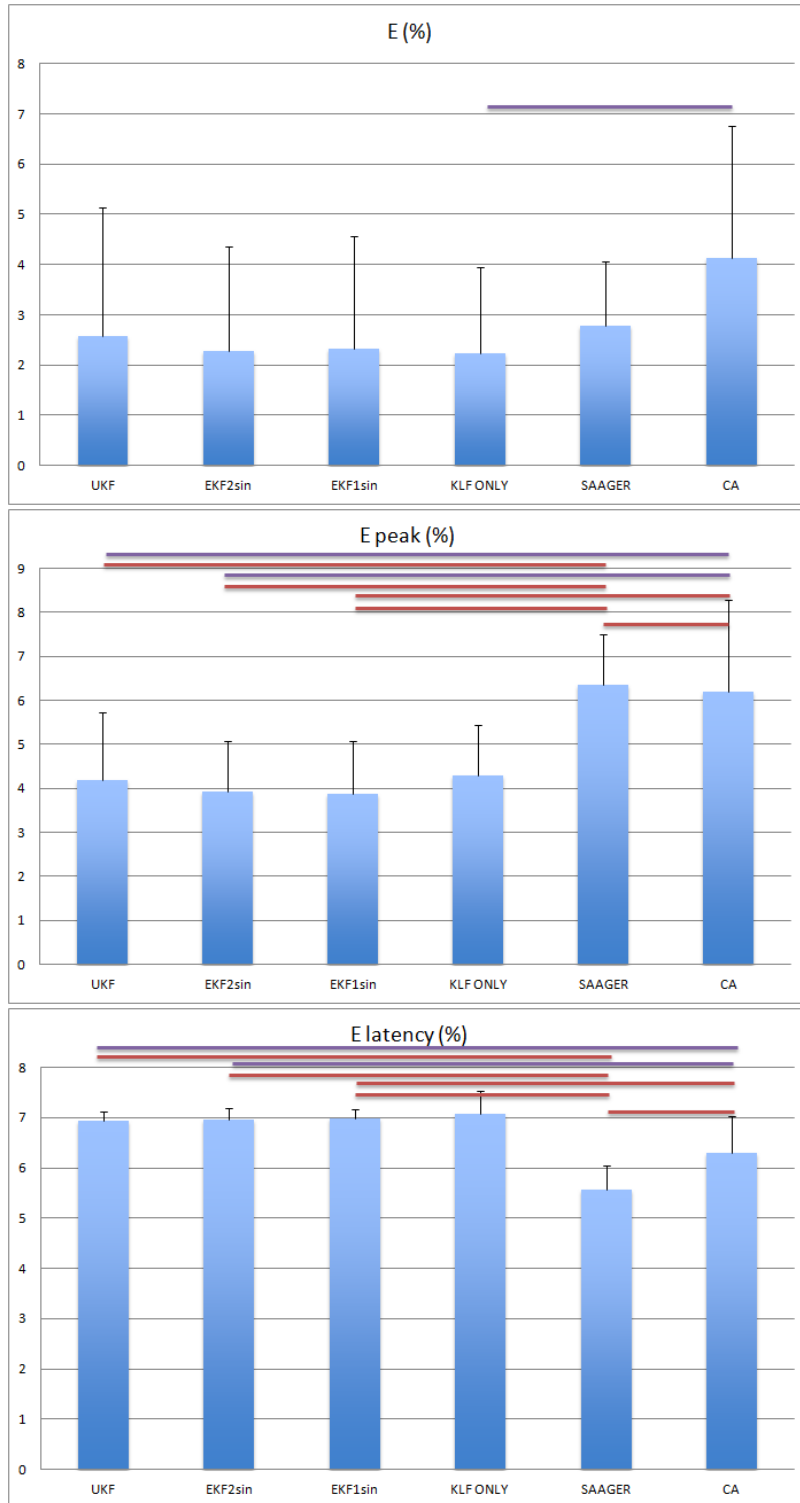aph of the mean values obtained across all subjects for the index of error E_{peak} in the high SNR situation. Bottom: bar graph of the mean values obtained across all subjects for the index of error E_{lat} in the high SNR situation. Statistical significance at the $p < 0.05$ and $p < 0.01$ levels (two-tailed paired t-test) is illustrated by purple and red lines over the bars, respectively.
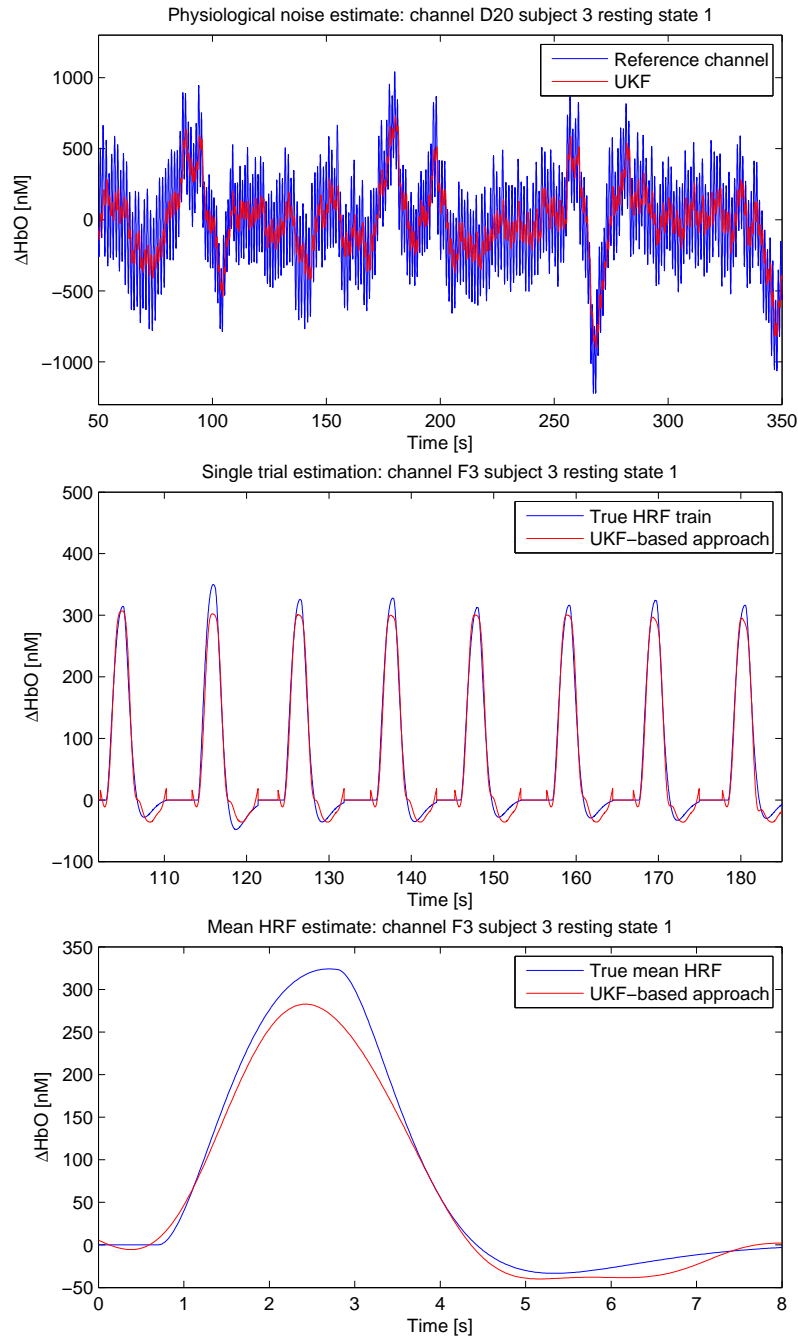
Figure 5.4: top: Unscented Kalman filtering results (red line) for the estimation of physiological noise from reference channel data (blue line) for a particular subject (zoom in the [50-350] s time window, reference channel source 4 - detector 20). Middle: single trial estimates obtained with the UKF-based proposed algorithm (red line) with the HRF train (blue line) added to the resting state data (zoom in the [100-185] s time window, standard channel source 6 - detector 3, which is correlated with the standard channel signal shown in the top figure). Bottom: mean HRF estimate (red line) obtained by averaging all single trial estimates, superposed to the true mean HRF (blue line).

As we can see from Figs. 5.5 and 5.6, the proposed UKF-based method is able to detect with very great accuracy both the single trial HRFs added to resting state data and the mean HRF estimate obtained by averaging the single trial estimates. Comparing the HRF estimate obtained with the proposed method and the true one, we can appreciate their similarity in the whole recovered shape. Nevertheless, the recovered HRF is less accurate compared to the one recovered in the high SNR scenario, as expected.

In addition, from Fig. 5.7, we can appreciate how the other EKF-based techniques are able to accurately detect the single trial HRFs as well as the mean HRF. Saager's method achieves good results, but its HRF estimate is slightly worse compared to the one of the nonlinear kalman filter based methods, above all in the estimate of single trial HRFs. The linear Kalman filter method recovers good shaped HRFs, both at the single trial level and at the mean level; however, its performance is worse than the ones of the reference channel-based methods, likely due to its inability in removing physiological noise oscillations. Finally, the performance of CA is the worst one; the main reasons are its non parametric approach and the inability to remove physiological noise oscillations.

Also in this scenario, the percentage estimation error, the peak error and the peak latency error were computed for all subjects and all channels to objectively test the performances of the different techniques and compare them. Table 5.2 reports for each subject the mean errors across channels for the proposed UKF-based method and the other methods used for comparison. Fig. 5.8 reports the bar graph of the mean error indexes computed across all subjects in the real SNR situation, where statistical significance at the $p < 0.05$ and $p < 0.01$ levels (two-tailed paired t-test) is illustrated by purple and red lines over the bars, respectively.

Looking at Table 5.2 and the bar graph in Fig. 5.8, differences in terms of performance of the techniques can be now appreciated quantitatively and they mirror the qualitative results previously described in Fig. 5.4 and 5.5. In particular, CA has the highest error index ($\approx 75\%$ for the total estimation error). Indeed, this method does not rely on any model in the estimation of the HRF and so its performance is limited. The linear Kalman filter approach works worse than the the nonlinear Kalman approaches and Saager's method, but it is definitely better than CA. Indeed, LKF adopts a prior model for estimating the HRF and this improves its performance compared to the non-parametric CA approach. However, LKF does not perform any physiological noise reduction before estimating the HRF. Hence, Saager's method works

Percentage errors for the real SNR scenario								
Subject	**UKF**			**EKF2sin**			**EKF1sin**		
	$E(\%)$	$E_{peak}(\%)$	$E_{lat}(\%)$	$E(\%)$	$E_{peak}(\%)$	$E_{lat}(\%)$	$E(\%)$	$E_{peak}(\%)$	$E_{lat}(\%)$
Subject 2 RS1	34.4	21	10.7	33.6	20.5	10.4	34.9	21.5	10.6
Subject 2 RS2	20.5	16.2	9.1	17.5	14.5	8.7	17.3	15.8	8.7
Subject 3 RS1	6.8	7.7	6.3	6.9	6.9	6.6	7.6	7.3	6.7
Subject 3 RS2	9.8	10.1	7.6	11.5	11	7.8	9.9	8.7	7.3
Subject 4 RS1	15.5	12.7	7.3	15.2	14.6	6.1	15.7	12.4	5.9
Subject 4 RS2	9.2	10.6	7	10	10.9	6.4	9.9	9.9	6.5
Subject 4 RS3	11.5	11.7	6.9	10.4	10	7.3	7.8	9.3	7.4
Subject 5 RS1	28.4	22.5	8.6	26.5	20.5	9.2	26.1	21.2	9
Subject 6 RS1	17.9	10.4	7	22.1	10	8	26.1	10.4	8.4
Subject 6 RS2	20	13.4	8.3	18.2	16.6	7.6	15.8	15.6	7.1
Subject 7 RS1	17.7	16.6	7.4	13	14	7.5	16.6	13.7	7.9
Subject 7 RS2	37.1	24.4	9.7	33.1	20.1	18	40.3	22	9.5
Mean	19.1	14.8	8	18.2	14.1	8.6	19	14	7.9
Sd	9.8	5.4	1.3	8.9	4.5	3.1	10.6	5.2	1.3
Subject	**KLF**			**SAAGER**			**CA**		
	$E(\%)$	$E_{peak}(\%)$	$E_{lat}(\%)$	$E(\%)$	$E_{peak}(\%)$	$E_{lat}(\%)$	$E(\%)$	$E_{peak}(\%)$	$E_{lat}(\%)$
Subject 2 RS1	33.8	20.5	10.9	67.5	24.5	11.1	87.1	28.1	12.3
Subject 2 RS2	20.7	13.4	8.1	39.6	22.1	7.7	65.8	25.6	8
Subject 3 RS1	10	9.3	6.8	8.4	10.3	5.3	19.5	15.4	6.1
Subject 3 RS2	4.4	5.8	7.6	9.6	10.5	5.9	16.7	13	6.7
Subject 4 RS1	127.5	27	13.3	8.5	9.5	5.6	228.9	40.72	18.9
Subject 4 RS2	36.5	16.9	4	12.9	9.8	4.3	159.3	45.6	6.3
Subject 4 RS3	21.6	17.2	6.5	5.3	8.7	5.4	79.9	38	10.7
Subject 5 RS1	24.9	20.4	9	48.2	18.5	9	48.8	19	9.7
Subject 6 RS1	25.5	13.7	6.8	25.8	13.4	5.2	61.2	29.6	5.9
Subject 6 RS2	26.2	21.6	7.2	9.2	11.7	4.9	59.2	36.4	7.4
Subject 7 RS1	9.8	11.7	7.1	22.7	17.9	6	30.2	22.4	6.4
Subject 7 RS2	18	14.2	6.2	30.8	16.3	16.6	45.7	24.4	16.8
Mean	29.9	16	7.8	24	14.4	7.3	75.2	28.2	9.6
Sd	32.1	5.8	2.3	19.4	5.3	3.5	61.4	10.2	4.3

Table 5.2: percentage errors with mean and standard deviation calculated across all subjects for all methods in the real SNR situation.

better, even without the use of any model. The non-parametric Saager's subtraction method, however, achieves worse performances than the nonlinear Kalman filter approaches. As far as the UKF and EKF-based approaches are concerned, we can see that they perform better than the other comparison methods; this is because we are using both a parametric approach and taking into account the information deriving from the reference channel data in order to reduce physiological noise. Therefore, these results confirm not only

the importance of the reference channel subtraction idea, but also quantify the actual improvements in the estimation of the HRF hidden in the fNIRS signal when subtracting physiological noise estimates from the corresponding standard channel signal.

For each error metric, a series of paired t-tests between techniques was also employed to check for statistical differences across the results. In particular, all methods were statistically different from CA when dealing with E (p<0.03), but no significant differences were detected among the other methods. It is to note that, according to Table 5.2, the nonlinear Kalman filter approaches seem to perform much better than the linear Kalman filter alone. Indeed, they give an error of $\approx 18\%$ which is lower than that of the linear Kalman filter, which is $\approx 30\%$. The same is true for the Saager's approach. It is likely that the lack of statistically significant differences between the non linear Kalman filter approaches and the other techniques is due to the low number of subjects available and considered in this study.

As far as the peak error E_{peak} is concerned, no statistical significant differences were noted among the Kalman methods, but all methods were statistically different from CA (p<0.04).

Finally, no statistically significant differences were detected in the latency error $E_{latency}$, except for the EKF approach with 2 sinusoids, which was significantly different from the Saager's method ($p < 0.001$).

The results achieved so far have highlighted that the performances of the UKF and EKF-based approaches are very similar ($\approx 19\%$ for the total estimation error). Even when the physiological noise model ϕ_i ef eqs. (4.3.1), (4.3.1) and (4.3.1) should be more accurate by taking into account more sinusoids, improvements in terms of error indexes are not visible. For instance, using a physiological noise model composed of two sinusoids (EKF2sin), which should better describe the complex noise present in fNIRS signals, does not improve the results in the HRF estimation compared to when using the single-sinusoid model (EKF1sin), and this can be seen in Fig. 5.3 and Fig. 5.4.

To quantitatively evaluate the performances of the UKF- and EKF-based approaches using a varying number of sinusoids (from 1 to 3), these non linear kalman filtering methods were run across all subjects and all reference channels located on the parietal cortex in order to estimate the noise model. The Akaike Information Criterion (AIC) was computed for each of the method between the original reference channel data and the estimated noise model in order to check whether adding more sinusoids in the physiological noise model ϕ_i actually improves the estimation of the physiological noise model and thus, consequently, the final HRF estimate. It is to note that in this case we are not trying to fit a model on the data that the model should describe as in the classic way, since the UKF and EKF try to estimate only low fre-

quency oscillations that overlap with the HRF band, and not other higher frequency components that are always present in the fNIRS signal. However, the computation of these indexes could be useful to evaluate which model is more likely to be the best.

In more details, both the UKF and EKF were implemented using the physiological noise model composed of 1, 2 and 3 sinusoids, respectively. Then, physiological noise estimation was run on all reference channel signals and the AIC was computed as:

$$AIC = ln(rss) + \frac{2(p-1)}{n}$$

where rss is the residual sum of squares given by the difference between the reference channel data and the physiological noise estimate obtained from the UKF and EKF with the three physiological noise models ϕ_i $i = 1, 2, 3$, p is the number of parameters of ϕ_i and n is the number of samples. Results of the AIC computation are shown in Table 5.3.

Mean AIC results						
Physiological noise model	UKF with ϕ_1	UKF with ϕ_2	UKF with ϕ_3	EKF with ϕ_1	EKF with ϕ_2	EKF with ϕ_3
Mean	22.92	23.49	23	22.79	21.17	22.43
Sd	0.44	0.79	0.79	0.46	0.41	0.57

Table 5.3: mean AIC values and their standard deviations computed by averaging across all reference channels and all subjects.

Looking at Table 5.3, it turns out that the mean AIC values are very similar to each other and with a very low standard deviation. From these results, we can suppose that enriching the physiological model ϕ_i with more sinusoids does not significantly improve the estimation of the real physiological noise. However, as we have stated before, the AIC is probably not the best index to use for this purpose. The similarity of the AIC results can also be explained by a predominance in the residual sum of squares of the high frequency non-modeled noise, which can overlook the improvements achieved by the use of more sinusoids in the estimation of the actual low frequency noise. This is the reason why in this thesis we tested the UKF with 2 sinusoids and EKF with both 1 and 2 sinusoids: we trusted the results achieved with the AIC analysis, using the single sinusoid model in the EKF algorithm, but at the same time we were aware of its limitations. Hence, using the 2 sinusoids model we had the chance to see whether in the final HRF estimate,

where a quantitative true index can be computed, the 2 sinusoids model was actually helping in improving the HRF estimate or not. From the results of Fig. 5.8 and table 5.2, where no differences between the HRFs estimated with the EKF with 2 and 1 sinusoids are appreciable, we can suppose that the results of the AIC analysis were quite correct.
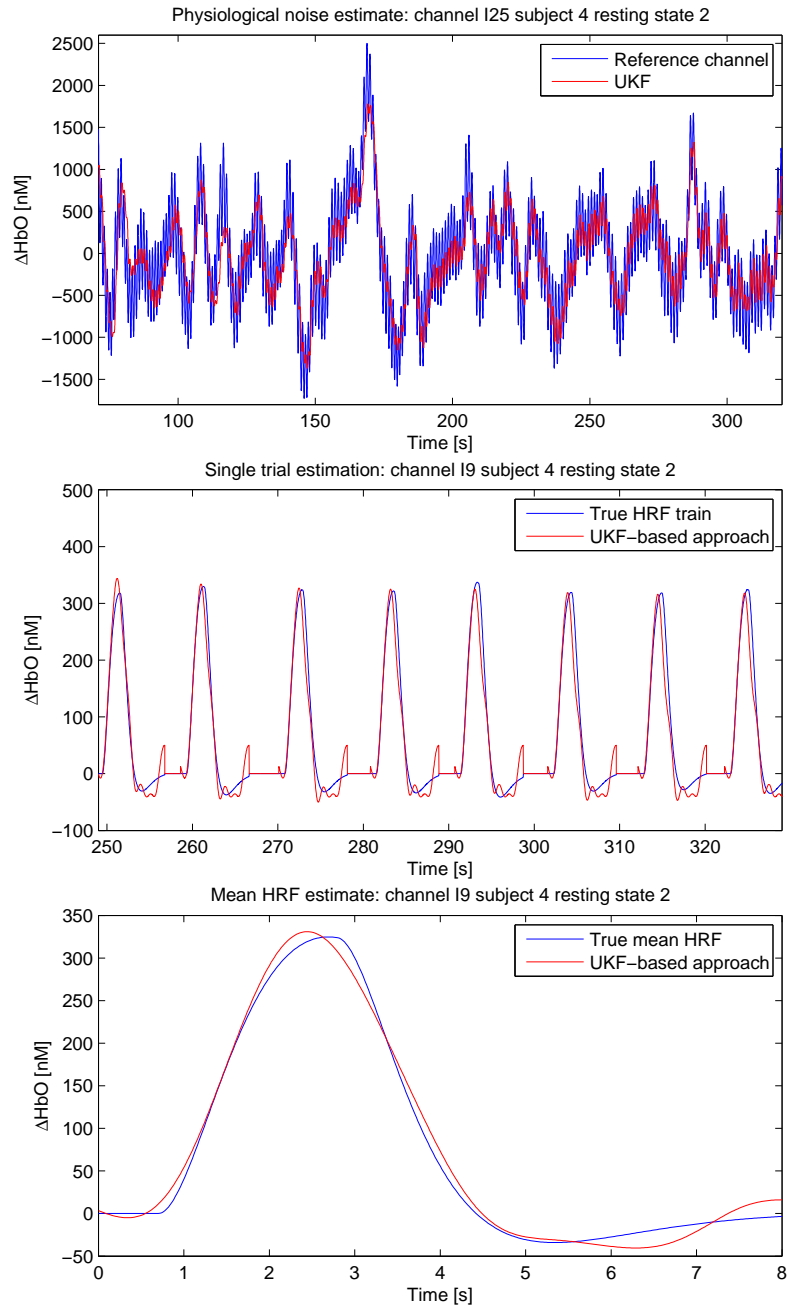
Figure 5.5: top: Unscented Kalman filtering results (red line) for the estimation of physiological noise from reference channel data (blue line) for a particular subject (zoom in the [80-320] s time window, reference channel source 9 - detector 25). Middle: single trial estimates obtained with the UKF-based proposed algorithm (red line) with the HRF train (blue line) added to the resting state data (zoom in the [249-328] s time window, standard channel source 9 - detector 9, which is correlated with the standard channel signal shown in the top figure). Bottom: mean HRF estimate (red line) obtained by averaging all single trial estimates obtained in the middle figure, superposed to the true mean HRF (blue line).
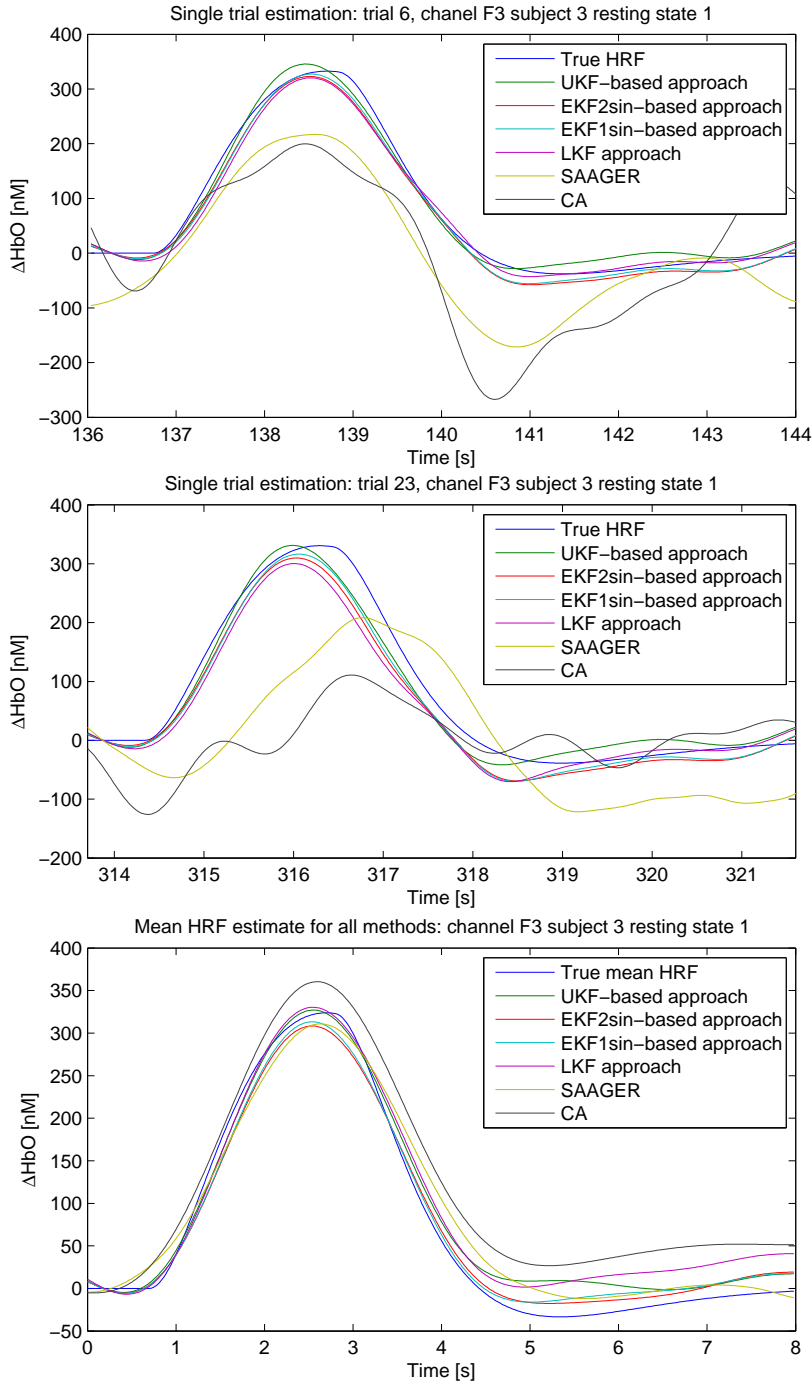
Figure 5.6: top and middle: true single trial HRFs (blue line) along with single trial HRFs estimated with all the methods in a particular subject (zoom in the [136-144] and [314.9-321.6] s time windows, standard channel source 6 - detector 3, SS channel used in the UKF-based physiological noise removal algorithm: source 4 - detector20). Bottom: true mean HRF (blue line) and mean HRF estimates computed by averaging all single trial estimates obtained with all methods.
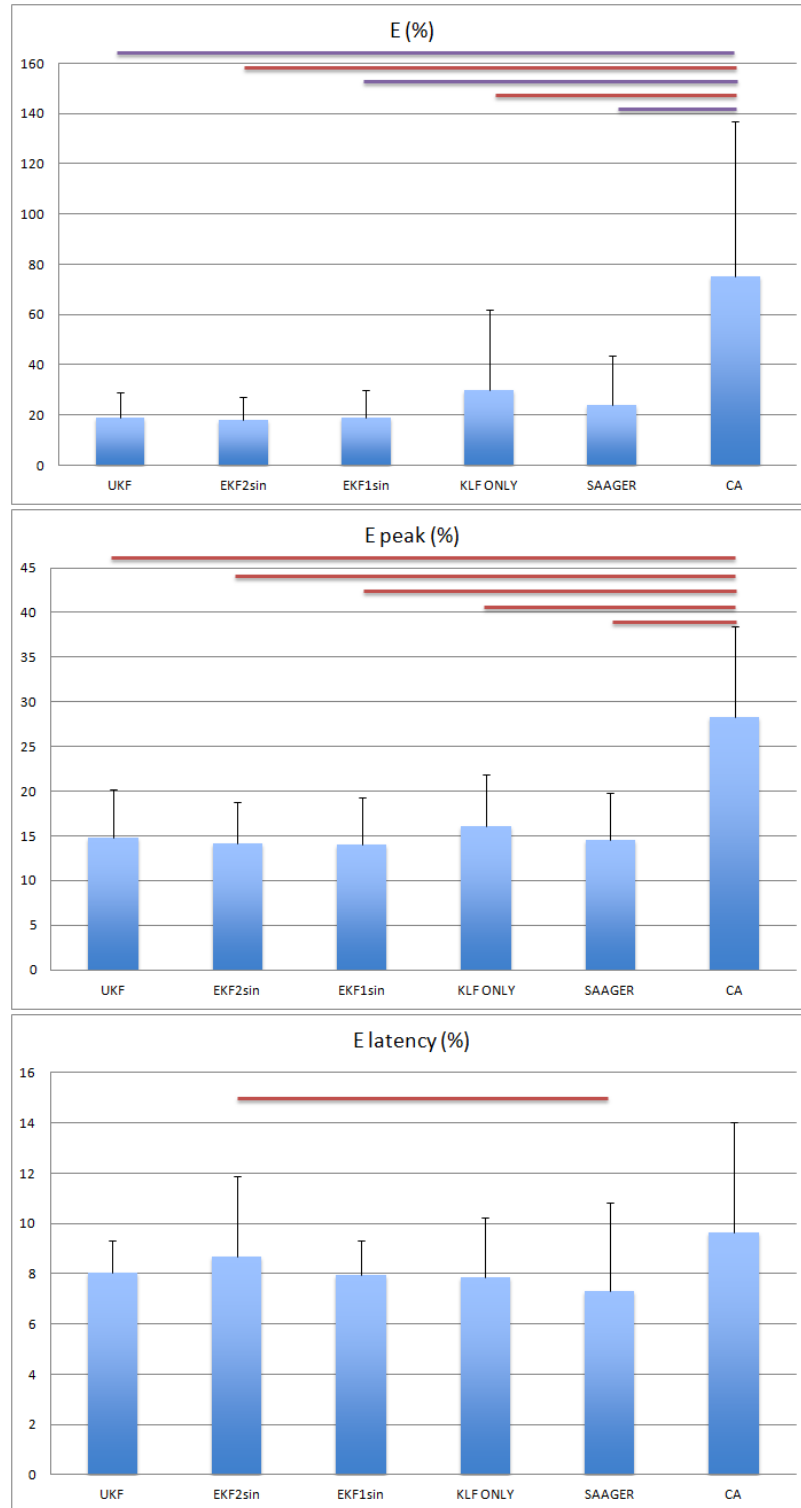
Figure 5.7: top: bar graph of the mean values obtained across all subjects for the index of error E in the real SNR situation. Middle: bar graph of the mean values obtained across all subjects for the index of error E_{peak} in the real SNR situation. Bottom: bar graph of the mean values obtained across all subjects for the index of error E_{lat} in the real SNR situation. Statistical significance at the $p < 0.05$ and $p < 0.01$ levels (two-tailed paired t-test) is illustrated by purple and red lines over the bars, respectively.

Chapter 6

Implementation on real data

The novel algorithm, along with the other methods used for the comparison, was subsequently tested on real cognitive data to assess whether its performance achieved the same good results of the semi-simulation scenario and therefore putting the ground for its application in real research and clinical settings.

6.1   Results

The dataset used in the real scenario was presented in section 2.1, where participants underwent a right-handed finger-tapping experiment. It is worth remarking that these results are only preliminary and future studies and insights need to be pursued with more participants. In order to apply the novel UKF-based algorithm and all other Kalman filter based techniques on this real data, the FIR time window and the number of temporal basis functions used in the model of the linear Kalman filter were modified according to the duration of the task involved. This is required to correctly detect the entire duration of the HRF, which is highly dependent on the task duration. In particular, for the 2 s tapping task the FIR time window was set to 12 s with 22 Gaussian functions, for the 6 s tapping task it was set to 16 s with 30 Gaussian functions, while for the 18 s tapping task it was set to 25 s with 46 Gaussian functions.

In Fig. 6.1, two examples of mean HRF estimated with all the techniques for the 18 s finger-tapping condition are displayed for a particular subject for a couple of symmetric channels, i.e. channels placed on the same position but in opposite hemispheres (left hemisphere channel: source 4 - detector 1, right hemisphere channel: source 8 - detector 10).

Referring to Fig. 6.1, we can note that there is great brain activation dur-
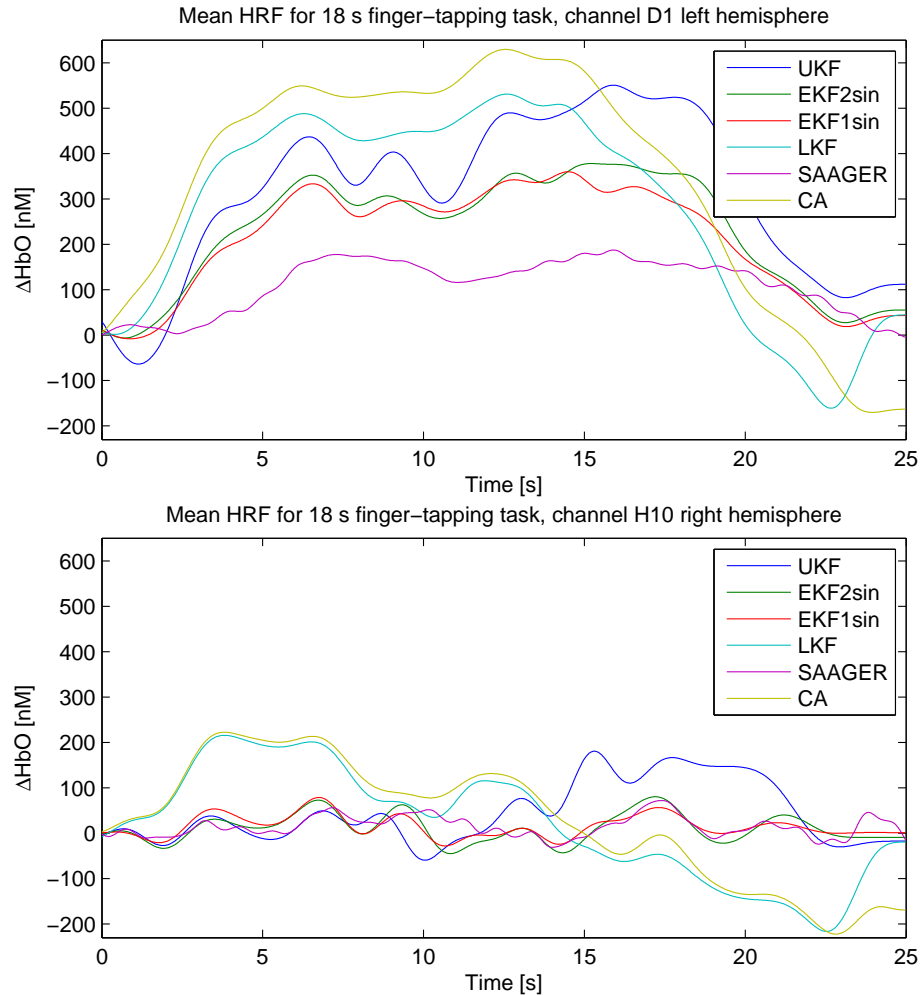
Figure 6.1: top: examples of mean HRF estimates obtained by the novel UKF-based algorithm and the other methods used in the comparison for the 18 s finger-tapping condition in a particular subject in a channel located in the left hemisphere (source 4 - detector 1). Bottom: examples of mean HRF estimates computed by all methods in the same subject but for a symmetric channel located on the right motor cortex (source 8 - detector 10).

ing the 18 s finger-tapping task in the channel located on the left hemisphere, but almost no activation is visible in the right one, where a baseline situation can be appreciated. These results are consistent with the underlying neurophysiological hypothesis, i.e. the brain activation is greater contralaterally than ipsilaterally. In addition, it is likely that the nonlinear Kalman approaches are able to better detect brain activation than the Saager's sub-
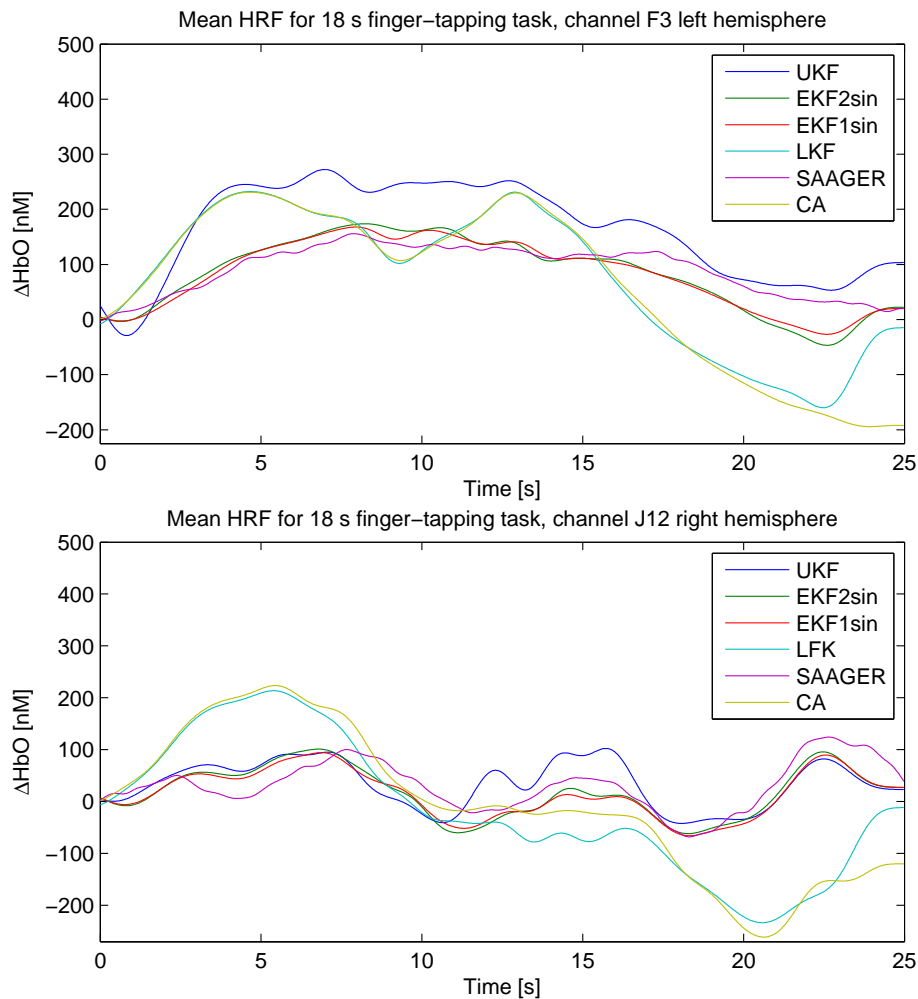
Figure 6.2: top: examples of mean HRF estimates obtained by the novel UKF-based algorithm and the other methods used for comparison for the 18 s finger-tapping condition in a particular subject in a channel located in the left hemisphere (source 6 - detector 3). Bottom: examples of mean HRF estimates computed by all methods for the same condition in the same subject but for a symmetric channel located on the right motor cortex (source 10 - detector 12).

traction method, which estimates a mean HRF with lower peak amplitude (≈ 150 nM) compared to the ones estimated by the non-linear Kalman filter approaches (≈ 500 nM). We can suppose that this likely underestimation of the HRF by Saager's method is due to the regression performed by this technique between the whole standard channel and reference channel signal,

which risks to remove part of the useful signal. Moreover, the non-linear Kalman filter parametric approaches rely on a model both for physiological noise and the HRF, which can presumably lead to less biased estimates. Conversely, CA and LKF are likely to overestimate the HRF, because of their inability to remove physiological noise oscillations, which still contaminate the mean HRF estimate. In the right hemisphere channel, the UKF and EKF approaches, as well as Saager's method, (i.e. all approaches that perform physiological noise correction) correctly estimate a baseline situation, whereas both CA and the linear Kalman filter provide a non-physiologically shaped activation, which resembles more a physiological noise oscillation.

These results are confirmed in Fig. 6.2, where all techniques performing a physiological noise reduction step estimate a physiologically shaped HRF in the left hemisphere and a baseline activation in the right one. Both CA and the linear Kalman filter, instead, detect brain activation in both hemispheres with approximately the same amplitude and a final undershoot with amplitude almost equal to the peak of the HRF itself and hence non physiological. Furthermore, the shape of the recovered HRFs in the right hemisphere channel by CA and LKF is far from being physiological, and more closely resemble a physiological noise oscillation.

Example results for the 6 s finger-tapping task are shown in Fig. 6.3 and 6.4 for a particular subject. In this case, the stimulus has a shorter duration: the expected brain activation will have lower amplitude compared to the 18 s task, while preserving the same noise level. This should produce a lower SNR condition compared to the 18 s task.

Note how CA and LKF estimate some physiological noise leading to non-physiological undershoots. All methods performing a physiological noise reduction step, instead, are able to reduce the oscillations and undershoot and tend to estimate a baseline condition, even if with more difficulty compared to the 18 s task.

Also in this lower SNR case, as can be appreciated in Fig. 6.3, CA and the linear Kalman filter show non-physiological undershoots and oscillations, which make the HRF estimation biased and non-physiological. The amplitude of this oscillation, likely due to physiological noise, can be mistaken by real activation during a peak amplitude analysis, leading to incorrect interpretation of the results. All methods performing a physiological noise reduction step, instead, are able to reduce oscillations and undershoots and perform better compared to the other methods, detecting the HRF in the left hemisphere and a baseline condition in the right one, even if with more difficulty compared to the 18 s task.

Results for the 2 s task are not reported here, because all methods performed poorly. This is likely due to the very small HRF elicited by such a
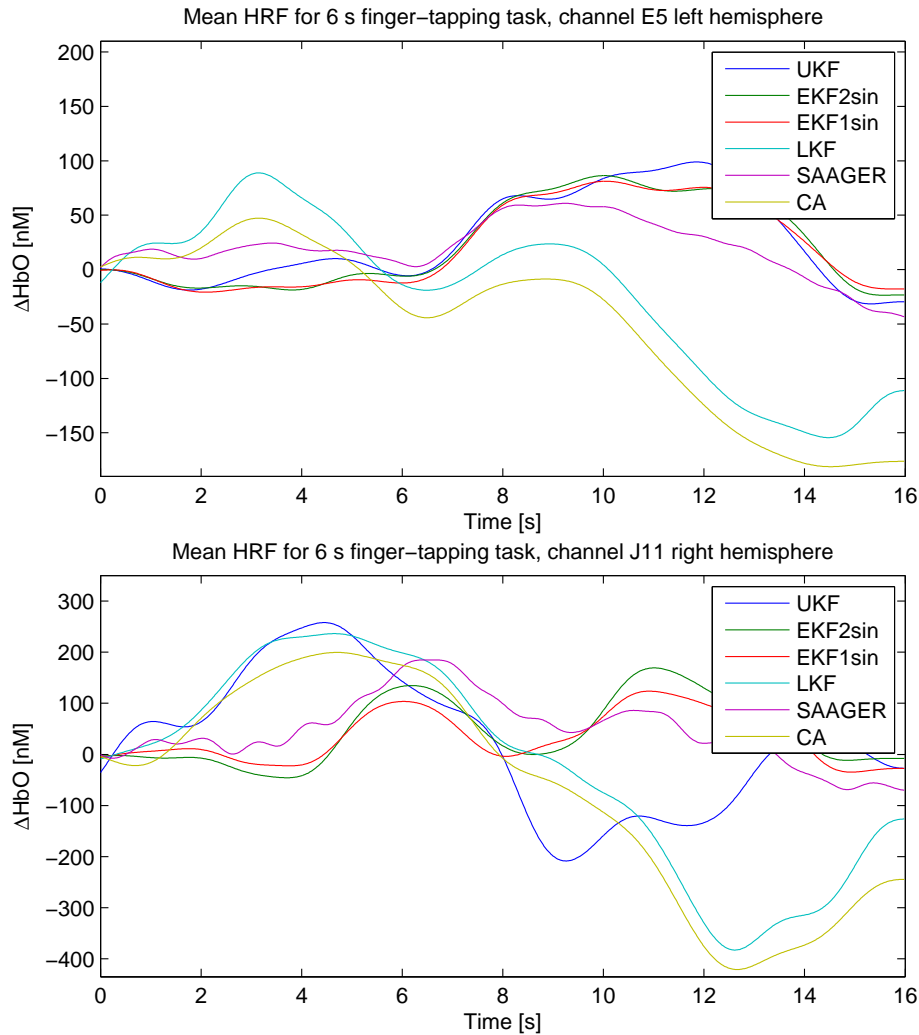
Figure 6.3: top: examples of mean HRF estimates obtained by the novel UKF-based algorithm and the other methods used for comparison for the 6 s finger-tapping condition in a channel located in the left hemisphere (source 5 - detector 5). Bottom: examples of mean HRF estimates computed by all methods for the same condition, but for a symmetric channel located on the right motor cortex (source 10 - detector 11).

short finger-tapping, coupled with the very low number of trials available for each participant. Further studies, with a higher number of trials for this task and of participants are required to test the methodologies also in this very low SNR condition.

On the whole, the proposed UKF-based algorithm seems to have a good

performance also with real data, giving the expected activation results, in accordance with literature.

6.2 Preliminary conclusions on real data analysis

In this chapter, we have demonstrated the ability of the proposed algorithm to detect brain activation on real data obtained during finger-tapping tasks. Results were consistent with neurophysiological hypothesis of contralateral activation, and estimated HRFs obtained were less noisy and more physiological compared to the ones estimated with the methods for comparison.

Chapter 7

Conclusions

7.1 Discussion

Functional near-infrared spectroscopy (fNIRS) is a novel neuroimaging technique which relies on near-infrared light, whose wavelengths lie between the 650 and 950 nm spectrum, to measure hemodynamic changes in the superficial layers of the brain by exploiting the different absorption behavior of oxy-hemoglobin (HbO) and deoxy-hemoglobin (HbR). Nowadays, this technique is being more and more used in research settings to determine brain activations associated with specific tasks and for further insights on brain activity. The reasons why fNIRS is now becoming an established neuroimaging technique can be found in its ease to use, cost effectiveness and completely non-invasiveness.

However, some issues still need to be faced regarding the estimation of the hemodynamic response function associated with brain activation. Indeed, the raw fNIRS signal does not only contain the HRF, but it is also contaminated by systemic interference and noise occurring in the superficial layers of the head. This interference typically derives from cardiac and respiratory activity and other physiological homeostatic processes such as the vasomotor activity. In addition, motion artifacts and instrumentation noise make the HRF estimation more difficult. As such, many studies are currently being conducted in this field to reduce physiology-based systemic interference and enhance HRF estimation from fNIRS signals, with the aim of making fNIRS technique more accurate and reliable for research and clinical use.

In this thesis, a novel algorithm was presented based on the estimation of the physiological interference using the so-called Unscented Kalman Filter. This method allows the reduction of physiological noise affecting standard channel signals, improving the estimation of the HRF, which is performed

87

using a linear Kalman filter as a second step in the procedure. In particular, the UKF, compared to the EKF, does not require the computation of the partial derivatives of the model during the linearization procedure, since its use is based on the computation of a fixed number of sample points, named sigma points, which capture the true mean and covariance of the states involved. In literature, it has been demonstrated that the UKF leads to better estimates and it is more robust, since it is not subjected to divergence phenomena associated to linearization errors, as in the EKF.

In particular, the novel method was tested in a semi-simulated scenario, where synthetic HRF trains were added to real resting state data and the algorithm was run to test its performance in the estimation of the known HRF. Known literature techniques (Saager's method, LKF, EKF1sin) and a newly proposed variant of the EKF1sin method, which uses a 2 sinusoidal model to estimate the noise model (EKF2sin) were implemented and used for comparison.

Two simulations were run. The first one was conducted in a situation of high SNR to determine the effectiveness of the methods implemented. Results showed that all methods achieve a high performance in this situation, leading correctly to very low indexes of error in the estimation of the HRF and its features compared to the true HRF. Once the effectiveness of the algorithms was confirmed, a second simulation was conducted to assess the performances of the methods in a more real context by lowering the peak of the synthetic HRF added and thus reducing the SNR. Results showed differences in terms of performance among the methods implemented. In particular, the UKF and the EKF-based approaches showed similar performances in terms of estimation error, and better performances compared to the linear Kalman filter, Saager's subtraction method and the CA. As such, these results confirm the effectiveness of the UKF and EKF-based approaches developed in this thesis for an improved HRF estimation. Furthermore, Saager's method performed better than CA and LKF. Therefore, the positive results of UKF- and EKF-based approaches and Saager's method highlight the importance of the use of the reference channel subtraction concept in order to improve HRF estimation. LKF performed better than CA: this result, together with the better performance of the parametric non linear Kalman filter approaches strengthen the hypothesis that using a model based approach gives improved results compared to non parametric approaches (CA and Saager's).

During the simulation phases, it was also noted that enriching the physiological noise model used in the UKF and EKF formulation with more sinusoids did not determine improvements in terms of HRF estimation (i.e., EKF1sin and EKF2sin has similar performances). To evaluate and confirm this observation, the Akaike Information Criterion was applied by running

the UKF- and EKF-based algorithms with physiological noise models with varying number of sinusoids (from 1 to 3), and results demonstrated that adding more sinusoids to the model did not significantly improve the final HRF estimate.

The choice of the UKF approach in this thesis was justified by the hypothesis that the fNIRS signal should be highly non linear. In this scenario, UKF should perform better than EKF, being a higher order filter. If the signal is not highly non linear, instead, it has been shown that the performances of EKF and UKF are highly similar [45]. The results achieved in this thesis are contradicting our initial hypothesis: the similar performance of UKF- and EKF-based approaches seems to point out that the fNIRS signal is not highly non linear. Nevertheless, results show that both methods can be applied successfully and the linearization performed in the UKF algorithm should produce more robust results. Further studies are required to understand whether there are situations in which the UKF approach can give much better results than the EKF-based approach (e.g. fNIRS signal acquired in difficult experiments, where more motion artifacts and signal non linearity are present).

Eventually, the algorithm was also tested on real cognitive data, where right-handed participants underwent a series of right-handed finger-tapping tasks with different durations. Results proved that both the UKF and EKF-based approaches are able to detect the HRFs in channels located on the contralateral motor cortex in the condition of 18 s finger-tapping tasks (high SNR) and in the condition of 6 s finger-tapping tasks (lower SNR). Activation in the ipsilateral hemisphere was detected as well, but with lower amplitude or as a baseline condition, according to well known neurophysiological hypothesis. The reference channel based Saager's method achieved similar performances, highlighting also in the real scenario case the importance of the reduction of physiological noise oscillations exploiting the reference channel signals. Instead, CA and LKF performances were the worst in this real scenario, recovering in many channels non-physiologically shaped HRFs, which closely resembled physiological noise oscillations.

The overall results, despite being obtained from a limited number of participants, are very promising and further studies and improvements are required to completely assess and validate the performance of the UKF-based algorithm proposed in this thesis.

7.2   Future studies

Results achieved so far are very promising, but future developments and insights are needed to evaluate the reasons why both UKF- and EKF-based approaches yielded similar performances.

First of all, testing the proposed UKF-based algorithm and the other comparison methods on an increased greater number of real subjects on a greater number of real subjects will be useful to test statistical significant differences between the results obtained by the different methods. Furthermore, a sensitivity analysis, aiming at computing the optimal set of initialization parameters for the UKF-based approach, will help in optimizing the filter, yielding improved final HRF estimates.

Moreover, future work will be necessary to understand why increasing the number of sinusoids in the physiological noise model ϕ_i did not improve HRF estimation. It might be due to the increased number of parameters to be estimated. Therefore, it might be possible to test the performance of the algorithm keeping a multi-sinusoidal model, but reducing the number of time-varying parameters. For example, improvements could be tested by fixing the phase θ_i of the sinusoids, lowering the complexity of the entire model.

Another interesting future development could be the application of the novel algorithm proposed on data acquired with DOT with high density arrays. This might be useful to test the algorithm on channels located on different areas of the cortex and hence with different expected activation. In this scenario, it could be interesting to evaluate whether the fNIRS signal non-linearity is constant over the whole brain surface or there are actually brain regions in which physiological noise is more present than in others, making the fNIRS signal more non-linear. If so, we expect the UKF-based algorithm to be more efficient than the EFK approach in these areas, while giving similar performances in regions of the cortex with a more linear signal. The novel proposed algorithm should also be tested on real cognitive data involving other tasks than finger-tapping, for example tasks involving the assessment of language, memory and attention. The activation recovered with the novel UKF-based algorithm should be compared with known literature activations, to further validate the proposed algorithm.

Finally, the UKF-based algorithm involves different steps during the signal processing. This might be sub-optimal, since it could lead to an underestimation of the true HRF, as noted in [32]. Hence, it could be useful to combine the physiological noise estimation step with the HRF estimation step into a single step to increase the overall performance of the algorithm.

Bibliography

[1] Gratton G., Fabiani M., Friedman D., Franceschini M.A., Fantini S., Corballis P., Gratton E., *Rapid Changes of Optical Parameters in the Human Brain during a Tapping Task*, Journal of Cognitive Neuroscience, 7, 446-456, 1995.

[2] Hoshi Y., Tamura M.,*Near-Infrared Optical Detection of Sequential Brain Activation in the Prefrontal Cortex during Mental Tasks*, NeuroImage, 5, 292-297, 1997.

[3] Scarpa F., Brigadoi S., Cutini S., Scatturin P., Zorzi M., Dell'Acqua R., Sparacino G., *A reference-channel based methodology to improve estimation of event related hemodynamic response from fNIRS measurements*, NeuroImage, 72, 106-119, 2013.

[4] Jöbsis, F.F., *Noninvasive infrared monitoring of cerebral and myocardial sufficiency and circulatory parameters*, Science, 198, 1264-1267, 1977.

[5] Flock S.T., Patterson M.S., Wilson B.C., Douglas R.W.,*Monte Carlo Modeling of Light Propagation in Highly Scattering Tissues: Model Predictions and Comparison with Diffusion Theory*, IEEE Transactions On Biomedical Engineering, 36, 12, 1989.

[6] Flock S.T., Jacques S.L., Wilson B.C., Star W.M., van Gemert M.J.C., *Optical properties of intralipid: a phantom medium for light propagation studies*, Lasers in Surgery and Medicine, 12, 510-519, 1992.

[7] Graf B. W., Ralston T. S., Jo Ko H., Boppart S. A., *Detecting intrinsic scattering changes correlated to neuron action potentials using optical coherence imaging*, Optics Express, 17, 134-155, 2009.

[8] Hoge R. D., Franceschini M. A., Covolan R. J. M., Huppert T., Mandeville J. B., Boas D. A., *Simultaneous recording of task-induced changes in blood oxygenation, volume, and flow using diffuse optical imaging and arterial spin-labeling MRI*, NeuroImage, 25, 701-707, 2005.

[9] Gibson A. P., Austin T., Everdell N. L., Schweiger M., Arridge S. R., Meek J. H., Wyatt J. S., Delpy D. T., Hebden J. C., *Three-dimentional whole-head optical tomography of passive motor evoked responses in the neonate*, NeuroImage, 30, 521-528, 2006.

[10] Cooper C., Delpy D., Nemoto E., *The relationship of oxygen delivery to absolute hemoglobin oxygenation and mitochondrial cytochrome oxidase redox state in the adult brain: a near-infrared spectroscopy study*, Biochemistry Journal, 332, 627-632, 1998.

[11] Cooper C., Cope M., Springett R., Amess P. N., Penrice J., Tyszczuk L., Punwani S., Ordidge R., Wyatt J., Delpy D. T., *Use of Mitochondrial Inhibitors to Demonstrate That Cytochrome Oxidase Near-Infrared Spectroscopy Can Measure Mitochondrial Dysfunction Noninvasively in the Brain*, Journal of Cerebral Blood Flow and Metabolism, 19, 27-38, 1999.

[12] Boas D., Franceschini M., Dunn A., Strangman G., *Nonivasive Imaging of Cerebral Activation with Diffuse Optical Tomography*, In Vivo Optical Imaging of Brain Function, CRC Press, 8, 196-216, 2002.

[13] Cope M., *The development of a Near-Infrared Spectroscopy System and Its Application for Noninvasive Monitoring of Cerebral Blood and Tissue Oxygenation in the Newborn Infant* , Ph.D. Thesis, University College London, 1991.

[14] Boas D., Gaudette T., Strangman G., Cheng X., Marota J., Mandeville J., *The accuracy of near-infrared spectroscopy and imaging during focal changes in cerebral hemodynamic*, NeuroImage, 13, 76-90, 2001.

[15] Aslin R. N., Mehler J., *Near-infrared spectroscopy for functional studies of brain activity in human infants: promise, prospects and challenges*, Journal of Biomedical Optics, 10, 011009, 2005.

[16] Bluestone A.Y., Abdoulaev G., Schmitz C., Barbour R. L., Hielscher A. H., *Three-dimensional optical-tomography of hemodynamics in the human head*, Optics Express, 9, 272-286, 2001.

[17] Lloyd-Fox S., Blasi A., Elwell C. E., *Illuminating the developing brain: the past, present and future of functional near infrared spectroscopy*, Neuroscience and Biobehavioral Reviews, 34, 269-284, 2010.

[18] Joseph D.K., Huppert T.J., Franceschini M.A., Boas D., *Diffuse optical tomography system to image brain activation with improved spatial*

resolution and validation with functional magnetic resonance imaging, Applied Optics, 45, 8142-8151, 2006.

[19] Gagnon L., Yücel M. A., Dehaes M., Dehaes M., Cooper R. J., Perdue K. L., Selb J., Huppert T., Hoge R. D., Boas D. A., *Quantification of the cortical contribuition to the NIRS signal over the motor cortex using concurrent NIRS-fMRI measurements*, NeuroImage, 59, 3933-3940, 2012.

[20] Zhang X., Toronov V., Fabiani M., Gratton G., Webb A., *The study of cerebral hemodynamic and neuronal response to visual stimulation using simultaneous NIR optical tomography and BOLD fMRI in humans*, Photonic Therapeutics and Diagnostic, 566, 2005.

[21] Cutini S., Scarpa F., Scatturin P., Jolicoeur P., Pluchino P., Zorzi M., Dell'Acqua R., *A hemodynamic correlate of lateralized visual short term memories*, Neuropsychologia, 49, 1611-1621, 2011.

[22] Ehlis A. C., Bähne C. G., Jacob C. P., Herrmann M. J., Fallgatter A. J., *Reduced lateral prefrontal activation in adult patients with attention-deficit/hyperactivity disorder during a working memory task: A funtional near-infrared spectroscopy (fNIRS) study*, Journal of Psychiatric Research, 42, 1060-1067, 2008.

[23] Brigadoi S., Cutini S., Scarpa F., Scatturin P., Dell'Acqua R., *Exploring the role of primary and supplementary motor areas in simple motor tasks with fNIRS*, Cognitive Processing, 13, 97-101, 2012.

[24] Wager T. D., Vazquez A., Hernandez L., Noll D. C., *Accounting for non linear BOLD effects in fMRI: parameter estimates and a model for prediction in rapid event-related studies*, NeuroImage, 25, 206-218, 2005.

[25] Tang L., Avison M. J., Gore J. C., *Nonlinear blood oxygen level dependent responses for transient activations and deactivations in V1, insights into the hemodynamic response function with the baloon model*, Magnetic Resonance Imaging, 27, 449-459, 2009.

[26] Scholkmann F., Spichtig S., Muehlemann T., Wolf M., *How to detect and reduce movement artifacts in near-infrared imaging using moving standard deviation and spline interpolation*, Physiological Measurement, 31, 649-662, 2010.

[27] Molavi B., Dumont A. G., *Wavelet-based motion artifact removal for functional near-infrared spectroscopy*, Physiological Measurements, 33, 259, 2012.

[28] Brigadoi S., Ceccherini L., Cutini S., Scarpa F., Scatturin P., Selb J., Gagnon L., Boas D. A., Cooper R. J., , *Motion artifacts in near-infrared spectroscopy: A comparison of motion correction techniques applied to real cognitive data*, NeuroImage, 85, 181-191, 2014.

[29] Jasdzewski G., Strangman G., Wagner J., Kwong K. K., Poldrack R. A., Boas D. A., *Differences in the hemodynamic response to the event-related motor and visual paradigms as measured by near-infrared spectroscopy*, NeuroImage, 20, 479-488, 2003.

[30] Gagnon L., Cooper R. J., Yücel M. A., Perdue K. L., Greve D. N., Boas D. A., *Short separation channel location impacts the performance of short channel regression in NIRS*, NeuroImage, 59, 2518-2528, 2012.

[31] Saager R., Berger A., *Measurement of layer-like hemodynamic trends in scalp and cortex: implications for physiological baseline suppression in functional near-infrared spectroscopy*, Journal of Biomedical Optics, 13, 1679-1685, 2008.

[32] Brigadoi S., *Shedding light into the brain: Methodological innovations in optical neuroimaging*, Ph.D. Thesis, 3, 59-88, Padova University, 2014.

[33] Gagnon L., Perdue K., Greve D. N., Goldenholds D., Kaskhedikar G., Boas D. A., *Improved recovery of the hemodynamic response in diffuse optical imaging using short optode separations and state space modeling*, NeuroImage, 56, 1362-1371, 2011.

[34] Zhang Q., Strangman G. E., Ganis G., *Adaptive filtering to reduce global interference in non-invasive NIRS measures of brain activation: How well and when does it work?*, NeuroImage, 45, 788-794, 2009.

[35] Ambrosin A., Master Thesis:*Kalman filter approach for the estimation of the hemodynamic response from near-infrared spectroscopy data (fNIRS)*, Padova University, 2013.

[36] Glover H. G., *Deconvolution of Impulse Response in Event-Related BOLD fMRI*, NeuroImage, 9, 416-429, 1999.

[37] Kalman R. E., *A New Approach to Linear Filtering and Prediction Problems*, Journal of Fluids Engineering, 81, 35-45, 1960.

[38] Julier S. J., Uhlmann J. K., Durrant-Whyte H., *A new approach for filtering nonlinear systems*, Proceedings of the American Control Conference, 1628-1632, 1995.

[39] Julier S. J., Uhlmann J. K., *A new extension of the Kalman filter to nonlinear systems*, Proceedings of AeroSense: The 11th International Symposium on Aerospace/Defense Sensing, Simulation and Controls, 1997.

[40] Wan E. A., van der Merwe R., Nelson A. T., *Dual estimation and the unscented transformation*, Advances in Neural Information Processing Systems, MIT Press, 666-672, 2000.

[41] Wan E. A., van der Merwe R., *The unscented Kalman filter for nonlinear estimation*, Proceedings of Symposium on Adaptive Systems for Signal Processing, Communication and Control (AS-SPCC), IEEE, Alberta, Canada, October 2000.

[42] Haykin S., *Kalman filtering and Neural networks*, John Wiley & sons Inc., Ch. 7, pp. 230-231, 2001.

[43] Huppert T. J., Diamond S. G., Franceschini M. A., Boas D. A., *HomER: a review of time-series analysis methods for near-infrared spectroscopy of the brain*, Applied Optics, 48, 280-298, 2009.

[44] Gagnon L., Yücel M. A., Boas D. A., Cooper R. J., *Further improvement in reducing superficial contamination in NIRS using double short separation measurements*, NeuroImage, 85, 127-135, 2014.

[45] Fiorenzani T., Manes C., Oriolo G., Peliti P., *Comparative study of Unscented Kalman filter and Extended Kalman filter for position/attitude estimation in unmanned aerial vehicles*, Inst. for Systems Analysis and Computer Science (IASI-CNR), Rome, Italy, Rept. 08-08, 2008.

Sitography

[46] http://pubs.acs.org/email/cen/html/120907204622.html

[47] http://www.crsltd.com/tools-for-functional-imaging/tomographic-fnirs-imaging

[48] http://www.iopscience.iop.org/0967-3334/33/6/925/article

Acknowledgments

I would like to thank Professor Giovanni Sparacino for being welcoming and available for important discussions throughout the developing of this thesis. I would also like to thank Sabrina Brigadoi for helping me in fruitful corrections and directions. Finally, last but not least, I am very thankful to Alessandra for her constant support during these years and to my parents, for their early emphasis on the importance of education.